Doctoral Thesis

Microscopic characterization of diatoms and their changes with heating by infrared (IR) micro-spectroscopy

July 2015

Department of Earth and Space Science,

Graduate School of Science, Osaka University

Leila Alipour

博士論文

顕微赤外分光による珪藻の特性とその加熱変化の評価

2015 年 7 月

大阪大学大学院理学研究科宇宙地球科学専攻

アリプル　レイラ

Look deep into nature, and then you will understand everything better.

Albert Einstein

Acknowledgments

It would not have been achievable to fulfill the requirements for this PhD thesis without support of many kind people over the course of this demanding work.

First and foremost, I owe a great deal of thanks to my PhD supervisor Professor Satoru Nakashima, at the Laboratory of Physical Geochemistry, for all his scientific, honorable friendship, and moral supports during the course.

I am grateful to Associate Professor Osamu Hisatomi and Assistant Professors Makoto Katsura and Tadashi Yokoyama for their valuable discussions and comments during my stay at Osaka University, Associate Professor Osamu Hisatomi also served as one of my committee members.

I would like to thank Professor Tadashi Kondo, Professor Sho Sasaki and Professor Kentaro Terada for serving on my committee.

My heartfelt thanks go to Professor emeritus Koichi Hatada and all other respected fellows of Toyonaka Rotary Club for their kindness, humble manner and financial supports.

My sincere thanks are for Mrs. Keiko Inoue-Uozumi for being beside me at the most difficult time of my stay in Japan. I also would like to thank Mrs. Fusa Kasai, and other members of Toyonaka International Friendship Association (Tifa) for their kindness and sense of humanity.

I would like to thank the friendship and cooperation of previous and current members of Nakashima group, especially Mai Hamamoto, Tomoka Nishimura, Ryota Tonoue, Chie Onga, Misa Okada, Ryota Tomizawa, Sagakuni Nagasaki and Yuki Nakaya.

I wish to acknowledge the academic, technical and financial support of Osaka University and its staff in particular Graduate School of Science that provided the necessary support for this research.

I owe more than mere words to my parents Olya and Azhdar as well as my sisters Nasim and Ayda for everything they have done to me throughout my life and being unconditionally just there when I need them.

Last but not least, I must thank my loving husband, Afshin, and beloved sweet daughter, Arshida, for standing beside me all the way with outmost patience and understandings, giving me the courage and motivation to continue and challenge all difficulties to move my career forward.

Abstract

In order to characterize a representative biomineral, washed present day centric diatom samples (Diameter: 100-350μm) have been analyzed and imaged by infrared (IR) micro-spectroscopy and Scanning Electron Microscopy (SEM).

Since diatom silica frustules have complex microscopic morphology including many void areas such as micro- or nano-pores, the effects of voids on the IR spectral band shapes were first evaluated. With increasing void area %, $1220cm^{-1}/1070cm^{-1}$ peak height ratio (Si-O polymerization index) increases and $950cm^{-1}/800cm^{-1}$ peak height ratio (Si-OH/Si-O-Si) decreases, both approaching 1. Based on the void area% of representative diatom samples determined by SEM image analyses (51.5% to 20.5%) and spectral simulation, the $1220cm^{-1}/1070cm^{-1}$ ratios of diatom samples are sometimes affected by the void effect, but the $950cm^{-1}/800cm^{-1}$ ratios can indicate real structural information of silica. This void effect should be carefully evaluated for IR micro-spectroscopy of micro/nano-porous materials. IR micro-spectroscopic mapping of 4 representative diatom silica frustules indicated some large $950cm^{-1}/800cm^{-1}$ ratio regions suggesting the presence of hydrated amorphous immature silica in the chemical structure.

Based on the IR and SEM results on 43 diatom samples, maturity of diatom silica frustules is considered to increase with $1220cm^{-1}/1070cm^{-1}$ peak height ratios (opposite trend to the void effect) by IR micro-spectroscopy, associated with the increase of average thicknesses by optical microscope and the decrease of void area percentages by SEM. These IR micro-spectroscopic data with careful void effect evaluation may be applied to physicochemical structures of many other bionanomaterials including biominerals.

In situ heating IR transflection micro-spectroscopy has been conducted on unwashed diatom frustules on Al plates to examine transformation processes upon heating of aliphatic CHs, proteins and silica for simulating their changes with burial-diagenesis.

Assuming the two first order reaction model (faster and slower rates), the kinetic parameters (reaction rate constants k_1 and k_2 and activation energies E_a) for aliphatic CHs

(CH_2 and CH_3), proteins (amide I and amide II bands) and silica (the 3650cm^{-1} band due to stretching of O-H bound to Si and the 805cm^{-1} band due to symmetric Si-O-Si stretching vibration) were evaluated. The obtained results suggest possible interactions of 1) decreases of aliphatic CH_2 and amide I and 2) silica transformation (SiOSi increase) and slower decrease rates k_2 of aliphatic CHs and amide I, during the heating of diatom frustules.

Comparison of obtained results with those for heating of cyanobacteria, coal and kerogen together with those for hydrothermal decomposition of amino acids, suggest that organic transformation reactions including protein degradation and generation of aliphatic hydrocarbons inside the diatom silica frustules might be different from those of proteins and/or kerogens separated from the biological structures. Although further studies are needed, importance of organic-inorganic interactions should be noted during the burial-diagenesis of diatom frustules.

Table of Contents

Chapter 1. General introduction

1.1. Diatoms as a representative biomineral with silica frustules

Inorganic materials (minerals) are often used as encasement/protection or support of biological bodies: silicates in diatoms and algae, carbonates in invertebrates, and calcium phosphates and carbonates in vertebrates (Mann, 2001; Boskey, 2003). They are called biominerals. Appearance of biominerals dates back to about 600 million years ago based on geological records, when small, unicellular and simple living organisms on the earth changed into complex and multicellular organisms with tough building materials (Mann, 2001; Knoll, 2003; Igisu et al 2014).

Despite extensive studies of bulk chemical compositions, structures and properties of these biominerals, their formation processes (called biomineralization) are still poorly understood (Mann, 2001; Sumper, 2002; Kröger & Sumper, 2004; Mount et al 2004, Hildebrand, 2008, Tesson & Hildebrand, 2013). One of the main reasons is the lack of microscopic characterization of biominerals.

Silica biomineralization on the earth is widespread, largely by simple aquatic living structures including unicellular organisms such as diatoms and radiolaria in addition to multicellular sponges (Lowenstam & Weiner, 1989; Sumper & Kröger, 2004). These organisms produce silica based skeletons forming the majority of their body mass and, in the case of diatoms; the silica skeletons exhibit intricate cell wall patterns in nano- to micro-meter ranges (Sumper & Kröger, 2004).

Diatoms are a large and ecologically important group of eukaryotic unicellular photosynthetic phytoplankton controlling the carbon cycle of the earth (Smetacek, 1985; Falkowski et al 1998; Wilkerson & Dugdale, 1998) and are an important origin of petroleum and natural gas together with other small aquatic organisms such as radiolaria and foraminifera (Aoyagi & Omokawa 1992; Aoyagi & Omokawa 1993, Theriot, 2012; Levitan et al 2014). Their cell wall is composed of mainly hydrous amorphous silica

($SiO_2.nH_2O$) with a small portion of organic macromolecules (proteins and polysaccharides) (Hecky et al, 1973; Kröger & Poulsen, 2008; Sumper & Brunner, 2008) (Fig.1.1a).

The biomineralization of diatom silica is considered to involve a variety of metabolic processes: the diatom takes up silicon from the environment in soluble form as silicic acid and then transports it into the cell. During the cell wall synthesis, silicic acid is polymerized into silica forming diatom frustule (Hildebrand, 2008; Hecky et al, 1973) (Fig.1.1a). However, formation processes of diatom silica frustules are not well known because of the lack of their microscopic chemical structures.

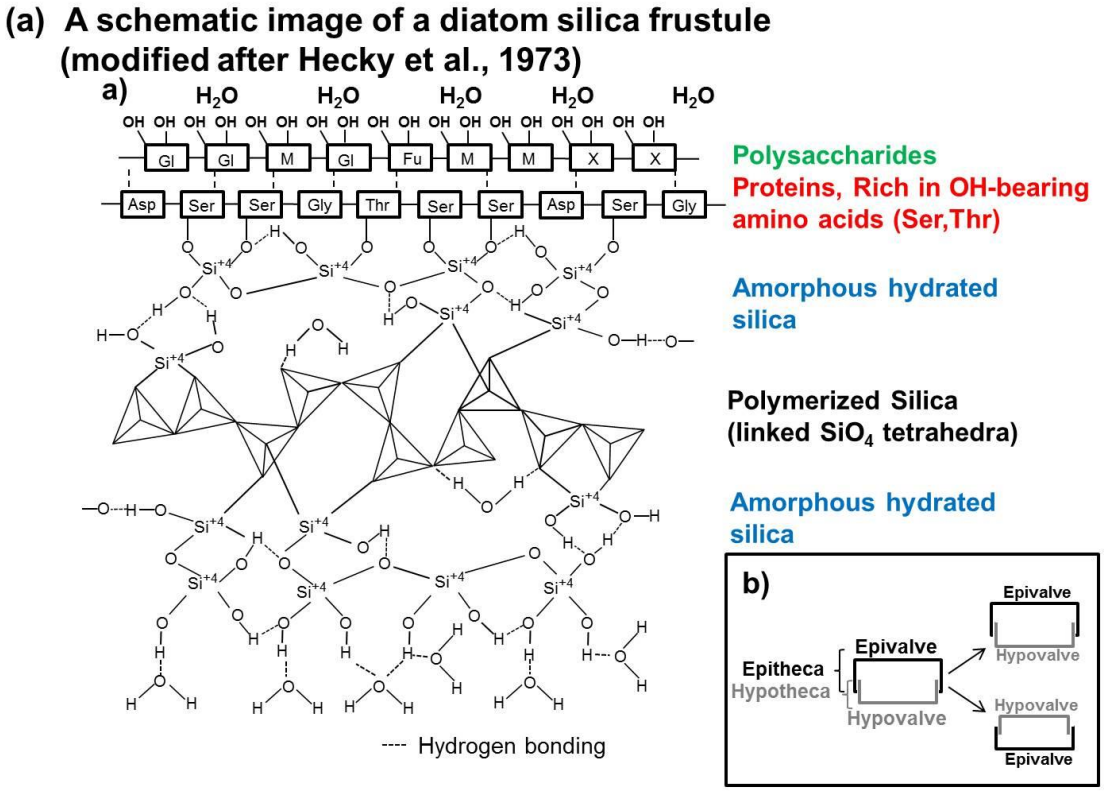

Fig.1.1. Schematic images of (a) chemical structure of diatom silica frustule and (b) cell division process.

In this research, Infrared (IR) micro-spectroscopy, Scanning Electron Microscopy (SEM) and Raman micro-spectroscopy has been applied to describe chemical and physical structures of present day centric diatoms (*Arachnoidiscus ornatus*) (Diameter: 100-350 µm) in micro-scales.

The structure of diatom silica is considered to be similar to amorphous hydrous silica gel (Asada et al., 2002). The structures of amorphous silicates are often described by "Q^n species" (Lin et al, 2011) while "n" in the term "Q^n species" indicates the number of the bridging oxygen linked to the Si atom, i.e., how many tetrahedra (possible values: 0–4) are bonded to the tetrahedron. Quartz mainly consists of Q^3 and Q^4 species, having a high degree of polymerization, whereas hydrated species often contain Q^1 and Q^2 species, corresponding to low degrees of polymerization.

Infrared Si-O bands around 1300-800cm^{-1} are considered to be composed of several components related to the above Q^n species (García-Lodeiro et al., 2009). A band at 815cm^{-1} is corresponding to Si–O symmetric stretching vibrations in Q^1 units and a band around 970cm^{-1} to Si–OH asymmetric stretching vibrations in Q^2 units. The 1070cm^{-1} band can be assigned to Q^3 species with three oxygen atoms bridged to Si, while the 1220cm^{-1} band can be assigned to Q^4 species with four oxygen atoms bridged to Si. Therefore, the 1220cm^{-1}/1070cm^{-1} peak height ratio would correspond to Q^4/Q^3 species ratio and can be expected to indicate degrees of Si-O-Si linkage with increasing polymerization.

In biogenic silica, 800cm^{-1}/950cm^{-1} peak height ratio has been proposed as an indicator of diagenetic transformation of biosilica (Schmidt et al 2001). However, since 950cm^{-1} peak due to Si-OH can disappear; an inverse ratio of 950cm^{-1}/800cm^{-1} has been used in order not to make the ratio infinite. This ratio has been already used as a measure of diagenetic transformation of diatom silica (Nakashima et al., 2002)(Fig.1.2).

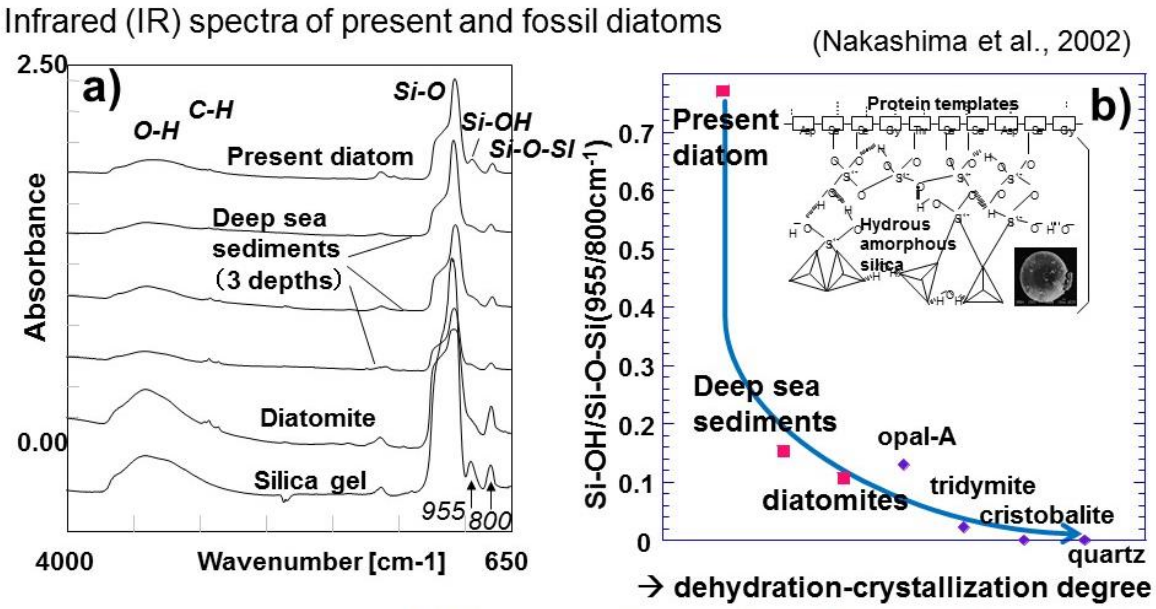

Fig.1.2. (a) Infrared spectra of present and fossil diatoms and (b) changes in Si-OH/Si-O-Si ratio ($955cm^{-1}/800cm^{-1}$ peak height ratio) of diatom silica frustules and some silica minerals (modified after Nakashima et al., 2002).

Since diatom silica frustules have abundant micro- and nano-pores, effects of voids on IR micro-spectroscopy have been evaluated (Chapter 2: 2.3.2). Also, the void area percentages of diatoms have been determined from SEM imaging (Chapter 2: 2.3.3). After careful evaluation of the void effects on diatoms, IR absorption peaks and their ratios have been determined for 43 diatom samples. IR microscopic imaging has been conducted by mapping the microscopic distribution of IR peak heights and ratios for 4 representative diatom samples (Chapter 2: 2.3.6).

1.2. Organic-inorganic interactions in diatom silica frustules during burial-diagenesis

Dead bodies of marine diatoms are sedimented on the ocean floor and buried in marine sediments with time. During their burial, temperature and pressure increase and organic components in diatom bodies are transformed. Silica is also transformed from amorphous

hydrous silica (Opal-A) via cristobalite (Opal-C) to quartz (Qz) (Pollastro, 1993)(Fig.1.3). These burial processes are subdivided into three phases: diagenesis, catagenesis and metagenesis (Berner, 1980; Tissot and Welt, 1984) which include complex processes such as compaction, heat-, fluid- and mass-flow, together with reaction kinetics (Hantschel and Kauerauf, 2009).

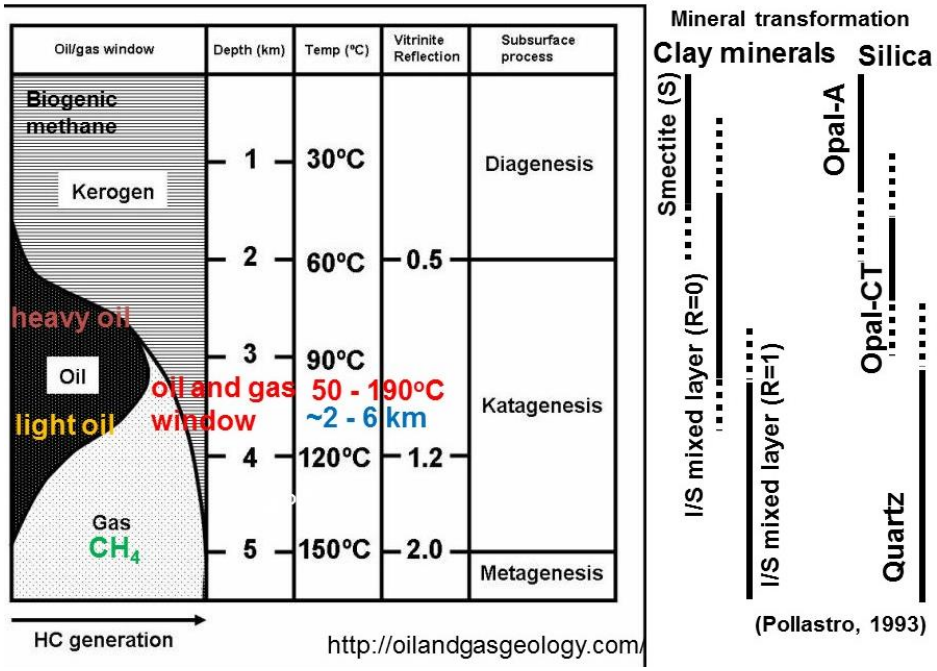

Fig.1.3. A schematic image of oil and gas generation during burial, diagenesis, catagenesis and metagenesis of sediments including biological debris such as diatoms. Transformations of clay minerals and silica are also indicated.

Generation of hydrocarbons is considered to be related to transformation of organic components in aquatic organisms such as diatoms during the burial-diagenesis (Tissot and Welt, 1984). Evaluation of hydrocarbon generation potentials has been conducted often by using reaction kinetics of kerogen to understand quality and quantity of petroleum and natural gas (Behar et al., 1997; Burnham et al., 1989; Dieckmann et al., 2000; Stainforth, 2009). Most of experimental simulations of hydrocarbon generation reactions have been conducted at high temperatures (450^{o}C -350^{o}C) resulting in wide ranges of rates and

activation energies (170 – 370 kJ/mol) (Behar et al., 1997; Burnham et al., 1989; Dieckmann et al., 2000; Stainforth, 2009; Tonoue, 2015: PhD thesis) with varying values giving a very large range of time scales for hydrocarbon generation by their extrapolation to lower temperatures of 80°C to 200°C (oil and gas window: natural hydrocarbon reservoir conditions)(Fig.1.4). Although some catalytic effects of minerals on rapid hydrocarbon generation have been suggested (Johns, 1979; Wei et al., 2006), few quantitative evaluations were reported. In particular, detailed kinetic studies of organic transformation processes during burial and diagenesis of diatomaceous sediments have not been simulated experimentally by using diatoms themselves as the source rock.

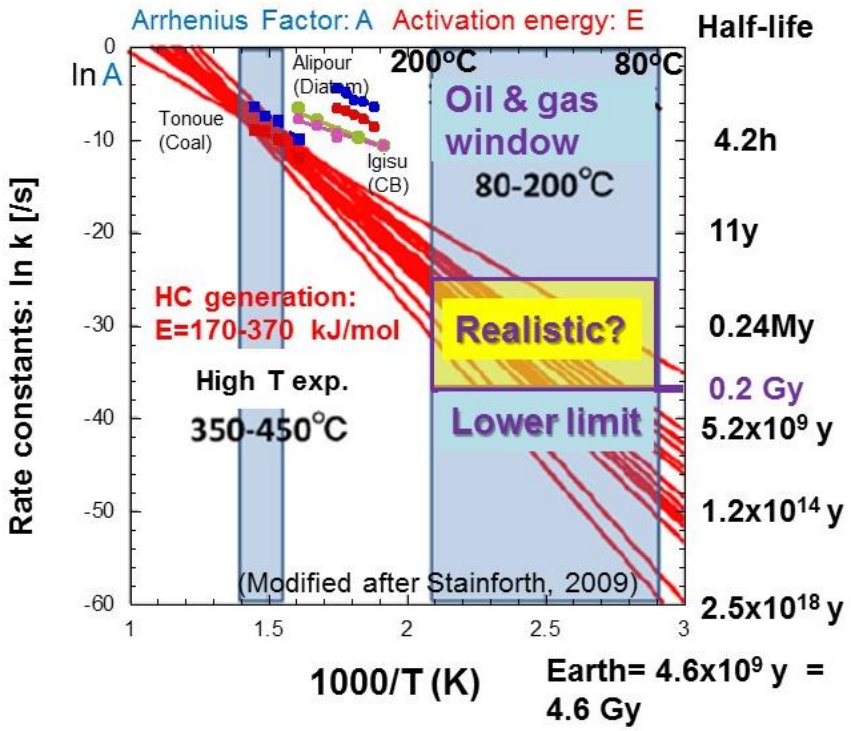

Fig.1.4. Arrhenius diagram for hydrocarbon generation reactions modified after Stainforth (2009) with some reported data on aliphatic CH decrease on coal (Tonoue, 2015) and on cyanobacteria (Igisu et al., 2015: submitted).

In this study, thermal transformations of diatoms are studied by in situ heating experiments under a Fourier transform infrared (FT-IR) spectrometer and kinetic parameters (reaction rate constants and activation energies) have been evaluated. A Transflection-mode FTIR spectroscopy was employed for measuring IR spectra of diatoms on Al plate in a heating stage. The transflection method of microscopic samples on metal plates is a useful method for studying in-situ heating behavior of geochemical samples (Okumura and Nakashima, 2004; 2005; 2006, Kebukawa et al., 2010, Tonoue et al., 2014).

Although generation of hydrocarbons from diatoms is considered to be related to transformation of organic components during the burial-diagenesis (Tissot and Welt, 1984), detailed relations of aliphatic hydrocarbon release and protein degradation are not known.

In this thesis, aliphatic hydrocarbon release, protein degradation and silica transformation processes were studied by the in situ heating IR transflection micro-spectroscopy of diatom frustules. The kinetic parameters (reaction rate constants and activation energies) for aliphatic CHs (CH_2 and CH_3), proteins (amide I and amide II bands) and silica (the 3650cm^{-1} band due to stretching of O-H bound to Si and the 805cm^{-1} band due to symmetric Si-O-Si stretching vibration) were also evaluated. The relationships among these components were clarified as well.

Chapter 2. Infrared (IR) Micro-Spectroscopy of Bionanomaterials (Diatoms) with Careful Evaluation of Void Effects

This chapter is modified from the paper "Infrared (IR) Micro-Spectroscopy of Bionanomaterials (Diatoms) with Careful Evaluation of Void Effects",
by Leila Alipour , Mai Hamamoto , Satoru Nakashima, Rika Harui, Masanari Furiki and Osamu Oku,
accepted on July 13, 2015 for publication in *Applied Spectroscopy*.

2.1. Introduction

In biological systems, certain elements are selectively extracted from the environment and incorporated into functional structures (Mann, 2001). As a result; inorganic solids are often deposited on biological tissues. Examples include silicates in diatoms and algae, carbonates in invertebrates, and calcium phosphates and carbonates in vertebrates (Boskey, 2003). These are called biominerals forming structural features such as sea shells, bones and teeth in mammals and birds (Mann, 2001). Appearance of biominerals dates back to about 600 million years ago based on geological records, when small, unicellular and simple living organisms on the earth changed into complex and multicellular organisms with tough building materials (Mann, 2001; Knoll, 2003; Igisu et al 2014).

Despite extensive studies of bulk chemical compositions, structures and properties of these biominerals, their formation processes (called biomineralization) are still poorly understood (Mann, 2001; Sumper, 2002; Kröger & Sumper, 2004; Mount et al 2004, Hildebrand, 2008, Tesson & Hildebrand, 2013). One of the main reasons is the lack of microscopic characterization of biominerals.

Silica biomineralization on the earth is widespread, largely by simple aquatic living structures including unicellular organisms such as diatoms and radiolaria in addition to multicellular sponges (Lowenstam & Weiner, 1989; Sumper & Kröger, 2004). These

organisms produce silica based skeletons forming the majority of their body mass and, in the case of diatoms, the silica skeletons exhibit intricate cell wall patterns in nano- to micro-meter ranges (Sumper & Kröger, 2004).

Diatoms are a large and ecologically important group of eukaryotic unicellular photosynthetic phytoplankton controlling the carbon cycle of the earth (Smetacek, 1985; Falkowski et al 1998; Wilkerson & Dugdale, 1998). They not only play a key role in the regulation of the biogeochemical cycle of silicon in the modern ocean (Tréguer et al., 1995; Yool & Tyrrell, 2003), but also are an important origin of petroleum and natural gas (Aoyagi & Omokawa 1992; Aoyagi & Omokawa 1993, Theriot, 2012; Levitan et al 2014). The diatom cell wall is composed of mainly hydrous amorphous silica ($SiO_2.nH_2O$) with a small portion of organic macromolecules (proteins and polysaccharides) (Hecky et al, 1973; Kröger & Poulsen, 2008; Sumper & Brunner, 2008) (Fig.2.1a). Because of beautiful nano and micro-scale structures of diatoms (Fig.2.2), they are often regarded as model materials for nano-patterning and nano-fabrication (Mann & Ozin, 1996; Schäffer et al, 1997; Parkinson & Gordon, 1999; Tang et al, 2003; Losic et al, 2005; Gilbert et al 2005; Losic et al, 2006; Losic et al, 2007).

The biomineralization of diatom silica is considered to involve a variety of metabolic processes: the diatom takes up silicon from the environment in soluble form as silicic acid and then transports it into the cell. During the cell wall synthesis, silicic acid is polymerized into a silica forming diatom frustule (Hildebrand, 2008; Hecky et al, 1973) (Fig.2.1a). However, formation processes of diatom silica frustules are not well known because of the lack of their microscopic chemical structures.

In this research, I applied Infrared (IR) micro-spectroscopy, Scanning Electron Microscopy (SEM) and Raman spectroscopy to describe chemical and physical structures of present day centric diatoms (*Arachnoidiscus ornatus*) (Diameter: 100-350 μm) in micro-scales.

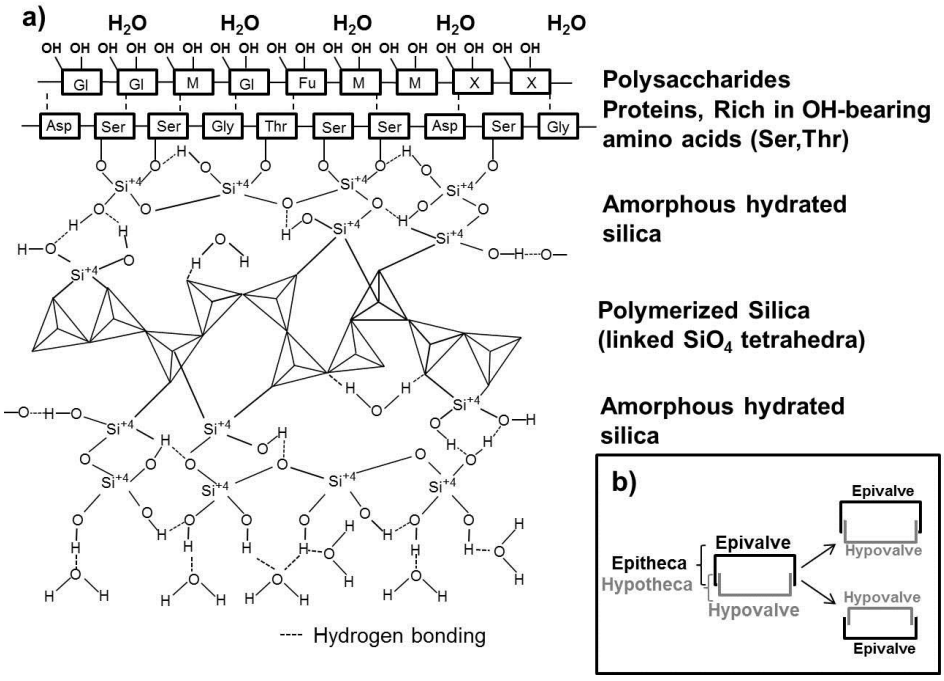

Fig.2.1. (a) A schematic image of a diatom silica frustule (modified after Hecky et al., 1973), (b) Schematic cross sections of diatom silica frustules during a cell division.

The structure of diatom silica is considered to be similar to amorphous hydrous silica gel (Asada et al., 2002). The structures of amorphous silicates are often described by "Q^n species" (Lin et al, 2011). "n" in the term "Q^n species" indicates the number of the bridging oxygen linked to the Si atom, i.e., how many tetrahedra (possible values: 0–4) are bonded to the tetrahedron. Quartz mainly consists of Q^3 and Q^4 species, having a high degree of polymerization, whereas hydrated species often contain Q^1 and Q^2 species, corresponding to low degrees of polymerization.

Infrared Si-O bands around 1300-800cm^{-1} are considered to be composed of several components related to the above Q^n species (García-Lodeiro et al., 2009). A band at 815cm^{-1} is corresponding to Si–O symmetric stretching vibrations in Q^1 units and a band around 970cm^{-1} to Si–OH asymmetric stretching vibrations in Q^2 units. The 1070cm^{-1} band can be assigned to Q^3 species with three oxygen atoms bridged to Si, while the 1220cm^{-1} band can be assigned to Q^4 species with four oxygen atoms bridged to Si. Therefore, the

$1220cm^{-1}/1070cm^{-1}$ peak height ratio would correspond to Q^4/Q^3 species ratio and can be expected to indicate degrees of Si-O-Si linkage with increasing polymerization.

In biogenic silica, $800cm^{-1}/950cm^{-1}$ peak height ratio has been proposed as an indicator of diagenetic transformation of biosilica (Schmidt et al 2001). However, since $950cm^{-1}$ peak due to Si-OH can disappear; I used an inverse ratio of $950cm^{-1}/800cm^{-1}$ in order not to make the ratio infinite.

Since diatom silica frustules have abundant micro- and nano-pores, effects of voids on IR micro-spectroscopy have been evaluated. Also, the void area percentages of diatoms have been determined from SEM imaging. After careful evaluation of the void effects on diatoms, IR absorption peaks and their ratios have been determined for 43 diatom samples. IR microscopic imaging has been conducted by mapping the microscopic distribution of IR peak heights and ratios for 4 representative diatom samples.

2.2. Materials and Methods

2.2.1. Materials

Centric diatoms (Diameters: 100-350μm) were taken from red algae at Kurosakinohana, near Misakiguchi station, Miura Peninsula, Kanagawa Prefecture, Japan (May, 2009). These diatoms can be classified into *Arachnoidiscus ornatus* after the description of Kobayashi et al. (1998). They were washed first by H_2O_2 (about 30 wt%) to remove organics, then by HCl (about 4 mol/l) to dissolve carbonates and finally by deionized water. Then they were mounted on a BaF_2 crystal, which is transparent in the $4000\text{-}700cm^{-1}$ region. 4 representative diatom samples were selected in this study among 43 samples: Samples A (Diameter: 177 μm), B (300 μm), C (310 μm) and D (176 μm) (Fig.2.2).

The first series of these samples, including samples B and C, were mounted on BaF_2 so as to show the exterior of the silica frustule from the top (exterior view)(Fig.2.2: B,C). The

second series, including samples A and D, were mounted on BaF_2 so as to show the interior of the silica frustule from the top (interior view) (Fig.2.2: A, D).

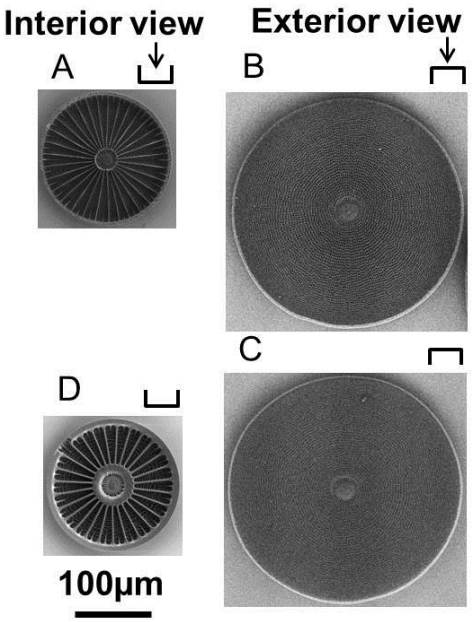

Fig.2.2. Scanning Electron Microscope (SEM) images of diatom samples A, B, C and D.

2.2.2. Methods

Infrared transmission micro-spectroscopy of diatoms was conducted by a Fourier transform IR (FT-IR) spectrometer (Jasco FTIR-620+IRT30) under the experimental conditions of 100 scans, 4cm^{-1} resolution, 4000-700cm^{-1} range and 50×50μm^2 aperture. The IR transflection micro-spectroscopy was also conducted on washed diatom samples mounted on an aluminum foil, but the 1200-1000cm^{-1} bands were strongly distorted because of longer path length. Although some corrections can be made on the transflection spectra, (Tonoue et al., 2014) these are not possible for diatoms including abundant micro and nano pores. Therefore current measurements of diatoms were conducted under transmission mode using a transparent BaF_2 disc sample support.

High resolution IR mapping with a 6.25×6.25μm^2 pixel size has been performed by IR imaging microscope (Thermo Nicolet iN10MX) under the experimental conditions of 64 scans, 8cm^{-1} resolution and 4000-700cm^{-1} range.

SEM images were obtained on the same samples on the BaF_2 crystal without carbon/metal coating under a low vacuum condition (about 50 Pa, 5kV acceleration) by SU3500 Scanning Electron Microscope (Hitachi High-Technologies).

2.3. Results:

2.3.1. IR spectra of diatom silica frustules.

A representative infrared (IR) spectrum of a diatom is shown in Fig.2.3. Absorption bands are observed at 3600cm^{-1}, 1070cm^{-1} with shoulders at 1220cm^{-1}, 950cm^{-1} and 800cm^{-1}. The 3600cm^{-1} and 950cm^{-1} bands are due to stretching of SiO-H and Si-OH bonds, respectively. The 1220cm^{-1}, 1070cm^{-1} and 800cm^{-1} bands are attributed to asymmetric and symmetric Si-O stretching vibrations, respectively (Lin et al, 2011; García-Lodeiro et al., 2009; Schmidt et al., 2001; Benning et al., 2004; Patwardhan et al., 2006; Nakashima et al., 1995; Ito & Nakashima., 2002). In the current study of diatom silica frustules, the broad Si-O band has a peak at 1070cm^{-1} with a shoulder at 1220cm^{-1}. Since 1070cm^{-1} band is considered to be due to Q^3 species with three oxygen atoms bridged to Si, while the 1220cm^{-1} band can be assigned to Q^4 species with four oxygen atoms bridged to Si (García-Lodeiro, 2009), 1220cm^{-1}/1070cm^{-1} peak height ratio can be used as an indicator of the Si-O polymerization of diatom silica frustules. While the smaller ratio of these two peak heights indicates disconnected Si-O chains, the larger value corresponds to the higher polymerization of Si-O. The 800cm^{-1}/950cm^{-1} peak height ratio has been proposed as an indicator of diagenetic transformation of biosilica (Schmidt et al, 2001). However, since 950cm^{-1} peak due to Si-OH can disappear; an inverse ratio of 950cm^{-1}/800cm^{-1} has been used in order not to make the ratio infinite.

Therefore, peak height ratios of $1220cm^{-1}/1070cm^{-1}$ and $950cm^{-1}/800cm^{-1}$ were determined as indicators of the polymerization of Si-O and Si-OH/Si-O-Si of diatom silica frustules, respectively (Fig.2.3).

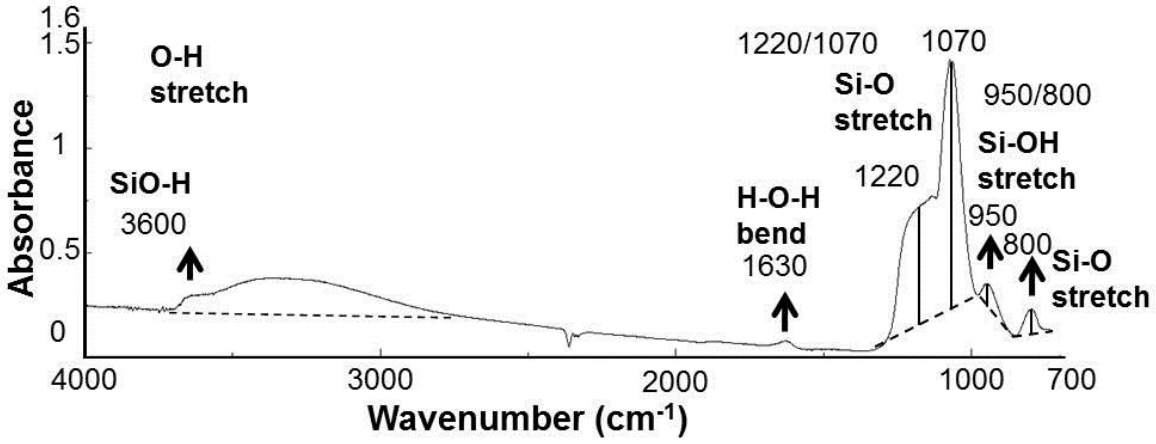

Fig.2.3. A representative IR Spectrum of a diatom silica frustule. $1220cm^{-1}/1070cm^{-1}$ and $950cm^{-1}/800cm^{-1}$ peak height ratios were determined and used in this study.

2.3.2. Void effects associated with IR micro-spectroscopy

In order to determine precise peak height ratios of $1220cm^{-1}/1070cm^{-1}$ and $950cm^{-1}/800cm^{-1}$, artefacts affecting shapes of IR absorption bands need to be evaluated first. Diatom silica frustules have generally complex microscopic morphology including many void areas such as micro- or nano-pores (Fig.2.2, Fig.2.4a). Therefore, effects of voids on the spectral band shapes must be considered.

For an absorbing material covering the aperture area (typically $50\times50\mu m^2$ area in this study) without voids (Fig.2.4b), absorbance (abs) of an IR band can be written by the Lambert-Beer law as:

$$\text{Abs} = -\log_{10}\left[\frac{I_1}{I_0}\right] \text{ and } \frac{I_1}{I_0} = 10^{-\text{Abs}} \quad (1),$$

where I_0 is the intensity of the incident beam (background spectrum), and I_1 is the transmission beam through the sample (sample spectrum).

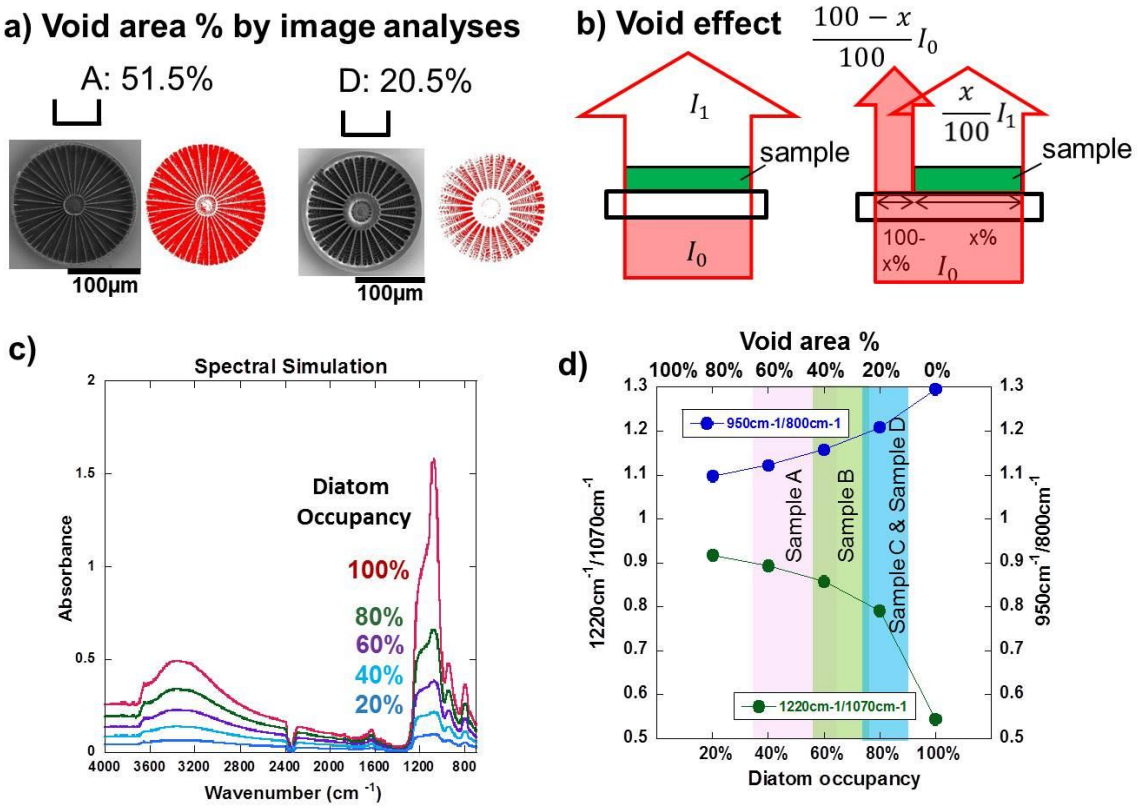

Fig.2.4. (a) SEM images of diatom samples A and D with binary images for void area% analyses. (b) Schematic illustrations of void effects on IR signal intensity I. (c) Spectral changes with diatom occupancy within the IR beam, using the spectrum at the centre of the diatom sample D to represent 100% diatom occupancy. (d) Changes in $1220cm^{-1}/1070cm^{-1}$ and $950cm^{-1}/800\ cm^{-1}$ ratios with diatom occupancy (or void area%).

If x% of the aperture is covered by the sample and the other (100-x %) is occupied by air (Fig.2.4b), absorbance can be written as the following:

$$\mathrm{Abs}' = -\log_{10}\left[\frac{\frac{x}{100}I_1 + \frac{100-x}{100}I_0}{I_0}\right] \text{ and so}$$

$$\mathrm{Abs}' = -\log_{10}\left[1 + \frac{x}{100}\left(\frac{I_1}{I_0} - 1\right)\right] \quad (2)$$

By substituting the Eq. 1 in the Eq. 2, we obtain:

$$\mathrm{Abs}' = -\log_{10}\left[1 + \frac{x}{100}\left(10^{-\mathrm{Abs}} - 1\right)\right] \quad (3)$$

As a spectral simulation to show this void effect, an IR spectrum on the central position of the sample D having less voids was used to calculate IR spectra with decreasing diatom occupancy (100, 80, 60, 40 and 20%) using the equation (3) without considering variation in light path length or scattering effects (Fig.2.4c).With increasing void area %, absorbance of all the IR bands decreased. It should be noted that the highest peak at 1070cm^{-1} showed larger attenuation than the adjacent shoulder at 1220cm^{-1}.

1220cm^{-1}/1070cm^{-1} peak height ratios for these simulated spectra were determined and plotted against the diatom occupancy (or void area %) in Fig.2.4d. The 1220cm^{-1}/1070cm^{-1} peak height ratio is about 0.54 for 100% occupancy (0% void) and increases to 0.92 for 20% occupancy (80% void) approaching 1.

950cm^{-1}/800cm^{-1} peak height ratios were also determined and plotted in Fig.2.4d. The 950cm^{-1}/800cm^{-1} peak height ratio is about 1.29 for 100% occupancy (0% void) and decreases to 1.1 for 20% occupancy (80% void) approaching 1.

2.3.3. Void area% of diatom silica frustules by image analyses.

In order to estimate void area percentages of the studied diatom samples, the SEM images were converted to binary images by using appropriate thresholds using image analysis software (ImageJ) (Fig.2.4a). The whole diatom areas contain voids of 51.5, 28.4, 20.8 and 20.5% for samples A, B, C and D, respectively (Figs. 2.4a and 2.5). The central areas of diatom contain voids of 34.9, 22.3, 16.7 and 4.2% for samples A, B, C and D, respectively (Fig.2.5). The rim areas of diatom contain voids of 62.5, 43.0, 23.7 and 23.8% for samples A, B, C and D, respectively (Fig.2.5). Therefore, the studied diatom samples can contain from 62.5 to 4.2 % of void areas which should be taken into account to evaluate their effects on the 1220cm^{-1}/1070cm^{-1} and 950cm^{-1}/800cm^{-1} peak height ratios (Fig.2.4d).

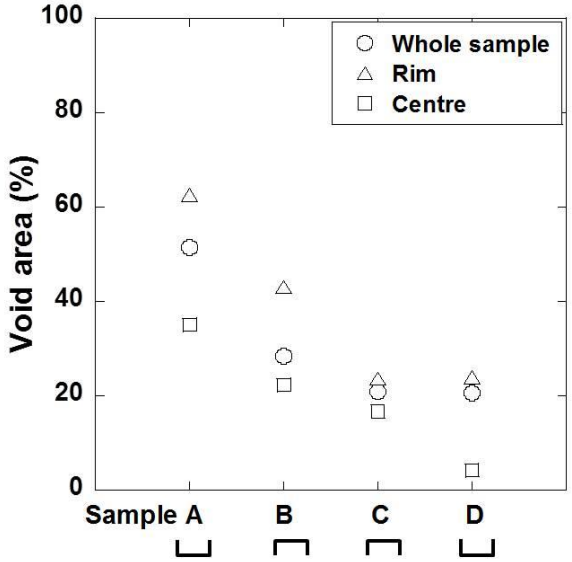

Fig.2.5. Void area percentages by image analyses for diatom samples A, B, C and D.

2.3.4. IR line profile analyses of diatom silica frustules

In order to evaluate $1220cm^{-1}/1070cm^{-1}$ and $950cm^{-1}/800cm^{-1}$ peak height ratios of diatom silica frustules while minimizing void effects, these values were determined for 4 diatom samples by IR line profile analyses deducting sample free areas at their edges (Fig.2.4b).

The $1220cm^{-1}/1070cm^{-1}$ and $950cm^{-1}/800cm^{-1}$ peak height ratios for 4 diatom samples without diatom free area in the aperture ($50\times50\mu m^2$) are shown in Fig.2.6. For sample A, $1220cm^{-1}/1070cm^{-1}$ ratio decreases from 0.35 to 0.30 at the center and it increases again to 0.34 toward the rim (Fig.2.6a). For sample B, the $1220cm^{-1}/1070cm^{-1}$ ratio is constant (0.43) throughout the location. For sample C, the $1220cm^{-1}/1070cm^{-1}$ ratio fluctuates between 0.55 to 0.51. For sample D, the $1220cm^{-1}/1070cm^{-1}$ ratio decreases from 0.61 to 0.54 at the center and increases again to 0.65 toward the rim.

$950cm^{-1}/800cm^{-1}$ ratios for sample A decrease from 1.01 to 0.86 at the centre and increase again to 0.99 toward the rim (Fig.2.6b). For sample B, $950cm^{-1}/800cm^{-1}$ ratios are around

1.2 with some fluctuation. For sample C, 950cm^{-1}/800cm^{-1} ratios are also around 1.2 and they also show some fluctuation. For sample D, it is relatively constant around 1.3.

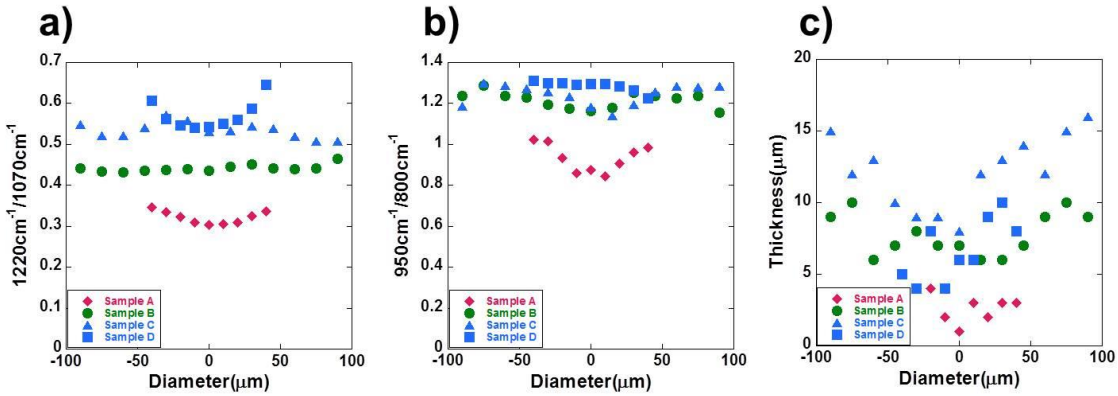

Fig.2.6. 1220cm^{-1}/1070cm^{-1} and 950cm^{-1}/800cm^{-1} peak height ratios for 4 diatom samples A, B, C and D without diatom free area in the aperture (50×50μm^2). (a) Line profiles of 1220cm^{-1}/1070cm^{-1} ratio across the centre for samples A, B, C and D. (b) Line profiles of 950cm^{-1}/800cm^{-1} ratio across the centre for samples A, B, C and D. (c) Line profiles of thickness for 4 diatom samples A, B, C and D.

Thicknesses of diatom silica frustules were determined by height differences of the top and bottom focused points under an optical microscopy along similar traverses as the IR line profile (Fig.2.6c). For sample A, the thickness varies from 1 to 4μm. The thickness of sample B ranges from 6 to 10μm. For sample C, the thickness at the centre is 8μm and increases to 16μm toward the edges. The thickness for sample D is 4 to 10μm.

2.3.5. Average values of thickness and 1220cm^{-1}/1070cm^{-1}, 950cm^{-1}/800cm^{-1} ratios of silica frustules

Since the thickness of samples A, B and D did not show systematic changes with their individual position within a sample, the average values of these were determined for 43 samples including the above 4 samples. IR absorption intensities are expected to increase with the samples thickness according to the Lambert-Beer law. Therefore, average peak

heights at 800cm^{-1} and 1070cm^{-1}, as representative absorption bands of interest, are plotted against the average thicknesses for each sample (Fig.2.7a, b).

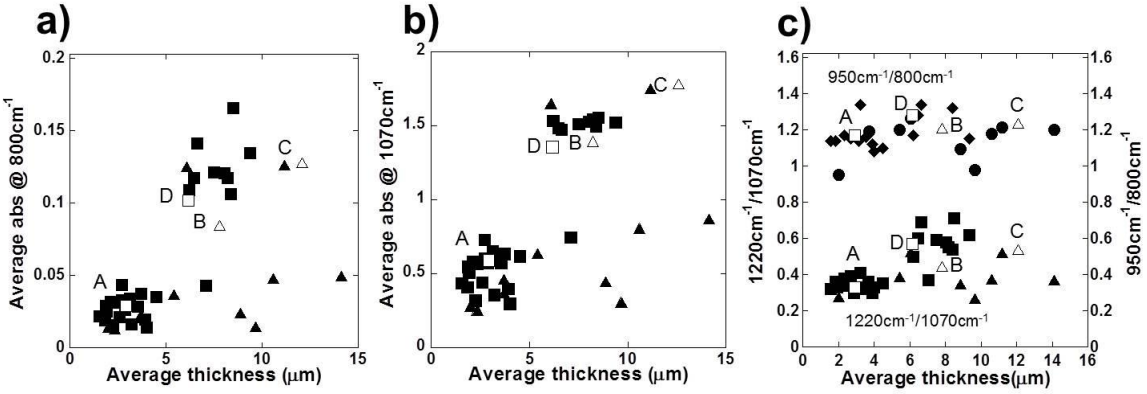

Fig.2.7. (a) Average values of 800cm^{-1} peak heights plotted against average thicknesses for 43 diatom samples. (b) Average values of 1070cm^{-1} peak heights plotted against average thicknesses. (c) Average values of 1220cm^{-1}/1070cm^{-1} and 950cm^{-1}/800cm^{-1} peak height ratios plotted against their average thicknesses. Filled rectangles and triangles are for interior and exterior views, respectively. Samples A, B, C and D are shown as corresponding open symbols.

The average peak heights at 800cm^{-1} and 1070cm^{-1} show rough positive relations with the average thickness for samples (Figs.2.7a,b) mounted to show the interior view including samples A and D (Fig.2.2, A, D). However, the data for the samples including B and C mounted to show the exterior view (Fig.2.2, B, C) demonstrate some deviations from the above trend (Figs.2.7a, b). Moreover, some exterior view samples keep similar peak heights for increasing thickness (filled triangles in Figs.2.7a, b).

Average values of 1220cm^{-1}/1070cm^{-1} and 950cm^{-1}/800cm^{-1} peak height ratios of the above line profile data for each sample are plotted in Fig.2.7c against its average thickness.

Samples A, B, C and D have average thicknesses of 2.9, 7.8, 12.1 and 6.2 μm. Their average 1220cm^{-1}/1070cm^{-1} ratios are 0.33, 0.45, 0.54 and 0.57, respectively, and their average 950cm^{-1}/800cm^{-1} ratios are 1.17, 1.21, 1.24 and 1.28, respectively.

The same analyses were conducted on 39 additional diatom samples and these data are included in Fig.2.7c. The average $1220cm^{-1}/1070cm^{-1}$ and $950cm^{-1}/800cm^{-1}$ ratios for thin samples (2-5μm thick) are from 0.29 to 0.41 and 0.95 to 1.4, respectively, while these ratios for thick samples (6-14μm thick) are from 0.37 to 0.71 and 0.98 to 1.3, respectively. These will be discussed later by considering void effects.

2.3.6. IR micro-imaging results with SEM images

Since $1220cm^{-1}/1070cm^{-1}$ and $950cm^{-1}/800cm^{-1}$ ratios of diatom samples appear to have some variations with their thicknesses (Fig.2.7c), spatial distributions of these IR peak height ratios and thicknesses should be evaluated. In order to obtain microscopic distributions of IR peak intensities, IR microscopic imaging measurements were conducted on 43 samples. Representative data are presented for the same samples A, B, C and D (Figs. 2.8-2.11).

SEM images of sample A (interior view) show four different regions: (1) the central part which is flat and dense without holes (Fig.2.8a), (2) a ring structure surrounding the centre connected by elongated holes (central ring) (Fig.2.8a), (3) mesh-like hole-bearing structures (body) with radially elongated rods (costa) (Fig.2.8a, b, c) and (4) a thick rim part with fewer holes (Fig.2.8a, c). The radial rods (costa) can be classified into at least two different types. The first type of rods connects the center to the rim (primary costa). The second type of rods are in contact with the rim, between two primary rods, and taper away from 10-20μm (secondary costa) (Fig.2.8a, c). The pores (areola) in the mesh-like structures in the body fill the spaces among these primary and secondary costa.

IR imaging of sample A show that the absorbance at $800cm^{-1}$ (Si-O-Si) is largest at the center and central ring (0.03-0.042) with smaller values (0.02-0.032) within the body and rim parts (Fig.2.8d). Absorbance at $950cm^{-1}$ (Si-OH) for this sample A have their largest values (0.028-0.044) at the central ring together with some larger values at the radial cones (costa) and at the rim, while this value at other parts is about 0.018-0.035 (Fig.2.8e). The

950cm^{-1}/800cm^{-1}peak height ratio show two larger zones parallel to the IR scanning direction (Fig.2.8f). This may be related to erroneous ratio values due to very small absorbance at 800cm^{-1} at these portions (Fig.2.8d) but may also be caused by different sensitivities of the IR linear array sensor (16 channel MCT detectors). The 950cm^{-1}/800cm^{-1} peak height ratio is generally in the 1.0- 1.7 range throughout the sample (Fig.2.8f). The 1220cm^{-1}/1070cm^{-1}peak height ratio shows smaller values (~0.22) at the very centre but relatively constant values (around 0.37) for other regions, and values up to 0.38-0.42 for the rim part (Fig.2.8g).

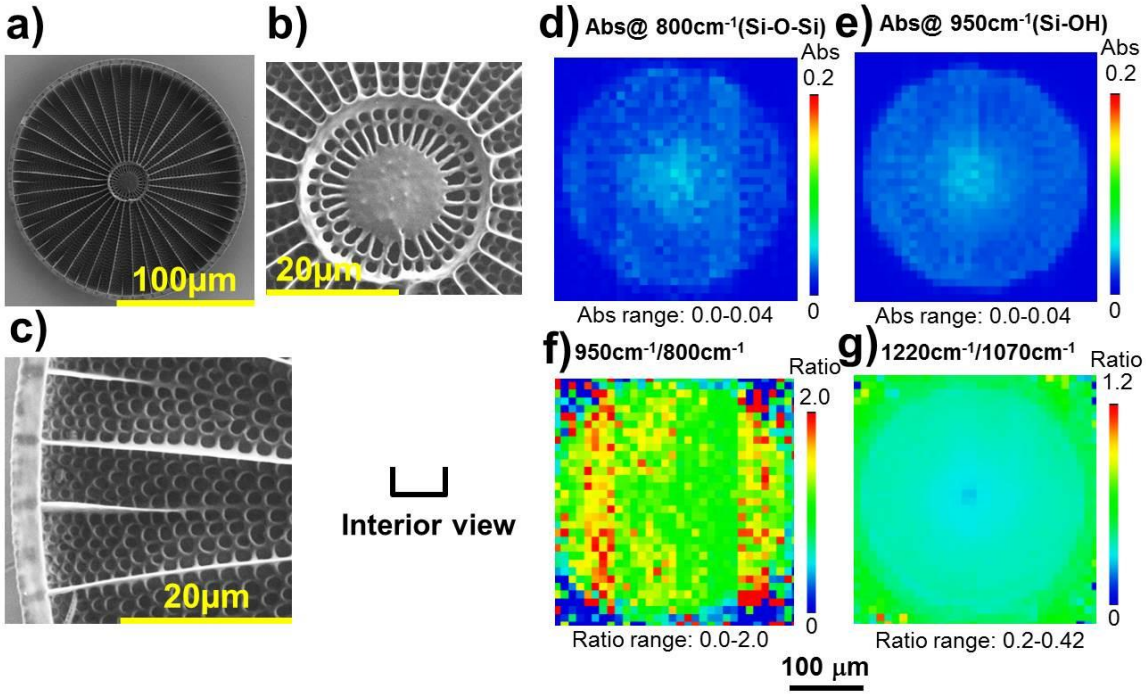

Fig.2.8. SEM images of sample A (Interior view). (a) Whole image. (b) Close up of the central part. (c) Close up of the rim part. IR imaging data for sample A with value ranges (high: red – low: blue). (d) Absorbance at 800 cm^{-1} (Si-O-Si). (e) Absorbance at 950cm^{-1} (Si-OH). (f) 950cm^{-1} /800cm^{-1} peak height ratio. (g) 1220cm^{-1}/1070cm^{-1} peak height ratio.

SEM images of sample B (exterior view) show four different regions: (1) the central part which is rather flat and dense without holes (Fig.2.9b), (2) a ring structure surrounding the centre with elongated holes (central ring) (Fig.2.9b), (3) mesh-like hole-bearing structures (body) (Fig.2.9a, b, c) and (4) a thick rim part with some holes (Fig.2.9a, c). The radial rods (costa) are not clear from this exterior view (Fig.2.9a) but can be recognized at the body (Fig.2.9c). The holes in the body appear to contain some fine solids (Fig.2.9b, c). These fine silica phases are considered to be excrements from the organism (Sumper & Kröger, 2004).

IR imaging of sample B shows that absorbance at 800cm^{-1} (Si-O-Si) is largest at the central ring (0.1-0.12) with smaller values (0.05-0.09) elsewhere in the body (Fig.2.9d). Radial costa at the body and rim appear to show some larger values (0.09-0.11). Absorbance at 950cm^{-1} (Si-OH) for this sample B have large values (0.13-0.15) at the central ring together with some larger ones at the radial cones (costa) and at the rim (0.1-0.13), while this value elsewhere is about 0.06-0.11 (Fig.2.9e). The 950cm^{-1}/800cm^{-1} peak height ratio is larger in the middle parts (1.4-1.9), with values of 0.8-1.5 elsewhere (Fig.2.9f). The 1220cm^{-1}/1070cm^{-1} peak height ratio shows relatively constant values (~0.5) throughout the sample with larger values at the rim (~0.9) (Fig.2.9g). However, this can be related to the void effect.

SEM images of sample C (exterior view) show four different regions: (1) the central part which is flat and dense without holes (Fig.2.10b), (2) a ring structure surrounding the centre with elongated holes (central ring) (Fig.2.10b), (3) mesh-like hole-bearing structures (body) (Fig.2.10a, b, c) and (4) a thick rim and some holes (Fig.2.10a,c). The radial rods (costa) are not clear from this exterior view (Fig.2.10a) but they can be recognized at the body (Fig.2.10c). The holes in the body have well developed fine branching structures (Fig.2.10b, c).

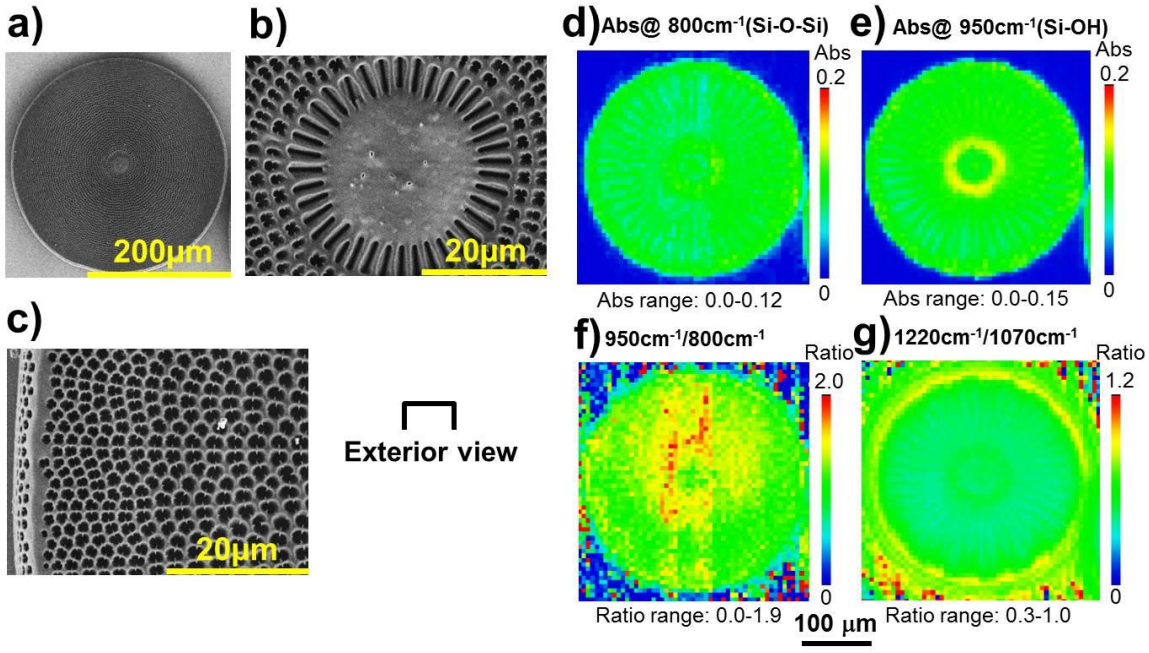

Fig.2.9. SEM images of sample B (Exterior view). (a) Whole image. (b) Close up of the central part. (c) Close up of the rim part. IR imaging data for sample B with value ranges (high: red – low: blue). (d) Absorbance at 800cm^{-1} (Si-O-Si). (e) Absorbance at 950cm^{-1} (Si-OH). (f) 950cm^{-1}/800cm^{-1} peak height ratio. (g) 1220cm^{-1}/1070cm^{-1} peak height ratio.

IR imaging of sample C shows that the absorbance at 800 cm^{-1} (Si-O-Si) is largest at the central ring (0.16-0.18) with smaller values in the body (0.07-0.12) and rim (0.11-0.15)(Fig.2.10d). Radial costa appear to show some larger values at the body (0.12-0.15). Absorbance at 950cm^{-1} (Si-OH) for this sample C is largest (0.17-0.2) at the central ring together with some larger ones at the radial cones (costa) and at the rim (0.13-0.18), while this value elsewhere is about 0.07-0.14 (Fig.2.10e). The 950cm^{-1}/800cm^{-1} peak height ratio is larger in the middle parts (1.2-1.7) with values of 0.8-1.5 elsewhere (Fig.2.10f). The 1220cm^{-1} /1070cm^{-1} peak height ratio is 0.55-0.7 for the body and shows larger values at the central ring and some costa (0.8-0.9) and becomes largest at the rim (~1.2) (Fig.2.10g). However, this can be related to the void effect.

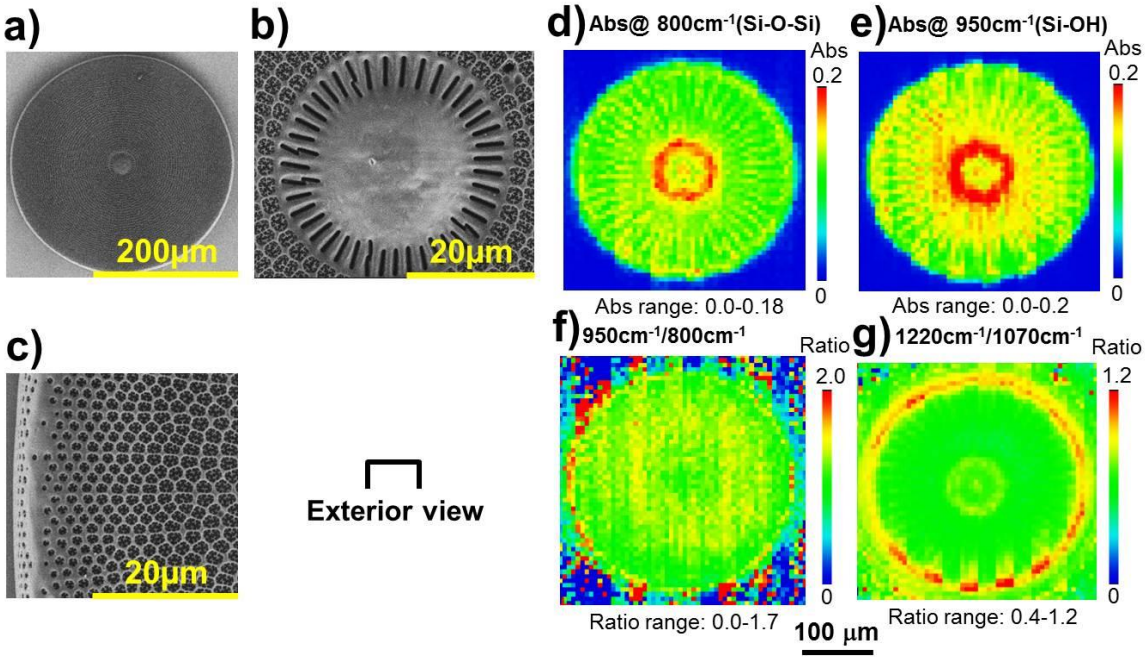

Fig.2.10. SEM images of sample C (Exterior view). (a) Whole image. (b) Close up of the central part. (c) Close up of the rim part. IR imaging data for sample C with value ranges (high: red – low: blue). (d) Absorbance at 800cm^{-1} (Si-O-Si). (e) Absorbance at 950cm^{-1} (Si-OH). (f) 950cm^{-1} /800cm^{-1} peak height ratio. (g) 1220cm^{-1}/1070cm^{-1} peak height ratio.

SEM images of sample D (interior view) show four different regions: (1) the central part which is rather flat and dense without holes (Fig.2.11b), (2) a prominent ring structure surrounding the centre connected by elongated holes (central ring) (Fig.2.11b), (3) mesh-like hole-bearing structures (body) with radially elongated rods (costa) (Fig.2.11a, b, c) and (4) a well-developed thick rim with fewer holes (Fig.2.11a, c). The radial rods (costa) can be classified into at least two different types. The first type of rods connects the centre and rim (primary costa). The second type of costa connects with the rim tapering away after 10-20 µm (secondary costa) (Fig.2.11a, c). In the broken part, a third type of rod (tertiary costa) can be detected growing from the rim for about 5µm (Fig.2.11a). The pores (areola) in the mesh-like structures in the body fill spaces among these primary and secondary costa.

IR imaging of sample D shows that the absorbance at 800cm^{-1} (Si-O-Si) is largest at the central ring (0.11-0.13) with smaller values characteristic of the body (0.05-0.11) and rim (0.07-0.1). Radial costa have larger values in the body (0.1-0.12) (Fig.2.11e). Absorbance at 950cm^{-1} (Si-OH) for this sample D is largest (0.13-0.16) at the central ring with absorbances of 0.11-0.14 at the rim and low values elsewhere (0.07-0.1) (Fig.2.11f). The 950cm^{-1}/800cm^{-1} peak height ratio is larger in the middle parts of the sample (1.2-1.8), while absorbance ratio values are 0.9-1.5 elsewhere (Fig.2.11g). The 1220cm^{-1}/1070cm^{-1} peak height ratio is 0.5-0.8 for the body and shows larger values at the central ring and some costa (~0.9), taking on the largest values at the rim (1-1.2) (Fig.2.11h). However, this can be related to the void effect.

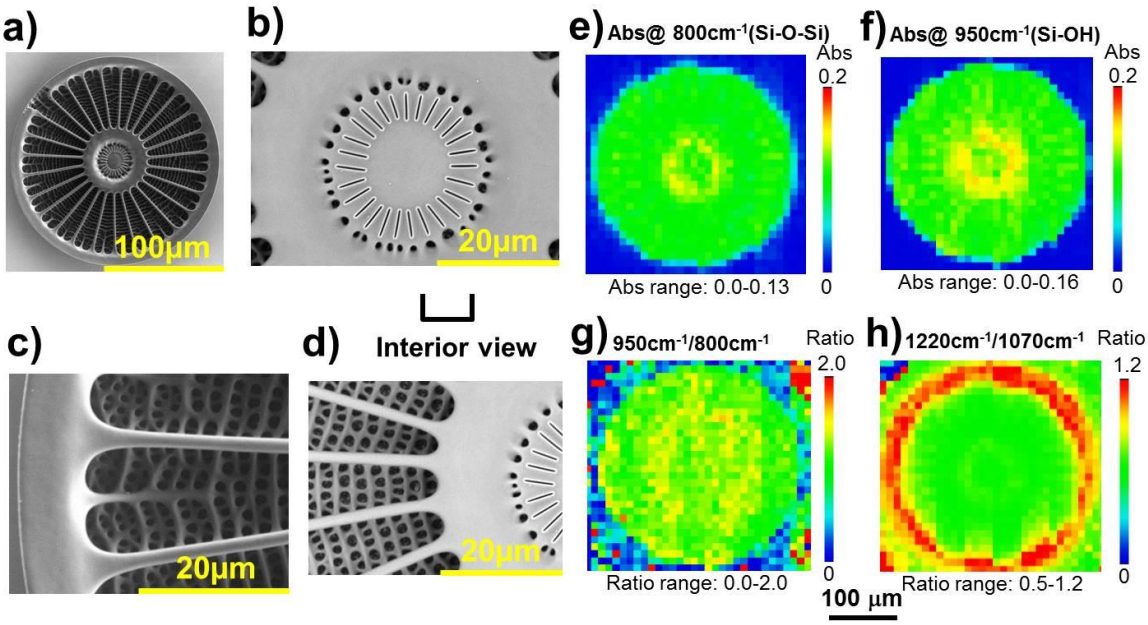

Fig.2.11. SEM images of sample D (Interior view). (a) Whole image. (b) Close up of the central part. (c) Close up of the rim part. (d) Close up of the body and central part. IR imaging data for sample D with value ranges (high: red – low: blue). (e) Absorbance at 800cm^{-1} (Si-O-Si). (f) Absorbance at 950cm^{-1} (Si-OH). (g) 950cm^{-1}/800cm^{-1} peak height ratio. (h) 1220cm^{-1}/1070cm^{-1} peak height ratio.

2.3.7. Raman micro-imaging of diatoms

Raman micro-imaging results on a diatom sample mounted on BaF_2 (interior view) show the presence of 950cm^{-1} Raman band due to Si-OH in agreement with the IR results but with higher spatial resolution (Fig.2.12a, b). By comparing with SEM images of the same sample (Fig.2.12c, d), costa are containing Si-OH species.

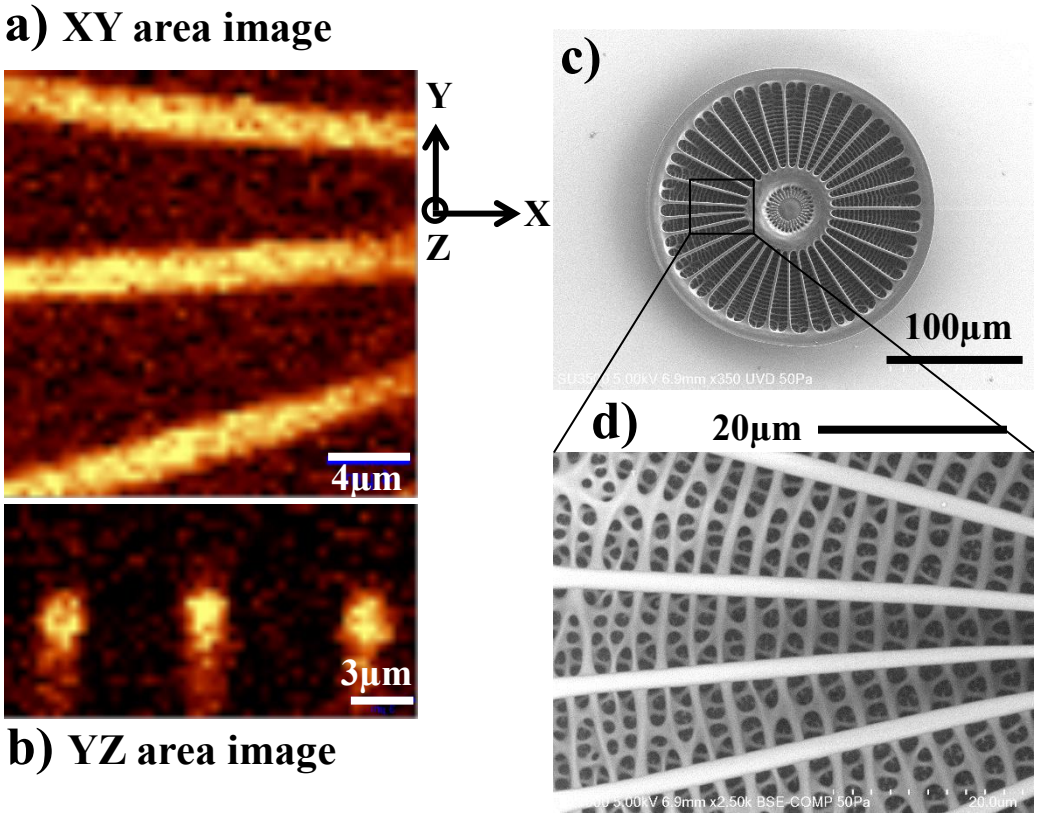

Fig.2.12 : (a, b) Raman band images and (c, d) SEM images of an adult diatom sample (interior view).

Similar Raman images are also obtained from exterior view of another sample also mounted on BaF_2 (Fig.2.13b, c).

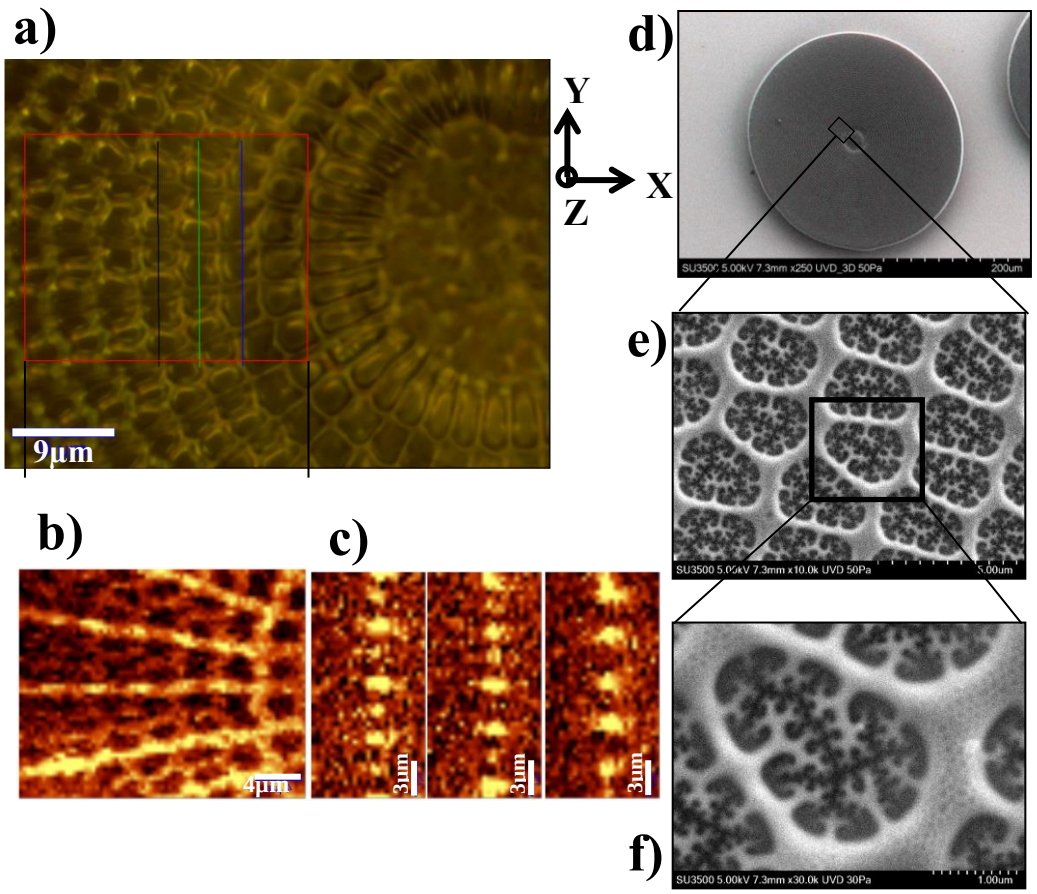

Fig.2.13 : (a) Optical image of an adult diatom (exterior view), (b) Raman SiOH (970cm^{-1}) band area image at XY vector, (c) Raman SiOH (970cm^{-1}) band area image at YZ vector, (d, e, f) SEM images of the same sample (exterior view).

2.4. Discussion

2.4.1. Void effects in IR spectra of microscopic porous structures of diatoms

The void effects on IR spectra of porous materials have been simulated by using the IR spectrum of the central position of the sample D having less voids with increasing void area percentages (20, 40, 60, 80 and 100 %) (Fig.2.4c). With increasing void area %, absorbance of all the IR bands decreased (Fig.2.4c), 1220cm^{-1}/1070cm^{-1} peak height ratios increased

from about 0.54 (0% void) to 0.92 (80% void), approaching 1 and $950cm^{-1}/800cm^{-1}$ peak height ratios decreased from 1.29 (0% void) to 1.1 (80% void), approaching 1 (Fig.2.4d).

Void area% of diatom silica frustules were determined by the SEM image analyses on 4 representative samples A, B, C and D (Fig.2.5). Void area% of the whole diatom decreased from 51.5, 28.4, and 20.8 to 20.5% for the samples A, B, C and D (Fig.2.5). The central areas contain fewer voids, while the rim areas include more voids up to 62.5% for the sample A (Fig.2.5).

For sample A, the $1220cm^{-1}/1070cm^{-1}$ ratio was the smallest at the centre (0.30) and increased toward the rim (0.35) (red diamonds in Fig.2.6a). This can be explained by larger void area% at the rim (up to 62.5%) than the void area % of the centre (34.9%) (Fig.2.4d and Fig.2.5). The $950cm^{-1}/800cm^{-1}$ ratio for sample A was the smallest at the centre (0.87) and increased toward the rim (~1) (red diamonds in Fig.2.6b). This trend is opposite to the void effect (Fig.2.4d). Although the $1220cm^{-1}/1070cm^{-1}$ ratios are subject to the void effect, the $950cm^{-1}/800cm^{-1}$ ratio can indicate the real structural information of silica.

For sample B, the $1220cm^{-1}/1070cm^{-1}$ ratio was relatively constant around 0.43 (green circles in Fig.2.6a), despite the largest void area % at the rim (up to 43%) than at the centre (22.3%) (Fig.2.5). The $950cm^{-1}/800cm^{-1}$ ratio for sample B showed a slight increase from the centre toward the rim (green circles in Fig.2.6b), opposite of the void effect trend (Fig.2.4d).

For sample C, the $1220cm^{-1}/1070cm^{-1}$ ratio showed some variations around 0.54 (blue triangles in Fig.2.6a). The void area% of this sample C showed a small variation of void area% at the centre (16.7%) and the rim (23.7%) (Fig.2.5). The $950cm^{-1}/800cm^{-1}$ ratio for sample C showed a slight increase from the centre toward the rim (blue triangles in Fig.2.6b), opposite of the void effect trend (Fig.2.4d).

For sample D, the $1220cm^{-1}/1070cm^{-1}$ ratio increased from the centre (0.54) to the rim (0.65) (blue rectangles in Fig.2.6a). The void area% of this sample D was smallest at the centre (4.2%) and larger at the rim (23.8%) (Fig.2.5). Therefore, the increase of the

$1220cm^{-1}/1070cm^{-1}$ ratio from the centre to the rim can be explained by the void effect (Fig.2.4d). The $950cm^{-1}/800cm^{-1}$ ratio for sample D was relatively constant around 1.29 (blue rectangles in Fig.2.6b).

These results indicate that while the $1220cm^{-1}/1070cm^{-1}$ ratios are sometimes subject to the void effect, the $950cm^{-1}/800cm^{-1}$ ratio can indicate the real structural information of silica.

2.4.2. Maturity of diatom silica frustules in relation to void area %, thickness, $1220cm^{-1}/1070cm^{-1}$ and $950cm^{-1}/800cm^{-1}$ peak height ratios

The void area % shows a decreasing trend for the samples A, B, C and D (Fig.2.5). However their diameters do not follow the same sequence: samples A (177 µm), B (300 µm), C (310 µm) and D (176 µm) (Fig.2.2). Samples A and D are viewed from the interior looking inside a petri dish-like box while samples B and C are viewed from the exterior looking at the cover. The same views show similar diameters (Fig.2.2).

The diatom unicellular body is tightly encased in a cell wall (called a frustule) composed of amorphous silica containing a small portion of organic macromolecules (Hecky et al, 1973; Parkinson & Gordon, 1999; Nakajima & Volcani, 1969; Pickett-Heaps et al, 1990; Vrieling et al, 2000). The top half valve (epivalve) and its side wall, together, are called the epitheca, which covers a slightly smaller bottom half valve (hypovalve) with its side wall termed the hypotheca just like a petri dish-like box and its upper cover (Kröger & Sumper, 2004; Pickett-Heaps et al, 1990) (Fig.2.1b). Fine structures of these epitheca and hypotheca provide characteristic structures of a given species (Hildebrand, 2008).

Reproduction in diatoms is mostly asexual by binary fission, where each daughter cell receives one of the two frustules of the parent cell. This is used by each daughter cell as the larger frustule into which a second small frustule is constructed inside (Kröger & Sumper, 2004; Hildebrand, 2008; Sumper & Kroger, 2004; Round et al, 1990; Kroger, 2007; Scheffel et al 2011) (Fig.2.1b). This form of division results in a size reduction of the

daughter cell receiving the smaller frustule from the parent and therefore the average cell size of a diatom population decreases (Fig.2.1b), until the cells are about one-third their maximum size (Hasle & Syvertsen, 1996). Therefore, the diameters of diatom frustules do not indicate the maturity of the life stages.

On the other hand, during the growth of a diatom, silica is considered to be deposited increasingly on thin organic layers ((Mann, 2001; Hecky et al, 1973) (Fig.2.1a). Therefore, thicker and denser silica structures are expected for more mature diatoms.

The average thickness of sample C is larger than that of B (exterior view) (Fig.2.7). The valve thickness on the exterior view (B, C) under the microscope might be overestimated due to the thick wall at the rim standing on the BaF_2 crystal. Since the void area percentages of the sample C are slightly smaller than those of the sample B (Fig.2.5), the maturity might be slightly larger for C, in agreement with the thickness order (Fig.2.7).

The average thickness of sample D is larger than that of A (interior view) (Fig.2.7). Since the void area percentages of sample D are smaller than those of the sample A (Fig.2.5), the maturity is considered to be larger for D than that of A, in agreement with the thickness order (Fig.2.7).

Average $950cm^{-1}/800cm^{-1}$ ratios are larger for D (1.28) than A (1.17) and slightly larger for C (1.24) than B (1.21) (Fig.2.7c). Because of the larger void area % for A (51.5%) than D (20.5%) and for B (28.4%) than C (20.8%) (Fig.2.5), this larger $950cm^{-1}/800cm^{-1}$ ratios for samples D (>A) and C (>B) can be explained by the void effect (Fig.2.4d). Since the average $950cm^{-1}/800cm^{-1}$ ratios do not show a systematic variation with the average thickness (Fig.2.7c), this ratio cannot be a good indicator of silica maturation.

Average $1220cm^{-1}/1070cm^{-1}$ ratios are larger for D (0.57) than A (0.33) and larger for C (0.54) than B (0.45) (Fig.2.7c). Because of the larger void area % for A (51.5%) than D (20.5%) and B (28.4%) than C (20.8%) (Fig.2.5), these larger $1220cm^{-1}/1070cm^{-1}$ ratios for samples D (>A) and C (>B) cannot be explained by the void effect (Fig.2.4d) and may be related to the structural changes of silica. Except for exterior view samples (filled triangles

in Fig.2.7c), the 1220cm^{-1}/1070cm^{-1} ratio shows an increasing trend with the average thickness. Therefore, increasing silica transformation can be expected for thicker diatoms.

According to these results, maturity of diatom silica frustules can be discussed based on the void area percentages, average thicknesses and average values of 1220cm^{-1}/1070cm^{-1} peak height ratios. Tentatively, by the order of the void area%, the maturities of 4 representative samples are in the following order: A < B < C < D (Fig.2.5). Although the average thicknesses have some overestimation, especially for the exterior view samples (Fig.2.2), this order is also in agreement with the 1220cm^{-1}/1070cm^{-1} peak height ratio (Fig.2.7c).

2.4.3. Growth of diatom silica frustules based on SEM and IR images

The void area percentages by SEM, average thicknesses by optical microscope and average values of 1220cm^{-1}/1070cm^{-1} peak height ratios by IR micro-spectroscopy suggested that maturities of 4 representative samples are in the following order: A< B < C < D (Fig.2.5).

Since the larger 1220cm^{-1}/1070cm^{-1} peak height ratio can correspond to maturity of diatom silica frustules, silica polymerization reaction might proceed during the maturation process.

The growth of diatom silica frustules is considered to occur from the centre toward the rim (Pickett-Heaps et al., 1990; Mayama & Kuriyama, 2002) and small pore spaces are increasingly filled with further silica (Sumper, 2002; Kröger & Sumper, 2004; Sumper & Kröger, 2004). Therefore, structural maturation of silica might also occur inside a single diatom. Microscopic heterogeneities of chemical structures of silica by means of the 1220cm^{-1}/1070cm^{-1} and 950cm^{-1}/800cm^{-1} ratios obtained by IR microscopic imaging on the representative samples A, B, C and D (Figs. 2.8-11) will be discussed here.

For sample A, IR imaging data did not show significant heterogeneities in the 1220cm^{-1}/1070cm^{-1} (0.2-0.42) and 950cm^{-1}/800cm^{-1} ratios (1.0-1.7) (Fig.2.8g, f). It should be noted

that the 1220cm^{-1}/1070cm^{-1} peak height ratio shows smallest values (~0.22) at the very centre (Fig.2.8g). Since this sample is considered to be immature, based on its abundant voids and thin thickness, chemical structure of silica is also expected to be immature with smaller 1220cm^{-1} /1070cm^{-1}peak height ratios (less polymerization) than other samples. The smallest 1220cm^{-1} /1070cm^{-1} peak height ratio at the central position may suggest that the growth of silica frustules possibly occur from the centre, as is suggested by biologists (Pickett-Heaps et al., 1990; Mayama & Kuriyama, 2002).

For sample B, the 1220cm^{-1}/1070cm^{-1} peak height ratio shows relatively constant values (~0.5) throughout the sample (Fig.2.9g). On the other hand, the 950cm^{-1} /800cm^{-1} peak height ratios are larger in the middle parts (1.4-1.9) than they are in the other parts (0.8-1.5) (Fig.2.9f). The middle portion of sample B has a similar void area% (~22.3%) to the body average (Fig.2.5) and the void effect on this peak height ratio should give smaller values for increasing void% (Fig.2.4d). Therefore, the larger 950cm^{-1}/800cm^{-1} peak height ratios at the middle part of sample B indicate larger Si-OH/Si-O-Si ratios at the middle parts corresponding to more hydrated amorphous nature of silica.

For sample C, the 1220cm^{-1}/1070cm^{-1} peak height ratio is around (0.55-0.7) for the body and shows larger values at the very centre, central ring and some costa (0.8-0.9) (Fig.2.10g). This result indicates that silica polymerization is significant for these portions. The 950cm^{-1}/800cm^{-1} peak height ratio is larger at the middle parts (1.2-1.7), while the other parts have the values of 0.8-1.5 (Fig.2.10f). This area with larger Si-OH/Si-O-Si ratios may correspond to more hydrated amorphous silica in immature regions. This may be related to fine, pore-filling structures observed by SEM in these middle parts (Fig.2.10b, c). This kind of nanoscopic silica droplet (50-300nm) deposition has been reported in a different diatom species (*Coscinodiscus Wailesii*) (Sumper, 2002; Kröger & Sumper, 2004).

For sample D, the 1220cm^{-1} /1070cm^{-1} peak height ratio is around 0.5-0.8 for the body and has larger values at the central ring and some costa (~0.9) (Fig.2.11h). The 950cm^{-1} /800cm^{-1} peak height ratios are larger in the middle parts (1.2-1.8) than they are for other

parts (0.9-1.5) (Fig.2.11g). These results are mostly similar to sample C and the more hydrated amorphous immature silica might be present in the central region.

Based on the above mentioned results, the following working hypotheses for the formation processes of diatom silica frustules are proposed:

(1) Hydrated amorphous silica is deposited possibly on organic layers as is suggested by Hecky et al. (1973) (Fig.2.1a). Because the amino acids show high percentages of OH (serine, threonine; Hecky et al., 1973), dissolved $Si(OH)_4$ is considered to be deposited on protein layers through the dehydration reaction with OH-bearing amino acids. These primary silica layers have a high Si-OH/Si-O-Si ratio (large $950cm^{-1}/800cm^{-1}$ peak height ratio) and low degree of Si-O polymerization (small $1220cm^{-1}/1070cm^{-1}$ peak height ratio) (Fig.2.1a).

(2) During growth processes of silica frustules, leading to thicker silica layers (Fig.2.7), more dehydrated and polymerized silica layers are supposed to be developed (Fig.2.1a). The mechanisms responsible for these dehydration-polymerization reactions (Si-OH + HO-Si → Si-O-Si) are not known but may include some enzymes and/or catalysts (Kröger, 2007; Kröger & Sumper, 2000; Belton et al, 2008; Kröger & Sandhage, 2010).

(3) On the other hand, branching structures filling voids (Fig.2.10b,c) are supposed to occur by a secondary process which deposits hydrated amorphous silica on their growing surfaces (Sumper, 2002; Kröger & Sumper, 2004; Sumper & Kröger, 2004). During the growth of diatoms, thickening of silica frustules proceeds as the Si-OH/Si-O-Si ratio ($950\ cm^{-1}/800\ cm^{-1}$ peak height ratio) decreases and the degree of Si-O polymerization ($1220\ cm^{-1}/1070\ cm^{-1}$ peak height ratio) is increased (Fig.2.7c).

Further maturation of silica frustules occurs with increasing branching structures filling voids (decreasing void area% in Fig.2.5) and these branched structures are abundant at the middle ring portions (Fig.2.10b, c). Therefore, the branched portions show larger Si-OH/Si-O-Si ratios ($950cm^{-1}/800cm^{-1}$ peak height ratio) in the IR maps (Fig.2.10f).

Although further studies are needed to elucidate mechanisms of silica deposition and its growth in the presence of biomolecules (biomineralization), which are not well known (Mann, 2001; Sumper, 2002; Kröger & Sumper, 2004; Mount et al, 2004; Hildebrand, 2008; Tesson &Hildebrand, 2013), the present IR micro-spectroscopic data, with careful void effect evaluation, will be a valuable new tool for determining physicochemical structures of silica in micro-scale.

2.5. Conclusion

In order to characterize a representative natural bionanomaterial, present day centric diatom samples (Diameter: 100-350μm) have been measured by infrared (IR) micro-spectroscopy and Scanning Electron Microscopy (SEM). The following results were obtained:

(1) Since diatom silica frustules have complex microscopic morphology including many void areas such as micro- or nano-pores, the effects of voids on the spectral band shapes were first evaluated. With increasing void area %, $1220cm^{-1}/1070cm^{-1}$ peak height ratios increased and $950cm^{-1}/800cm^{-1}$ peak height ratios decreased both approaching 1. This void effect should be carefully evaluated for IR micro-spectroscopy of micro/nano-porous materials.

(2) Void area% of diatom silica frustules were determined by the SEM image analyses on 4 representative samples A(51.5%), B(28.4%), C(20.8%) and D(20.5%). The central areas contain fewer voids, while the rim areas include more voids.

(3) Based on the void area% of these samples and simulated trends of the $1220cm^{-1}/1070cm^{-1}$ and $950cm^{-1}/800cm^{-1}$ peak height ratios, the $1220cm^{-1}/1070cm^{-1}$ ratios of diatom samples are sometimes affected by the void effect, but the $950cm^{-1}/800cm^{-1}$ ratio is likely to indicate the real structural information of silica.

(4) The void area percentages determined by SEM, average thicknesses obtained by optical microscope and average values of $1220cm^{-1}/1070cm^{-1}$ peak height ratios (opposite trend

to the void effect) determined by IR micro-spectroscopy suggest that maturities of 4 representative samples are in the following order: A< B < C < D.

(5) The 1220cm^{-1}/1070cm^{-1} peak height ratio can be considered as an indicator of silica polymerization, when the void effects are minor.

(6) Microscopic heterogeneities of chemical structures of silica were obtained by IR micro-spectroscopic mapping of representative diatoms. The 950cm^{-1}/800cm^{-1} ratios show larger central portions of some diatoms that correspond to more hydrated amorphous immature silica.

(7) Based on IR mapping and SEM microscopy, the microscopic distribution of physicochemical structures of diatom silica frustules can be determined and they provide a means of studying formation mechanisms of bionanomaterials (biomineralization).

The present IR micro-spectroscopic data with careful void effect evaluation will be a valuable new tool for determining physicochemical structures of silica in micro scale.

Chapter 3. Changes in aliphatic CH species during in-situ heating IR microspectroscopy of unwashed diatoms

3.1 Introduction

Dead bodies of marine diatoms are sedimented on the ocean floor and buried in marine sediments with time. During their burial, temperature and pressure increase and organic components in diatom bodies are transformed. Silica is also transformed from amorphous hydrous silica (Opal-A) via cristobalite (Opal-C) to quartz (Qz) (Pollastro, 1993). These burial processes are subdivided into three phases: diagenesis, catagenesis and metagenesis (Berner, 1980; Tissot and Welt, 1984). These stages include complex processes such as compaction, heat-, fluid- and mass-flow, together with reaction kinetics (Hantschel and Kauerauf, 2009).

Diatoms are considered as one of major sources of oil and gas together with other small aquatic organisms such as radiolaria and foraminifera (Aoyagi & Omokawa 1992; Aoyagi & Omokawa 1993, Theriot, 2012; Levitan et al 2014). Generation of hydrocarbons is considered to be related to transformation of organic components in aquatic organisms such as diatoms during the burial-diagenesis (Tissot and Welt, 1984). The degree of organic transformation is often reported by maturation parameters, such as vitrinite reflectance, molecular biomarkers and mineral diagenesis (Hantschel and Kauerauf 2009).

Evaluation of hydrocarbon generation potentials has been conducted often by using reaction kinetics of kerogen (complex sedimentary organic matter) to understand quality and quantity of petroleum and natural gas (Behar et al., 1997; Burnham et al., 1989; Dieckmann et al., 2000). Most of experimental simulations of hydrocarbon generation reactions have been conducted at high temperatures (500^{o}C -350^{o}C) resulting in wide ranges of rates and activation energies (Behar et al., 1997; Burnham et al., 1989; Dieckmann et al., 2000; Tonoue, PhD thesis 2015). These varying values give a very large range of time scales for hydrocarbon generation by their extrapolation to lower temperatures of 70^{o}C to 150^{o}C (natural hydrocarbon reservoir conditions). Although some

catalytic effects of minerals on rapid hydrocarbon generation have been suggested (Johns, 1979; Wei et al, 2006), few quantitative evaluation were reported. In particular, detailed kinetic studies of organic transformation processes during burial and diagenesis of diatomaceous sediments have not been simulated experimentally by using diatoms themselves as the source rock.

In this study, thermal transformation of diatom frustules are studied by in situ heating experiments under a Fourier transform infrared (FT-IR) spectrometer and kinetic parameters (reaction rate constants and activation energies) have been evaluated. A Transflection-mode FTIR spectroscopy was employed here for measuring IR spectra of diatom frustules on Al plate in a heating stage. This transflection method is often used for measuring spectra of biological and other samples mainly because of higher absorbance due to a double pass length through the same sample, and also due to relative low cost of sample support substrates such as Al compared to transmission windows such as CaF_2 and BaF_2 (Bassan et al., 2012).

3.2 Materials:

Centric diatoms (Diameters: 100-350 μm) were taken from red algae at Kurosakinohana, near Misakiguchi station, Miura Peninsula, Kanagawa Prefecture, Japan (May, 2009). These diatoms can be classified into *Arachnoidiscus ornatus* after the description of Kobayashi et al. (1998). They were not washed but just dried in ambient air. One diatom particle was taken from these dried unwashed diatoms and mounted on an Al plate. The Al plate of about 5mm in diameter was cut from the Al plate of about 1 mm (100μm) thick and pressed by a hand press to flatten. The diatom was mounted on an Al plate without using any adhesive for measuring IR spectral changes at a high temperature.

3.3 Methods:

3.3.1. In situ isothermal heating experiments by micro-FTIR spectroscopy

In order to examine IR spectral changes with heating of unwashed diatoms, a single diatom mounted on an Al plate then placed in a heating stage (Linkam TS-1500)(Fig.3.1). The heating stage was set under an IR microscope connected to a Fourier transform IR spectrometer (FT-IR) (FTIR-620+IRT30, JASCO Co., Ltd). The temperature of the sample was monitored just below the Al plate and increased at a rate of 50^{o}C/minute up to the desired temperature (260, 270, 280, 290 or 300°C). Since no window materials were set in the heating stage, the diatom sample was heated in an ambient air atmosphere.

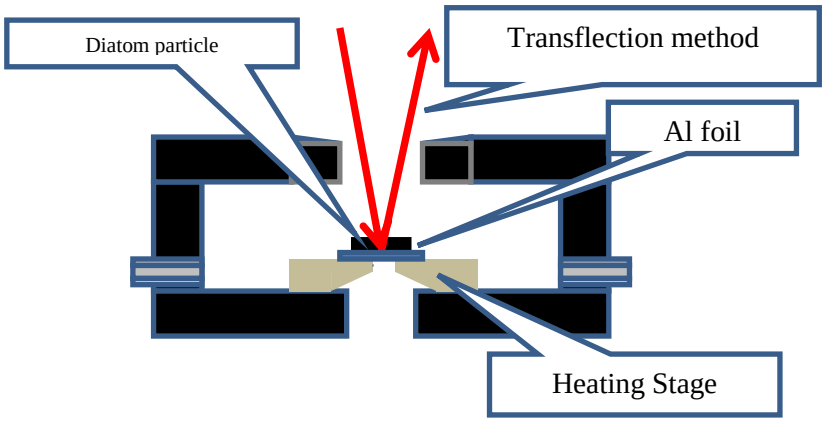

Fig. 3.1. Schematic figure of heating stage (Linkam 1500) used in this study.

The FT-IR has a ceramic IR light source, Ge coated KBr beam-splitter, a Mercury-Cadmium-Telluride (MCT) detector. The IR microscope has two ×16 Cassegrainian mirrors as focusing units.

A background reflection spectrum on a 100×100μm^2 aperture area was first measured on a diatom free Al plate at room temperature by accumulating 100 scans with 4cm^{-1} resolution in the 4000-700cm^{-1} wavenumber range. The sample transflection spectrum was measured on a diatom sample on an Al plate at room temperature. Then the diatom sample

on the Al plate in the heating stage was heated at a rate of 50^{o}C/minute up to the desired temperature (260, 270, 280, 290 or 300°C), which was kept constant during the following IR spectral measurements. A series of IR transflection (transmission-reflection) spectra was measured on the same position of the diatom sample on the Al plate at every 100 seconds. These transflection signals were divided by the above background spectrum on the diatom-free Al plate at room temperature. Although the background spectrum on the Al plate at the same temperature is preferable, since the reflection spectra of the Al plate at different temperatures did not vary significantly without any absorption features, the background reflection spectrum at room temperature on the Al plate was used for the whole series of data.

The transflection method of microscopic samples on metal plates is a useful method for in-situ heating behavior of geochemical samples (Okumura and Nakashima, 2004; 2005; 2006, Kebukawa et al., 2010, Tonoue et al., 2014). However, this method might include some artifacts (Tonoue et al., 2014). For instance, 1200-1000 cm^{-1} bands (Si-O stretching) are severely distorted because of reflection at the very absorbing wavenumber in transflection spectra of diatoms. However, the higher wavenumber regions such as aliphatic CHs and amides are less affected by strong reflections. Moreover, in order to avoid the void effect (Chapter 2), 100×100μm^2 aperture area was set within the diatom sample.

Diatom IR spectra were collected as absorbance (Abs), which can be written by the Lambert-Beer law as:

$$\mathrm{Abs} = -\log_{10}\left[\frac{I_1}{I_0}\right]$$

where I_0 is the intensity of the incident beam (background spectrum), and I_1 is the infrared signal intensity of the sample. In the transflection signal of a diatom sample, IR light transmitted through the diatom is reflected at the Al plate and transmitted again through the diatom, so the IR lights are travelling about twice the thickness of the diatom sample.

3.4 Results

3.4.1 IR spectra of unwashed diatom silica frustule

A representative Infrared (IR) transflection spectrum of an unwashed diatom silica frustule at room temperature (26°C) is shown in Fig.3.2. All the absorption bands in transflection mode in the 4000 - 700cm^{-1} wavenumber region are similar to those of transmission mode (Chapter 2) with the exception of Si-O stretching bands (1240 and 1030cm^{-1} bands due to stretching of SiO-H and Si-OH bonds, respectively) which are distorted at around 1300 – 1000cm^{-1} wavenumber region.

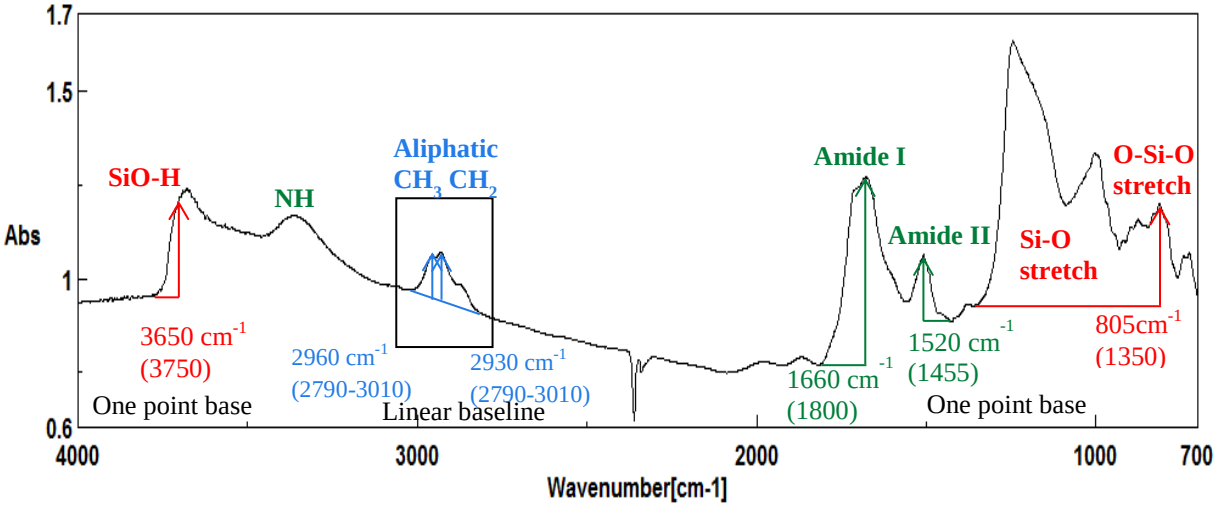

Fig. 3.2. A representative IR Spectrum of an unwashed diatom silica frustule at room temperature (26°C).

In general, absorption bands are observed at 3650, 3380, 2960, 2930, 1660, 1520 and 805cm^{-1}. The 3650cm^{-1} band is due to stretching of O-H bound to Si and the 805cm^{-1} band is attributed to symmetric Si-O stretching vibration (Chapter 2). The 2960 and 2930cm^{-1} bands are aliphatic CH_3 and aliphatic CH_2 asymmetric stretching, respectively (Painter et al., 1981; Coates, 2000; Gelabert et al., 2004; Kebukawa et al., 2009). The 1660 and 1520cm^{-1} bands are due to C=O stretching (Amide I) and N-H bending (Amide II) in amides of proteins, respectively (Painter et al., 1981; Coates, 2000; Gelabert et al., 2004;

Kebukawa et al., 2009; Jungandreas et al., 2012). In order to determine the following IR spectral changes upon heating of unwashed diatom frustules, peak heights of these bands have been determined as indicated in Fig.3.2. In this chapter, the peak heights for aliphatic CHs at 2960 and 2930cm^{-1} were determined by the linear baseline between 2790 and 3010cm^{-1}.

3.4.2 Changes in aliphatic CHs of diatom frustules during isothermal heating experiments

Isothermal heating in situ IR-microspectroscopy has been applied to diatom samples to collect a time series data sets at different temperatures (260, 270, 280, 290 and 300°C). Representative IR spectral changes with time during heating experiments of diatoms on Al plates under ambient atmospheric condition at 300, 290, 280, 270 and 260ºC are shown in Figs. 3.3-3.7.

Although the trends of peak changes are similar at all temperatures but on different time scales, peak heights of aliphatic CHs (2960 and 2930cm^{-1}), amide I (1660cm^{-1}), amide II (1520cm^{-1}) and SiOH (3650cm^{-1}) decreased with time. These results indicate decrease of both organic functional groups and SiOH upon heating. On the other hand, SiOSi band around 805cm^{-1} increases with heating due possibly to silica transformation. The amide and silica changes will be discussed in chapters 4 and 5, respectively.

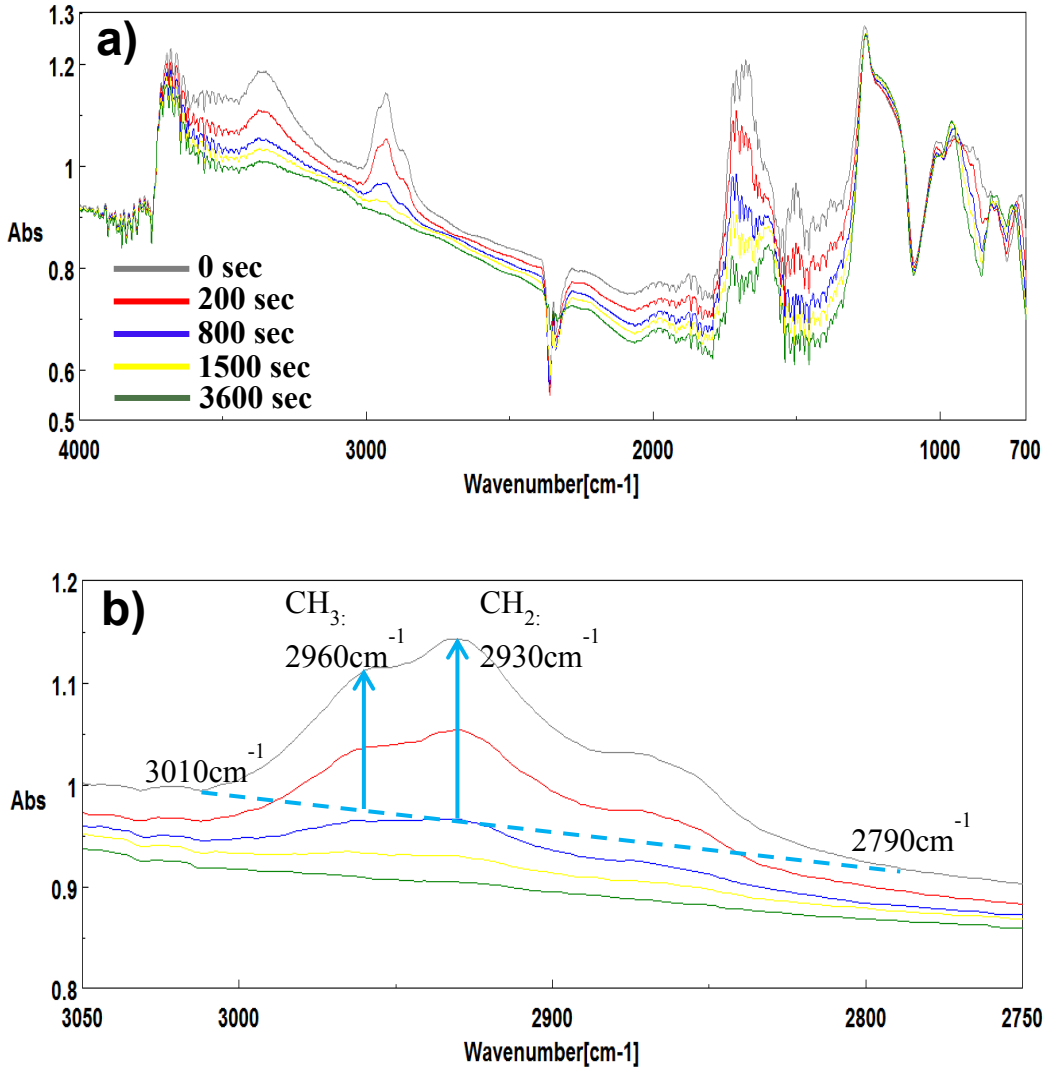

Fig.3.3. (a) IR spectral changes of diatom at 0, 200, 800, 1500 and 3600 seconds during heating experiments of an unwashed diatom on Al foil under ambient atmosphere at 300ºC. (b) Details of the aliphatic CH region with the linear baseline of 2790cm^{-1} to 3010cm^{-1} shown on the 0 sec spectra.

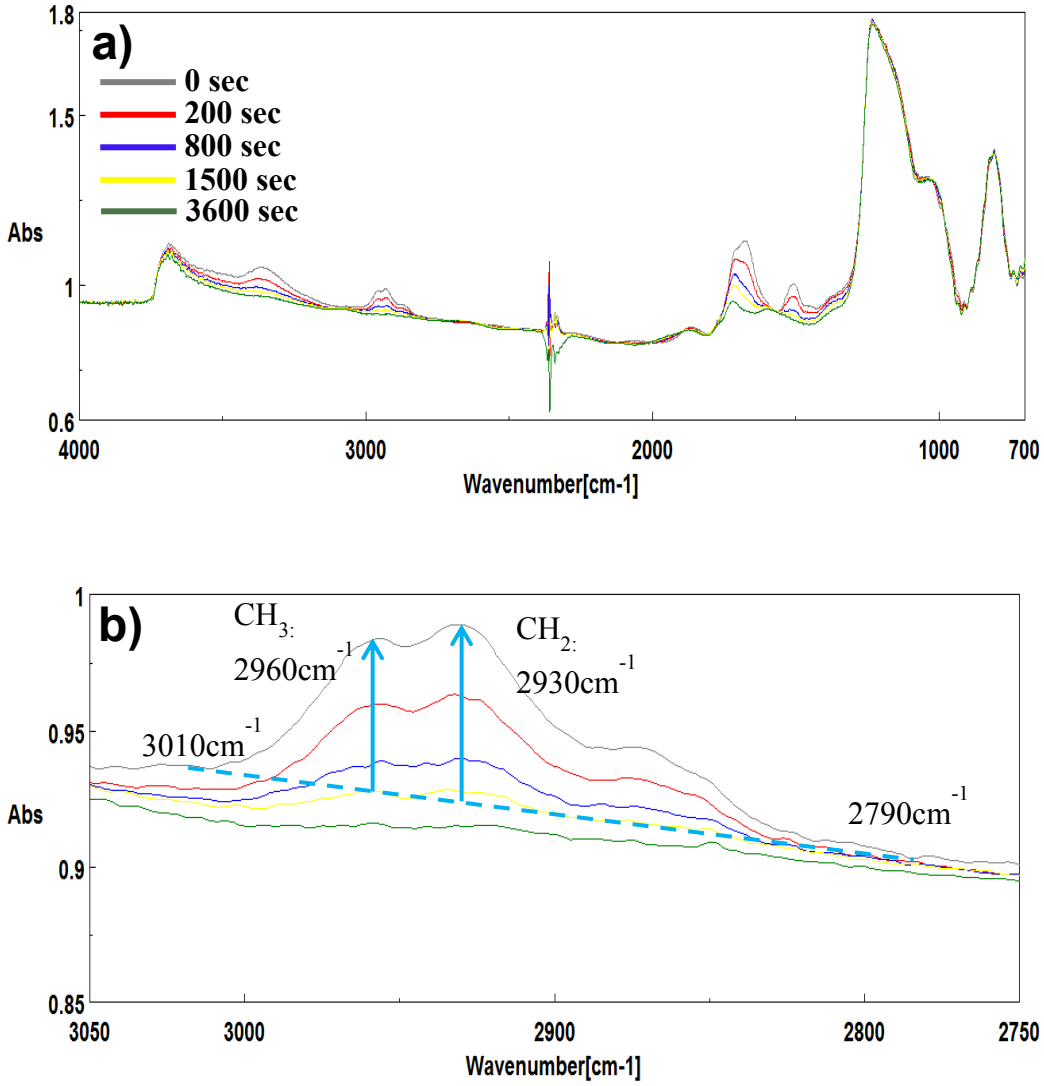

Fig.3.4. (a) IR spectral changes of diatom at 0, 200, 800, 1500 and 3600 seconds during heating experiments of diatom on Al foil under ambient atmospheric condition at 290ºC. (b) Details of the aliphatic CHs area with the linear baseline of 2790cm^{-1} to 3010cm^{-1} shown on the 0sec spectra.

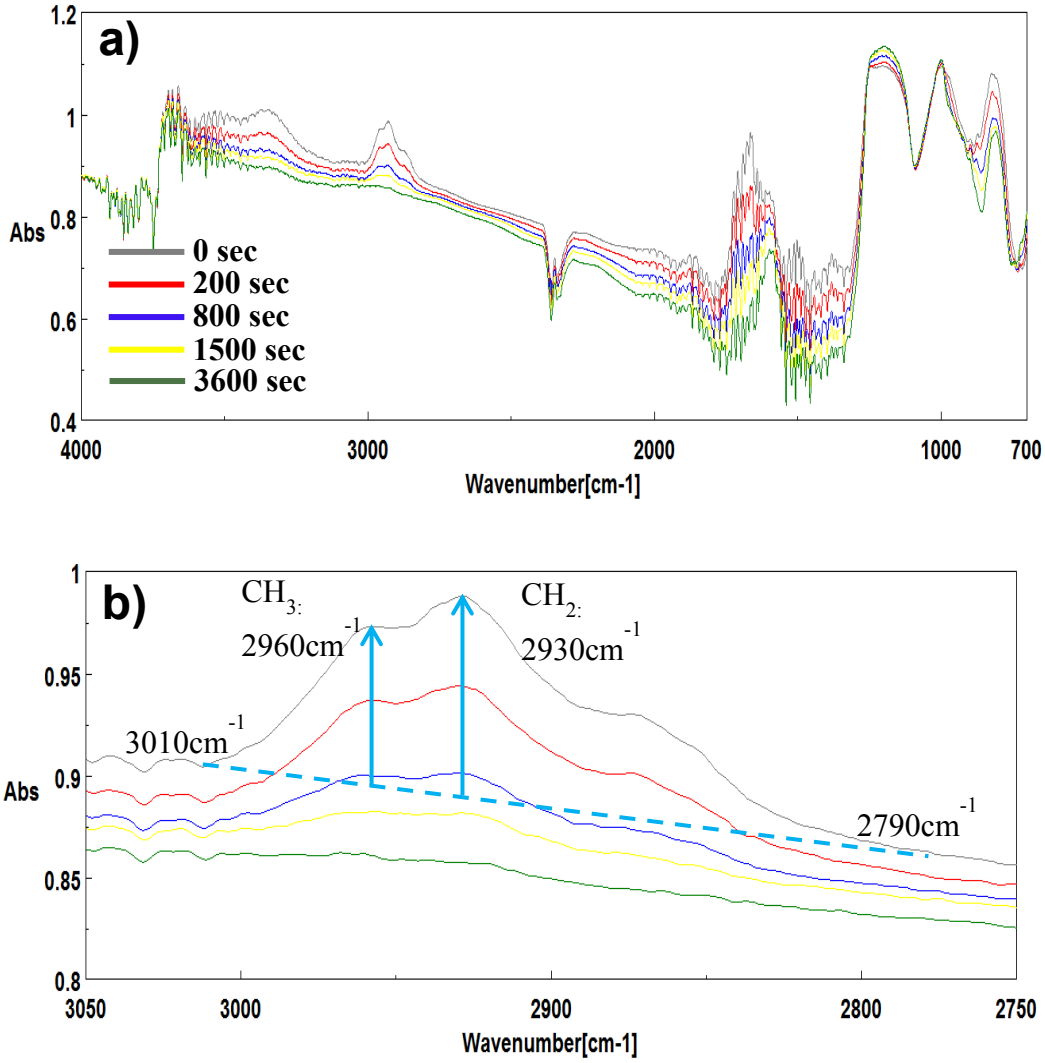

Fig.3.5. (a) IR spectral changes of diatom at 0, 200, 800, 1500 and 3600 seconds during heating experiments of diatom on Al foil under ambient atmospheric condition at 280ºC. (b) Details of the aliphatic CHs area with the linear baseline of 2790cm^{-1} to 3010cm^{-1} shown on the 0sec spectra.

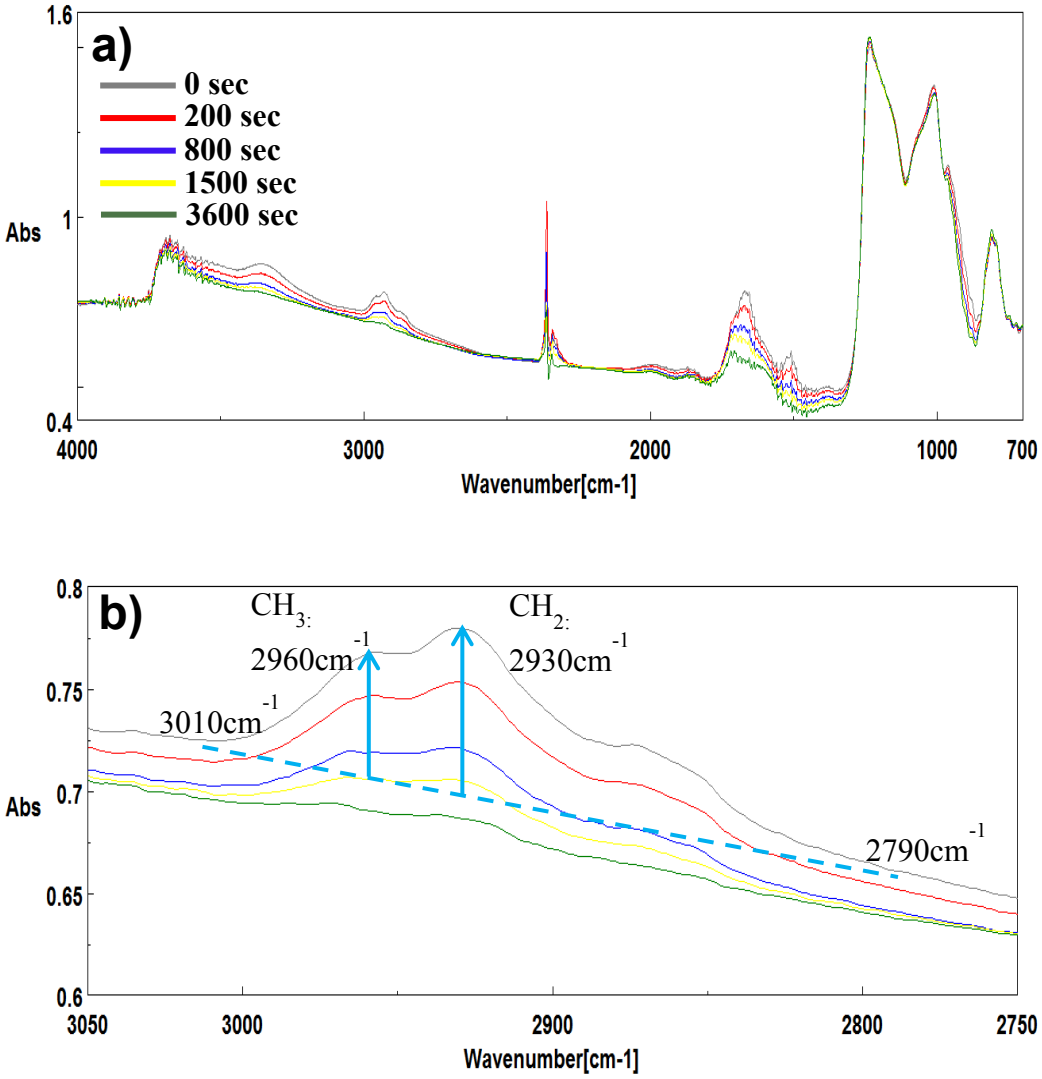

Fig.3.6. (a) IR spectral changes of diatom at 0, 200, 800, 1500 and 3600 seconds during heating experiments of diatom on Al foil under ambient atmospheric condition at 270ºC. (b) Details of the aliphatic CHs area with the linear baseline of 2790cm^{-1} to 3010cm^{-1} shown on the 0sec spectra.

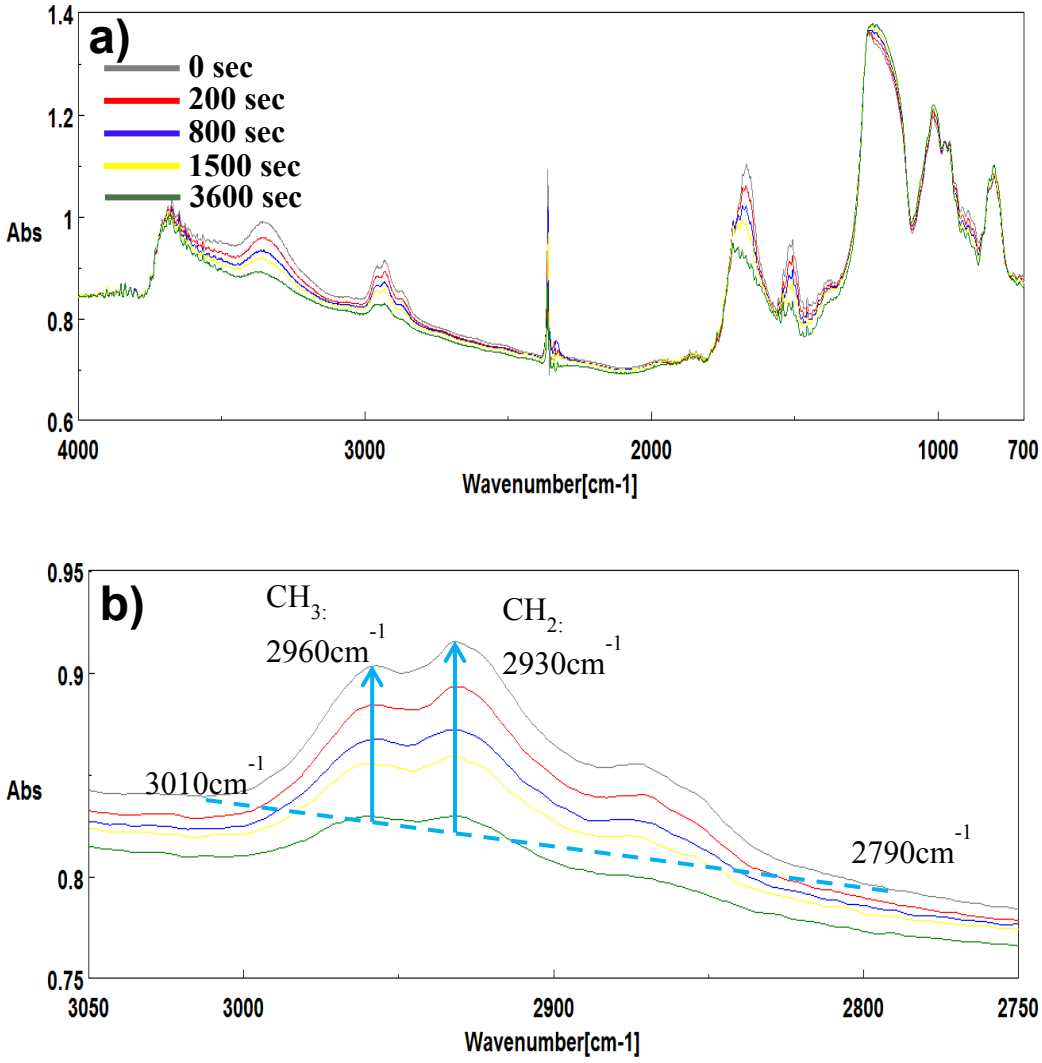

Fig.3.7. (a) IR spectral changes of diatom at 0, 200, 800, 1500 and 3600 seconds during heating experiments of diatom on Al foil under ambient atmospheric condition at 260ºC. (b) Details of the aliphatic CHs area with the linear baseline of 2790cm^{-1} to 3010cm^{-1} shown on the 0sec spectra.

In order to quantitatively examine decrease trends of aliphatic CH_2 (2930cm^{-1}) and CH_3 (2960cm^{-1}) bands, a linear baseline between 2790 and 3010cm^{-1} was applied to determine their peak heights. Changes with time in the peak heights of aliphatic CH_2 at 2930cm^{-1} and CH_3 at 2960cm^{-1} at 260 to 300ºC are shown in Fig. 3.8. The peak heights are divided by those at time zero (starting of the isothermal heating). The decrease trends of aliphatic CHs are similar for all the temperatures. The decrease rates appear to be faster at higher temperatures.

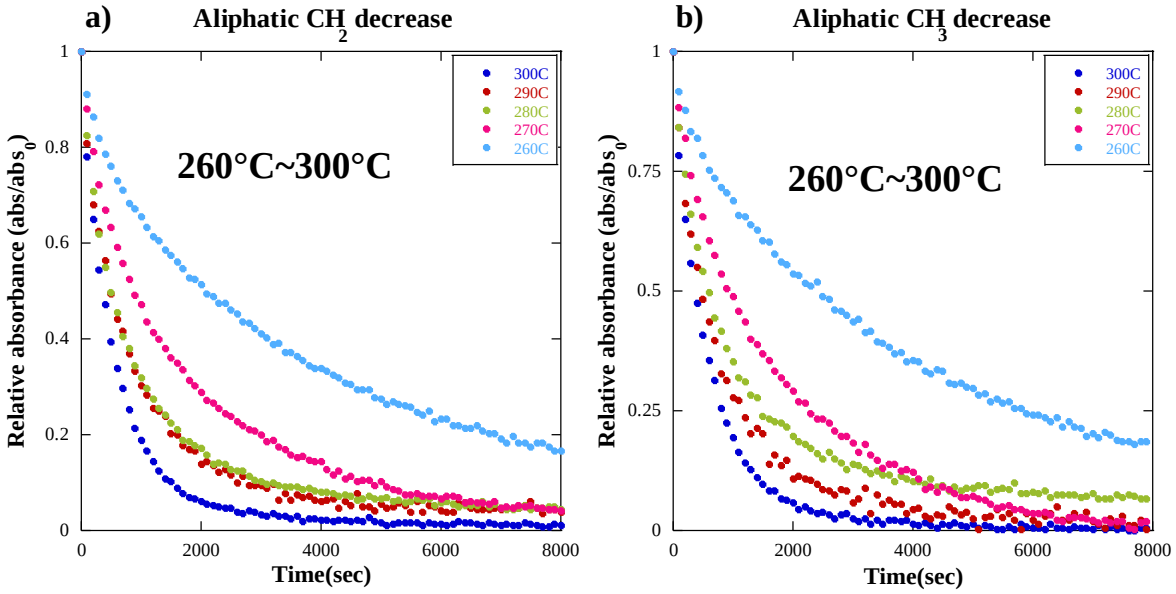

Fig.3.8. Changes with time in the peak heights of aliphatic CHs for (a) CH_2 at 2930cm^{-1} and (b) CH_3 at 2960cm^{-1} at 260, 270, 280, 290 and 300ºC.

3.5 Discussion

3.5.1 Kinetic analyses of decreases of aliphatic CHs

The above experimental results were analyzed by chemical reaction kinetics to determine reaction rates of aliphatic CH decrease in diatoms.

The degradation of organic functional groups is supposed to be a mixture of diverse complex multiple reactions, and separations of those reactions are often difficult. In the analyses of burial and diagenesis of organic materials in sediments and sedimentary rocks, the first order kinetics is often used for determining essentially oxidation rates of organic materials originated from dead organisms (Berner, 1980). In petroleum aliphatic hydrocarbon forming reactions, a number of parallel first order reactions are supposed and the summation of the multiple first order reactions has been employed for kinetic treatments (Behar et al., 1997; Burnham and Braun, 1990; Dieckmann et al., 2000). Therefore, the present decrease trends of aliphatic CHs in Fig.3.8 can be fitted by a combination of several first order reactions.

First, only one first order reaction model was applied to fit the experimental data by a single exponential curve. However, the fitting was very poor indicating presence of more than one first order reactions. In fact, by plotting the experimental data in Fig.3.8 in semi-logarithmic diagrams, roughly two linear regions can be recognized at initial and later stages of experiments at any temperature, especially at higher temperatures (Fig. 3.9). These two linear trends can correspond to two independent first order reactions (exponential decays): one is faster while the other one is slower.

By assuming the two first order reaction model, the decrease trends for CH_2 and CH_3 have been fitted by the following two exponential fitting equation for each temperature, to obtain reaction rate constants k_1 and k_2:

$$Abs = C_1 \exp(-k_1 t) + C_2 \exp(-k_2 t) + C_3$$

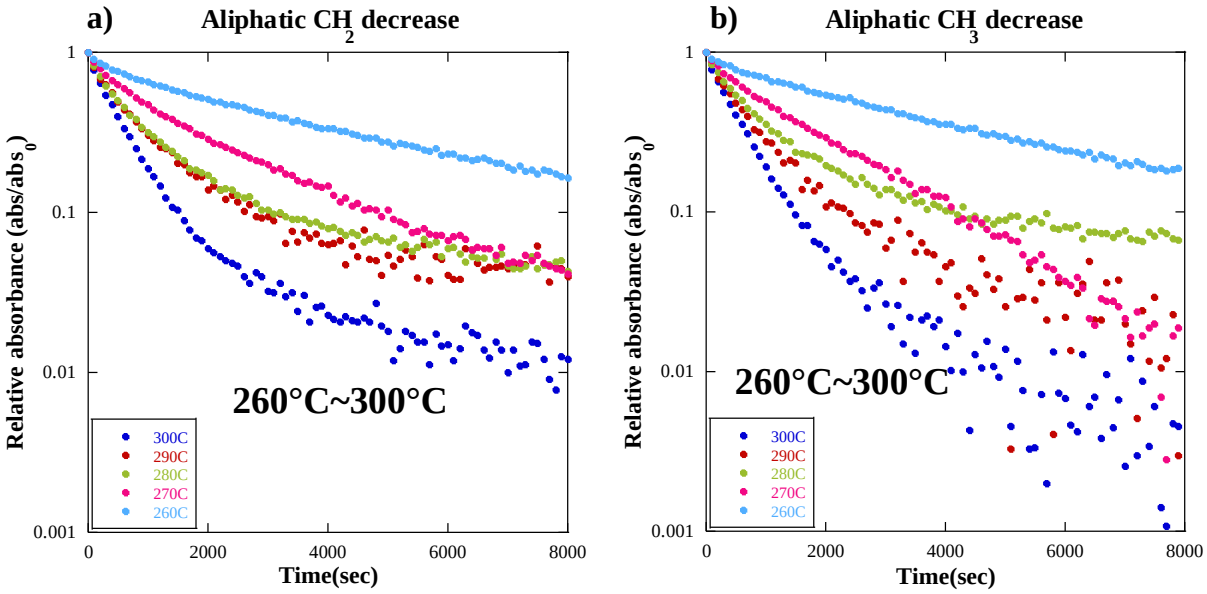

Fig.3.9, Semi-logarithmic plots for changes with time in the peak heights of aliphatic CHs for (a) CH_2 at 2930cm^{-1} and (b) CH_3 at 2960cm^{-1} at 260, 270, 280, 290 and 300ºC.

3.5.2 Decrease rates of aliphatic CHs

The fittings by the above two first order reaction equation of the experimental data for aliphatic CH decreases at 300^{o}C are shown in Fig.3.10. The fittings are very well with correlation coefficient R of over 0.9999, suggesting the validity of the reaction model.

Obtained first order rate constants for aliphatic CH_2 at 300ºC are k_1 = 1.3 x 10^{-2} s^{-1} for the initial stage (fast) and k_2 = 1.6 x 10^{-3} s^{-1} for the later stage (slow) (Fig.3.10a). The first order rate constants for aliphatic CH_3 at 300ºC are obtained to be k_1 = 1.7 x 10^{-2} s^{-1} for the initial stage (fast) and k_2 = 1.6 x 10^{-3} s^{-1} for the later stage (slow) (Fig.3.10b). These two rate constants are roughly in the same orders for the faster and slower reactions of aliphatic CH_2 and CH_3 (Table 3.1).

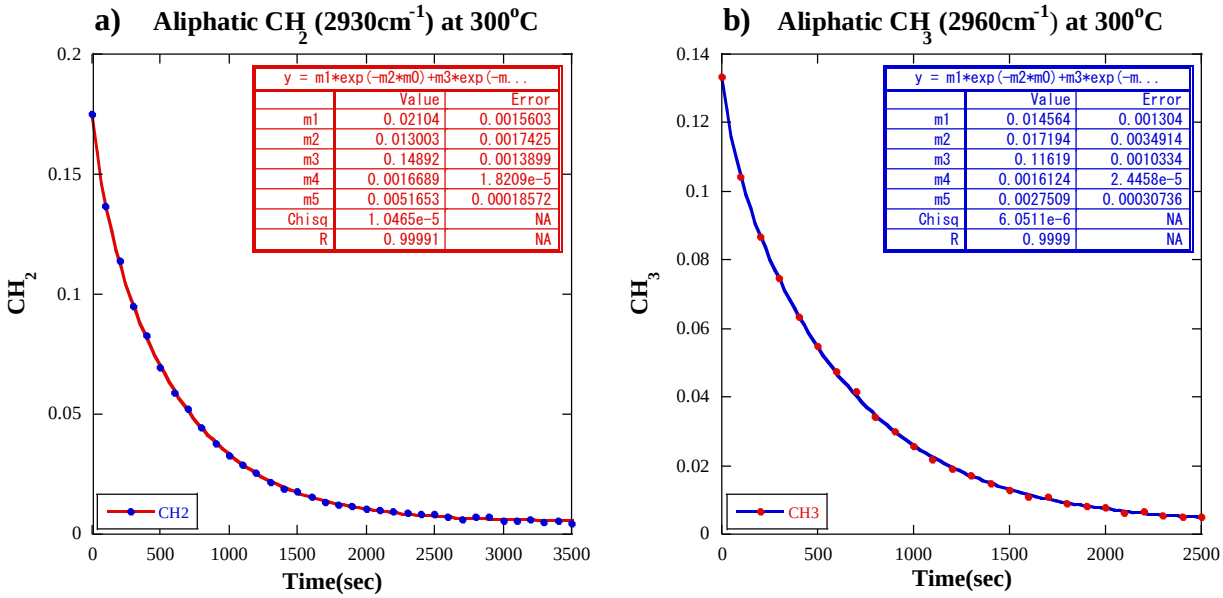

Fig.3.10. Results of curve fitting by two first order reactions (Abs = $C_1\exp(-k_1t) + C_2\exp(-k_2t) + C_3$), for changes with time in the peak heights of aliphatic CHs for (a) CH_2 at 2930cm^{-1} and (b) CH_3 at 2960cm^{-1} at 300ºC.

	CH_2: 2930 cm^{-1} Initial fast: k_1	CH_2: 2930 cm^{-1} Later slow: k_2	CH_3: 2960 cm^{-1} Initial fast: k_1	CH_3: 2960 cm^{-1} Later slow: k_2
300ºC	1.3×10^{-2} s^{-1}	1.6×10^{-3} s^{-1}	1.7×10^{-2} s^{-1}	1.6×10^{-3} s^{-1}
290ºC	8.1×10^{-3} s^{-1}	1.1×10^{-3} s^{-1}	5.9×10^{-3} s^{-1}	1.1×10^{-3} s^{-1}
280ºC	3.6×10^{-3} s^{-1}	7.7×10^{-4} s^{-1}	2.4×10^{-3} s^{-1}	6.3×10^{-4} s^{-1}
270ºC	2.9×10^{-3} s^{-1}	4.6×10^{-4} s^{-1}	1.5×10^{-3} s^{-1}	3.4×10^{-4} s^{-1}
260ºC	1.4×10^{-3} s^{-1}	2.0×10^{-4} s^{-1}	1.9×10^{-3} s^{-1}	2.1×10^{-4} s^{-1}

Table 3.1. Summary of the first order rate constants for aliphatic CH_2 and CH_3 (initial fast: k_1, later slow: k_2) at temperatures of 300-260ºC.

The fittings by the above two first order reaction equation of the experimental data for aliphatic CH decreases at 290^{o}C are shown in Fig.3.11. The fittings are very well with correlation coefficient R of 0.9993 and 0.9986, suggesting the validity of the reaction model. Obtained first order rate constants for aliphatic CH_2 at 290ºC are $k_1 = 8.1 \times 10^{-3}$ s^{-1}, for the initial stage (fast) and $k_2 = 1.1 \times 10^{-3}$ s^{-1} for the later stage (slow) (Fig.3.11a). The first order rate constants for aliphatic CH_3 at 290ºC are obtained to be $k_1 = 5.9 \times 10^{-3}$ s^{-1} for the initial stage (fast) and $k_2 = 1.1 \times 10^{-3}$ s^{-1} for the later stage (slow) (Fig.3.11b). These two rate constants are roughly in the same orders for the faster and slower reactions of aliphatic CH_2 and CH_3 (Table 3.1).

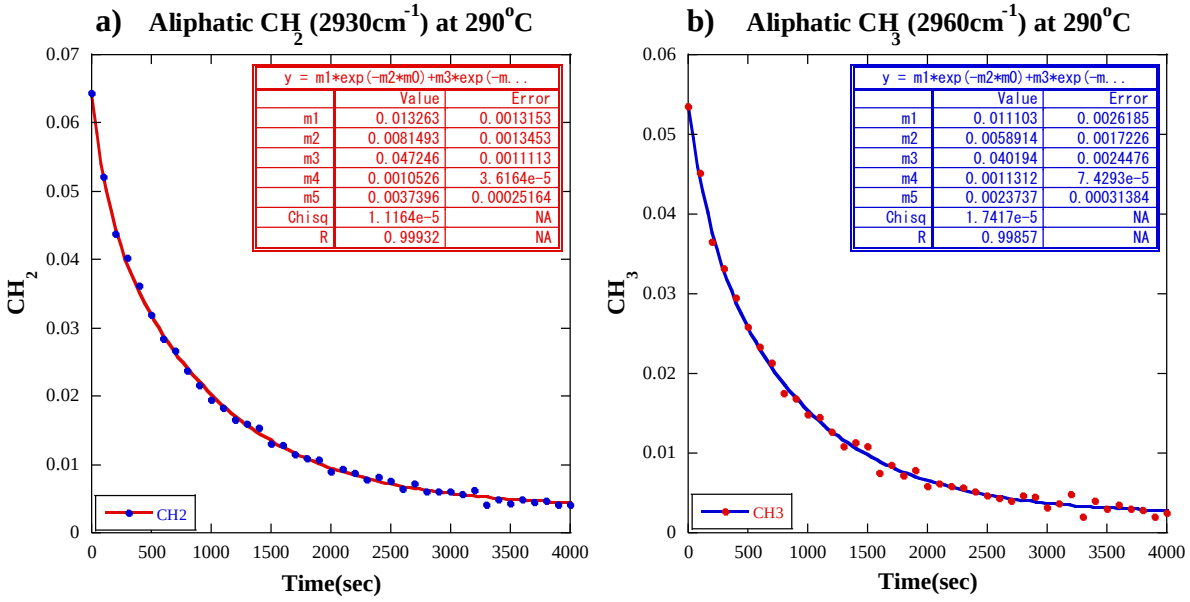

Fig.3.11. Results of curve fitting by two first order reactions (Abs = $C_1exp(-k_1t) + C_2exp(-k_2t) + C_3$), for changes with time in the peak heights of aliphatic CHs for (a) CH_2 at 2930cm^{-1} and (b) CH_3 at 2960cm^{-1} at 290ºC.

The fittings by the above two first order reaction equation of the experimental data for aliphatic CH decreases at 280°C are shown in Fig.3.12. The fittings are very well with correlation coefficient R of 0.9996 and 0.9994, suggesting the validity of the reaction model. Obtained first order rate constants for aliphatic CH_2 at 280ºC are k_1 = 3.6 x10^{-3} s^{-1}, for the initial stage (fast) and k_2 = 7.7 x10^{-4} s^{-1} for the later stage (slow) (Fig.3.12a). The first order rate constants for aliphatic CH_3 at 280ºC are obtained to be k_1 = 2.4 x10^{-3} s^{-1} for the initial stage (fast) and k_2 = 6.3 x10^{-4} s^{-1} for the later stage (slow) (Fig.3.12b). These two rate constants are roughly in the same orders for the faster and slower reactions of aliphatic CH_2 and CH_3 (Table 3.1).

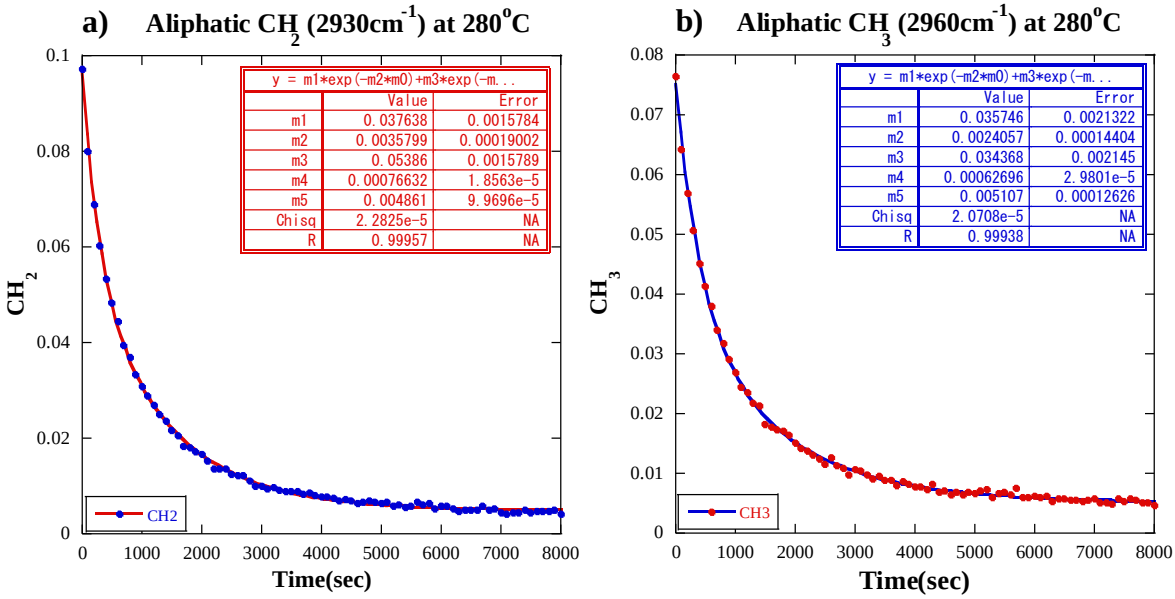

Fig.3.12. Results of curve fitting by two first order reactions (Abs = $C_1\exp(-k_1t) + C_2\exp(-k_2t) + C_3$), for changes with time in the peak heights of aliphatic CHs for (a) CH_2 at 2930cm^{-1} and (b) CH_3 at 2960cm^{-1} at 280ºC.

The fittings by the above two first order reaction equation of the experimental data for aliphatic CH decreases at 270°C are shown in Fig.3.13. The fittings are very well with correlation coefficient R of 0.9997 and 0.9991, suggesting the validity of the reaction model. Obtained first order rate constants for aliphatic CH_2 at 270ºC are k_1 = 2.9 x10^{-3} s^{-1}, for the initial stage (fast) and k_2 = 4.6 x10^{-4} s^{-1} for the later stage (slow) (Fig.3.13a). The first order rate constants for aliphatic CH_3 at 270ºC are obtained to be k_1 = 1.5 x10^{-3} s^{-1} for the initial stage (fast) and k_2 = 3.4 x10^{-4} s^{-1} for the later stage (slow) (Fig.3.13b). These two rate constants are roughly in the same orders for the faster and slower reactions of aliphatic CH_2 and CH_3 (Table 3.1).

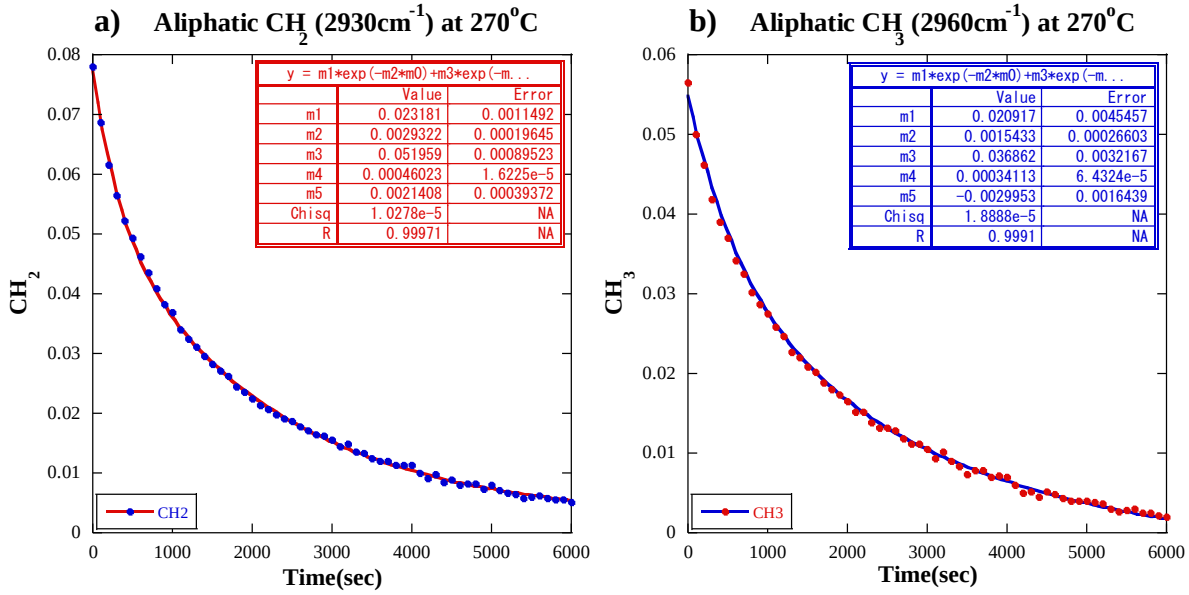

Fig.3.13. Results of curve fitting by two first order reactions (Abs = $C_1 exp(-k_1 t) + C_2 exp(-k_2 t) + C_3$), for changes with time in the peak heights of aliphatic CHs for (a) CH_2 at 2930cm^{-1} and (b) CH_3 at 2960cm^{-1} at 270ºC.

The fittings by the above two first order reaction equation of the experimental data for aliphatic CH decreases at 260°C are shown in Fig.3.14. The fittings are very well with correlation coefficient R of 0.9994, suggesting the validity of the reaction model. Obtained first order rate constants for aliphatic CH_2 at 260ºC are k_1 = 1.4 x10^{-3} s^{-1}, for the initial stage (fast) and k_2 = 2.0 x10^{-4} s^{-1} for the later stage (slow) (Fig.3.14a). The first order rate constants for aliphatic CH_3 at 260ºC are obtained to be k_1 = 1.9 x10^{-3} s^{-1} for the initial stage (fast) and k_2 = 2.1 x10^{-4} s^{-1} for the later stage (slow) (Fig.3.14b). These two rate constants are roughly in the same orders for the faster and slower reactions of aliphatic CH_2 and CH_3 (Table 3.1).

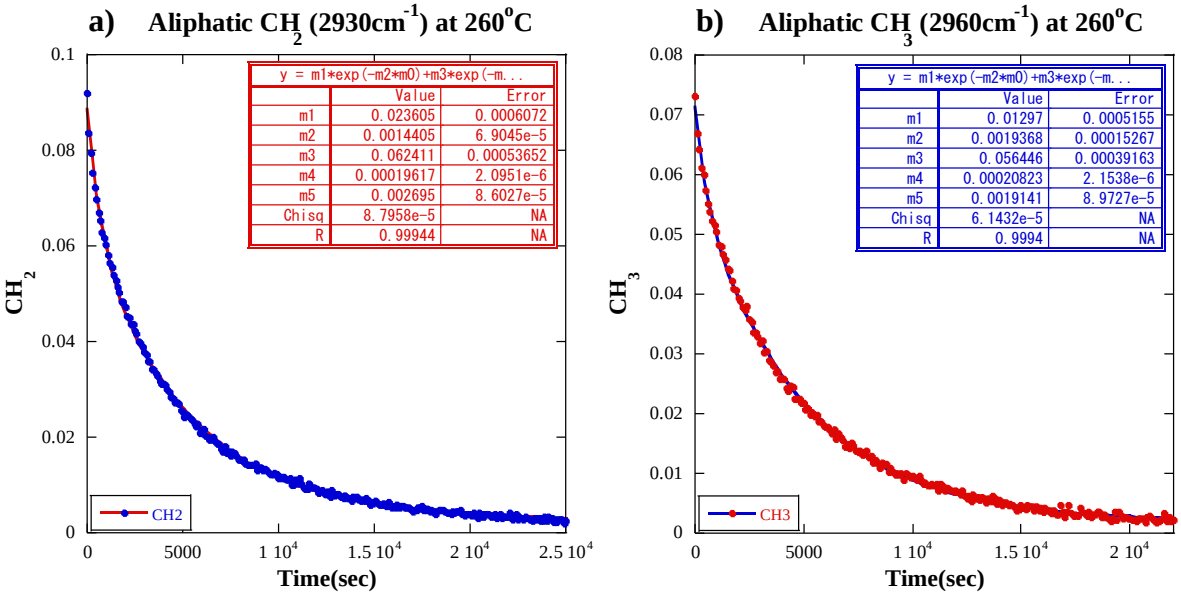

Fig.3.14. Results of curve fitting by two first order reactions (Abs = $C_1\exp(-k_1t) + C_2\exp(-k_2t) + C_3$), for changes with time in the peak heights of aliphatic CHs for (a) CH_2 at 2930cm^{-1} and (b) CH_3 at 2960cm^{-1} at 260ºC.

3.5.3. Temperature dependence of decrease rates of aliphatic CHs

Temperature dependence of reaction rates can be described by the Arrhenius equation:

$$\ln(k)=\ln(A)-E_a/RT$$

where k is the rate constant, A is the pre-exponential "frequency" factor, E_a is the activation energy, R is the gas constant (R= 8.314 J/mol.K) and T is the absolute temperature (K).

Obtained first order rate constants at different temperatures for aliphatic CH_2 and CH_3, k_1 for the initial stage (fast) and k_2 for the later stage (slow), were plotted in Arrhenius diagrams in Fig.3.15a and Fig.3.15b, respectively.

The rate constant of k_1 for aliphatic CH_3 is larger than that for CH_2 at 300°C, but they are smaller than those for CH_2 at the temperatures of 290, 280, 270 and 260°C. Gradients of

fitted lines of these data in Fig.3.15a give activation energies of E_a~123 kJ/mol for k_1 of CH_2 and E_a~156 kJ/mol for k_1 of CH_3 at the temperature range from 300 to 260°C.

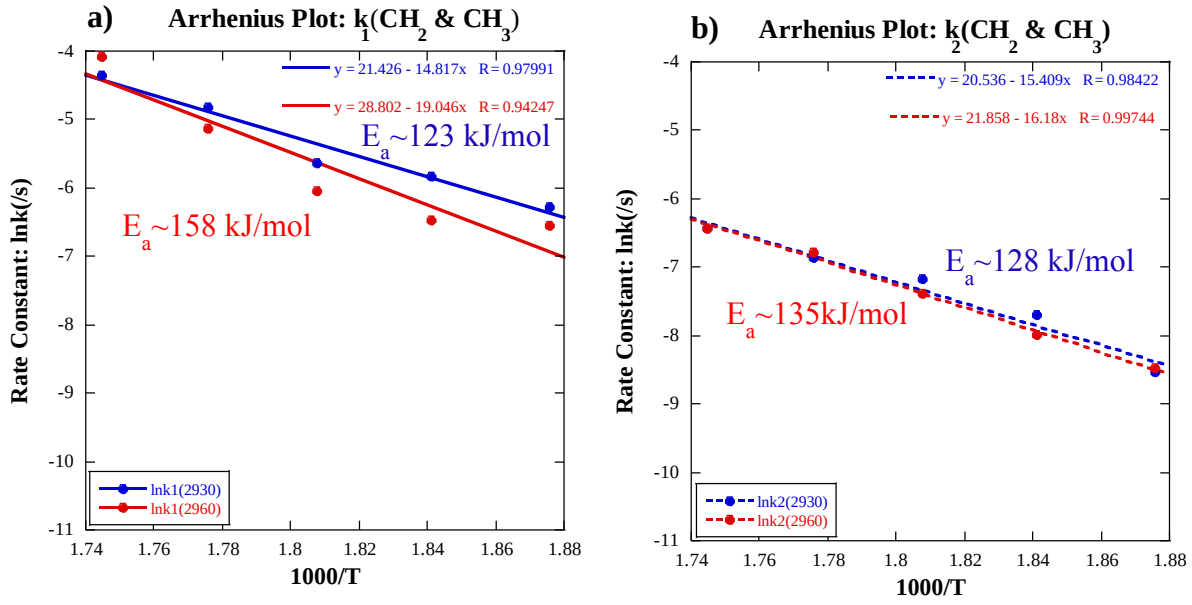

Fig.3.15. Arrhenius diagrams for the rate constants k as a function of temperature T (K) determined by two first order reactions for diatom heating experiments in Figs. 3.10 to 3.14. (a) k_1 for CH_2 at 2930cm^{-1} and CH_3 at 2960cm^{-1} at the temperature range of 300-260ºC. (b) k_2 for CH_2 at 2930cm^{-1} and CH_3 at 2960cm^{-1} at the temperature range of 300-260ºC.

The rate constants of k_2 for aliphatic CH_3 are larger than those for CH_2 at 300, 290 and 260°C, but they are smaller than those of CH_2 at 280 and 270°C. Gradients of fitted lines of these data in Fig.3.15b give activation energies of E_a~128 kJ/mol for k_2 of CH_2 and E_a~135kJ/mol for k_2 of CH_3 at the temperature range from 300 to 260°C.

The rate constants of the faster process k_1 of aliphatic CH_2 and CH_3 decreases plotted in the Arrhenius diagram (Fig. 3.15a) showed larger gradients for higher temperatures and smaller gradients for lower temperatures. Therefore, these data can be fitted by two

different linear trends for different temperature regions of 300 to 280^{o}C and 280 to 260^{o}C (Fig .3.16). These fitted lines for k_1 in the 300-280^{o}C range give activation energies of E_a~170 kJ/mol for CH_2 and E_a~257 kJ/mol for CH_3 (Fig.3.16a). On the other hand, for the temperature region 280^{-}-260^{o}C much lower activation energies of E_a~77 kJ/mol for CH_2 and E_a~62kJ/mol for CH_3 are obtained (Fig.3.16b).

The fitted lines for k_2 in the 300-280^{o}C range give activation energies of E_a~97 kJ/mol for CH_2 and E_a~124 kJ/mol for CH_3 (Fig.3.16c). For the temperature region from 280^{o}C to 260^{o}C, activation energies are E_a~167 kJ/mol for CH_2 and E_a~134 kJ/mol for CH_3 (Fig.3.16d).

These reaction rate constants and activation energies will be discussed in the summary and general discussion (chapter 6).

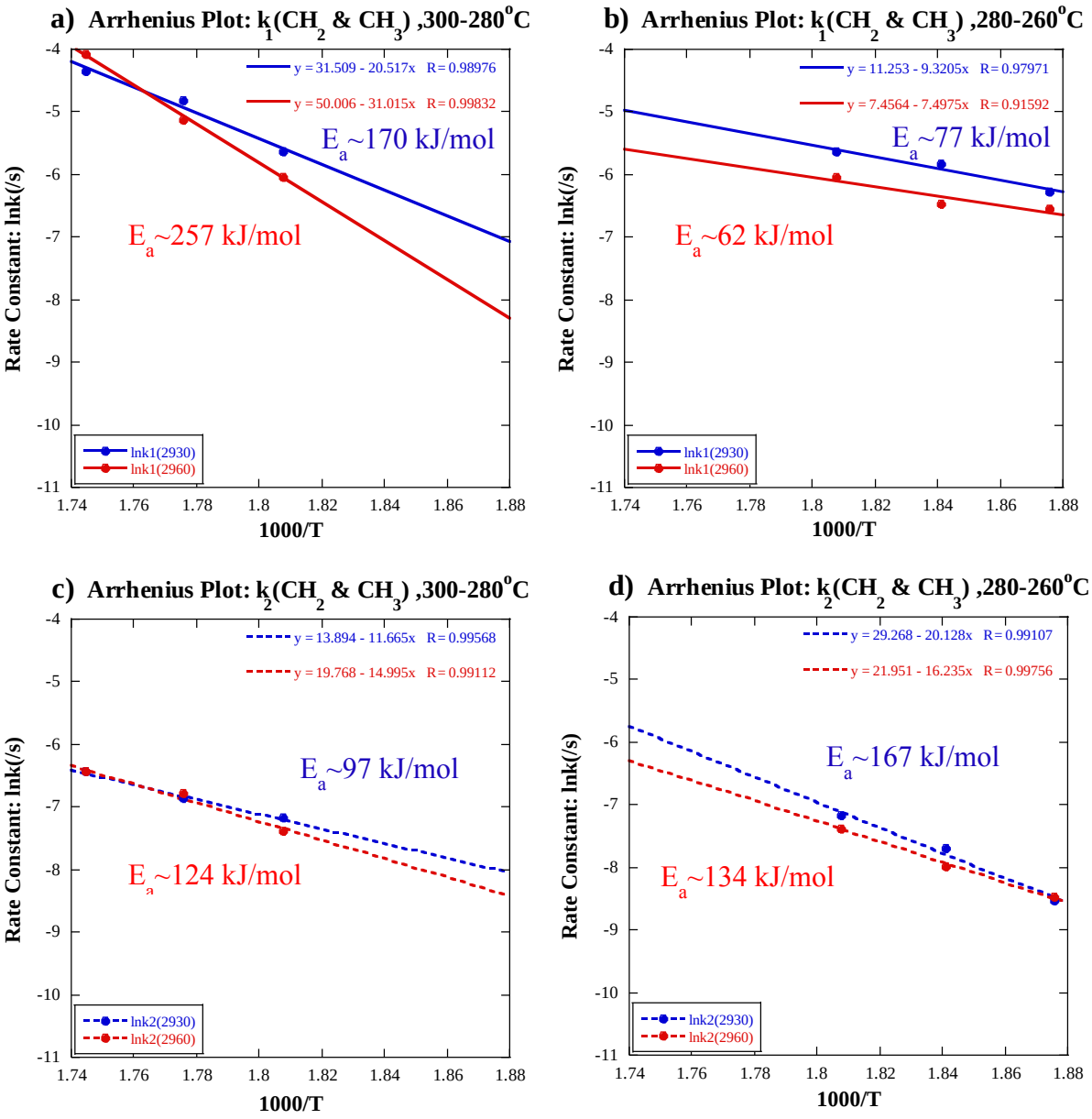

Fig.3.16. Arrhenius diagrams for the rate constants k as a function of temperature T (K) determined by two first order reactions for diatom heating experiments.

(a) k_1 of CH_2 at 2930cm^{-1} and CH_3 at 2960cm^{-1} in the temperature range of 300-280ºC.

(b) k_1 of CH_2 at 2930cm^{-1} and CH_3 at 2960m^{-1} in the temperature range of 280-260ºC.

(c) k_2 of CH_2 at 2930cm^{-1} and CH_3 at 2960cm^{-1} in the temperature range of 300-280ºC.

(d) k_2 of CH_2 at 2930cm^{-1} and CH_3 at 2960cm^{-1} in the temperature range of 280-260ºC.

Chapter 4. Changes in amide I and amide II during in-situ heating IR microspectroscopy of unwashed diatoms

4.1. Introduction

As it stated in the introduction of chapter 3, dead bodies of marine diatoms are sedimented on the ocean floor and buried in marine sediments with time. During their burial, temperature and pressure increase and organic components in diatom bodies are transformed. Although generation of hydrocarbons from diatoms is considered to be related to transformation of organic components during the burial-diagenesis (Tissot and Welt, 1984), detailed relations of aliphatic hydrocarbon release and protein degradation are not known.

In this chapter, protein degradation processes are studied during the same in situ heating IR transflection microspectroscopy on diatom frustules as chapter 3 and kinetic parameters (reaction rate constants and activation energies) for proteins (amide I and amide II bands) have been evaluated.

4.2. Methods

4.2.1. In situ isothermal heating experiments by micro-FTIR spectroscopy

The same unwashed centric diatoms (*Arachnoidiscus ornatus,* diameters: 100-350 μm) were mounted on Al plates without using any adhesive for measuring IR spectral changes at high temperatures in the heating stage (Linkam TS-1500) under the IR microspectromter (FTIR-620+IRT30, JASCO Co., Ltd). The temperature of the sample was monitored just below the Al plate and increased at a rate of 50^{o}C/minute up to the desired temperature (260, 270, 280, 290 or 300°C). Since no window materials are set in the heating stage, the diatom sample was heated in an ambient air atmosphere.

A background reflection spectrum on a 100×100μm^2 aperture area was first measured on a diatom free Al plate at room temperature by accumulating 100 scans with 4cm^{-1} resolution in the 4000-700cm^{-1} wavenumber range. The sample transflection spectrum was measured on a diatom sample on an Al plate at room temperature. Then the diatom sample on the Al plate in the heating stage was heated at a rate of 50^{o}C/minute up to the desired temperature (260, 270, 280, 290 or 300°C), which was kept constant during the following IR spectral measurements. A series of IR transflection (transmission-reflection) spectra was measured on the same position of the diatom sample on the Al plate at every 100 seconds. These transflection signals were divided by the above background spectrum on the diatom-free Al plate at room temperature.

4.3. Results

4.3.1. Changes in amide I and amide II of diatom frustules during isothermal heating experiments

Isothermal heating in situ IR-microspectroscopy has been applied to diatom samples to collect a time series data sets at different temperatures (260, 270, 280, 290 and 300°C). Representative IR spectral changes with time during heating experiments of diatom frustules on Al foils under ambient atmospheric condition at 300, 290, 280, 270 and 260ºC are shown in Figs. 4.1-4.5. In this chapter, since changes in amide I and II bands of proteins are analyzed details of these bands are also shown in these figures.

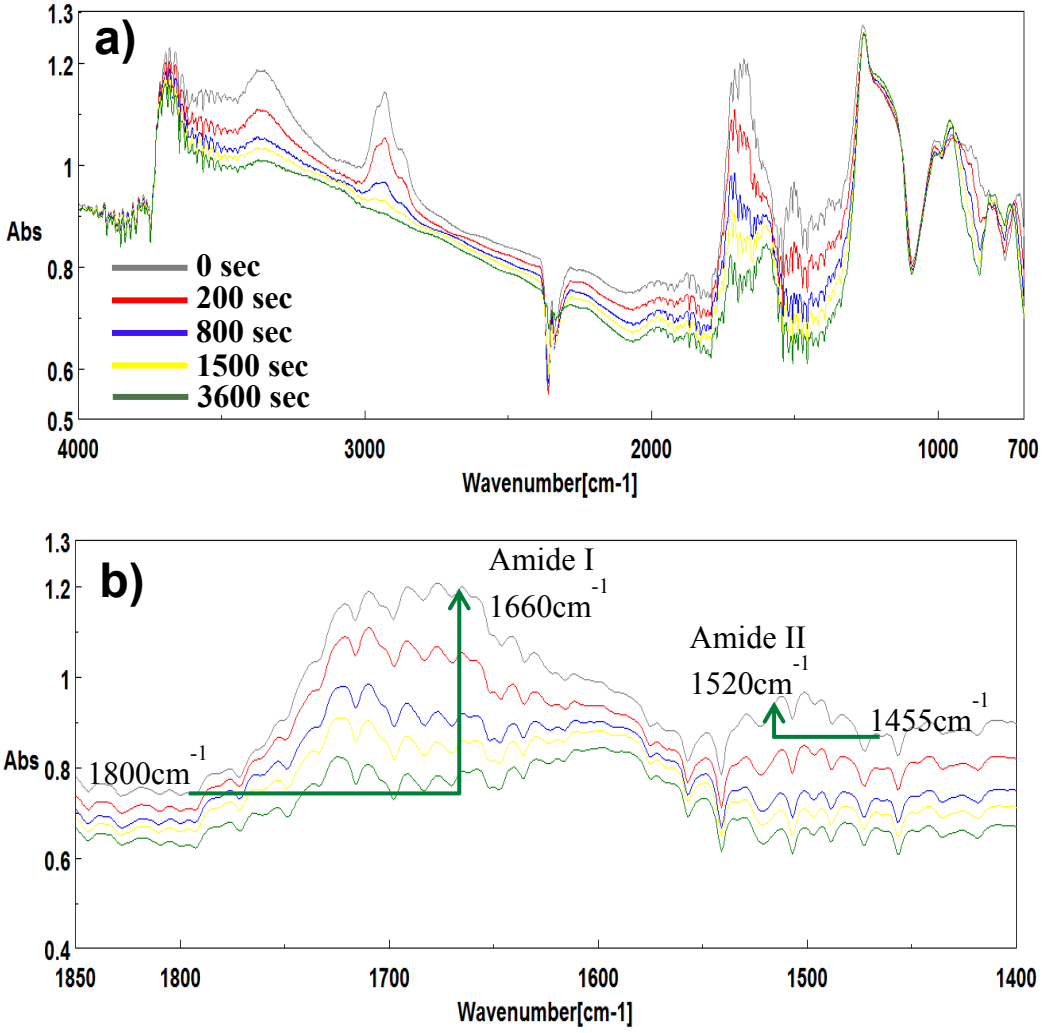

Fig.4.1. (a) IR spectral changes of diatom at 0, 200, 800, 1500 and 3600 seconds during heating experiments of an unwashed diatom on Al foil under ambient atmosphere at 300ºC.
(b) Details of the amide I and amide II region with one point baselines for amide I ($1660cm^{-1}$) and for amide II ($1520cm^{-1}$) shown on the 0 sec spectra.

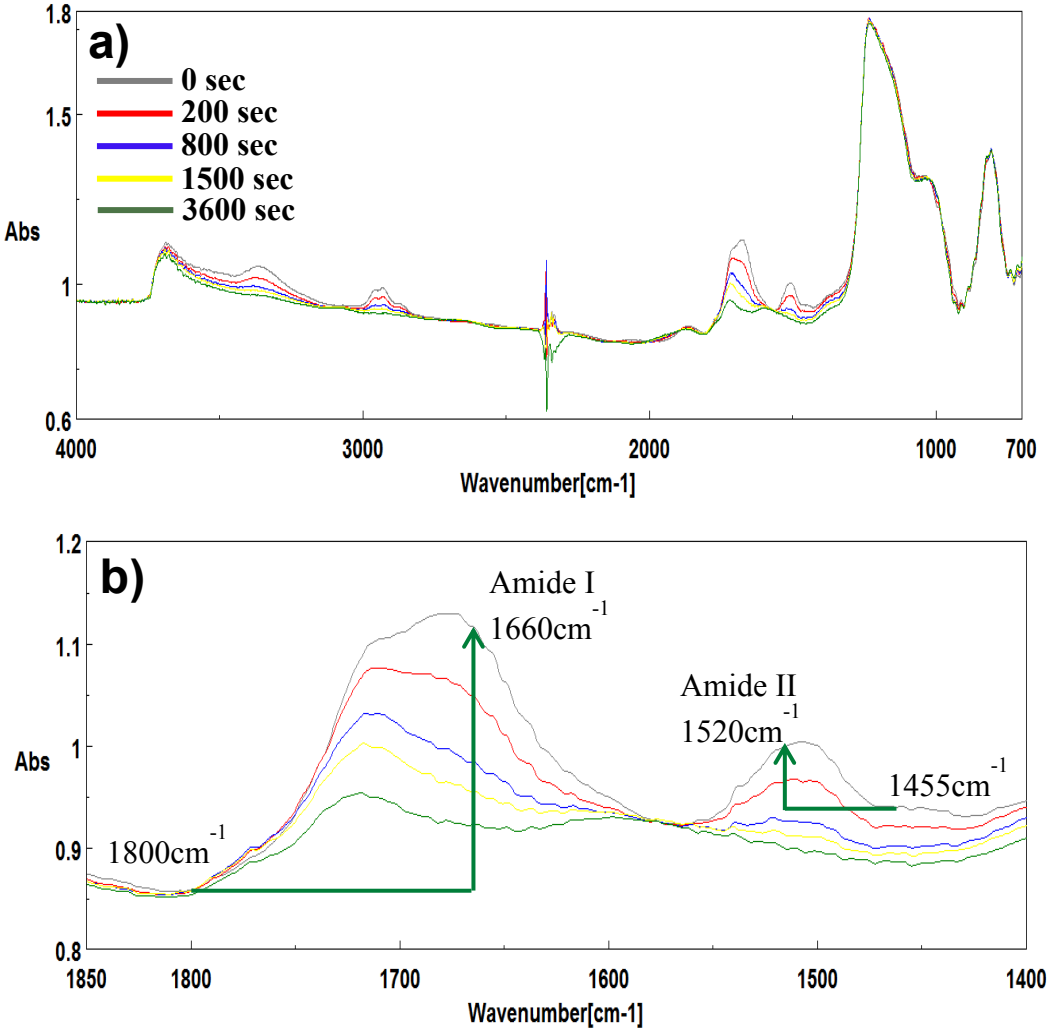

Fig.4.2. (a) IR spectral changes of diatom at 0, 200, 800, 1500 and 3600 seconds during heating experiments of an unwashed diatom on Al foil under ambient atmosphere at 290ºC.
(b) Details of the amide I and amide II region with one point baselines for amide I ($1660cm^{-1}$) and for amide II ($1520cm^{-1}$) shown on the 0 sec spectra.

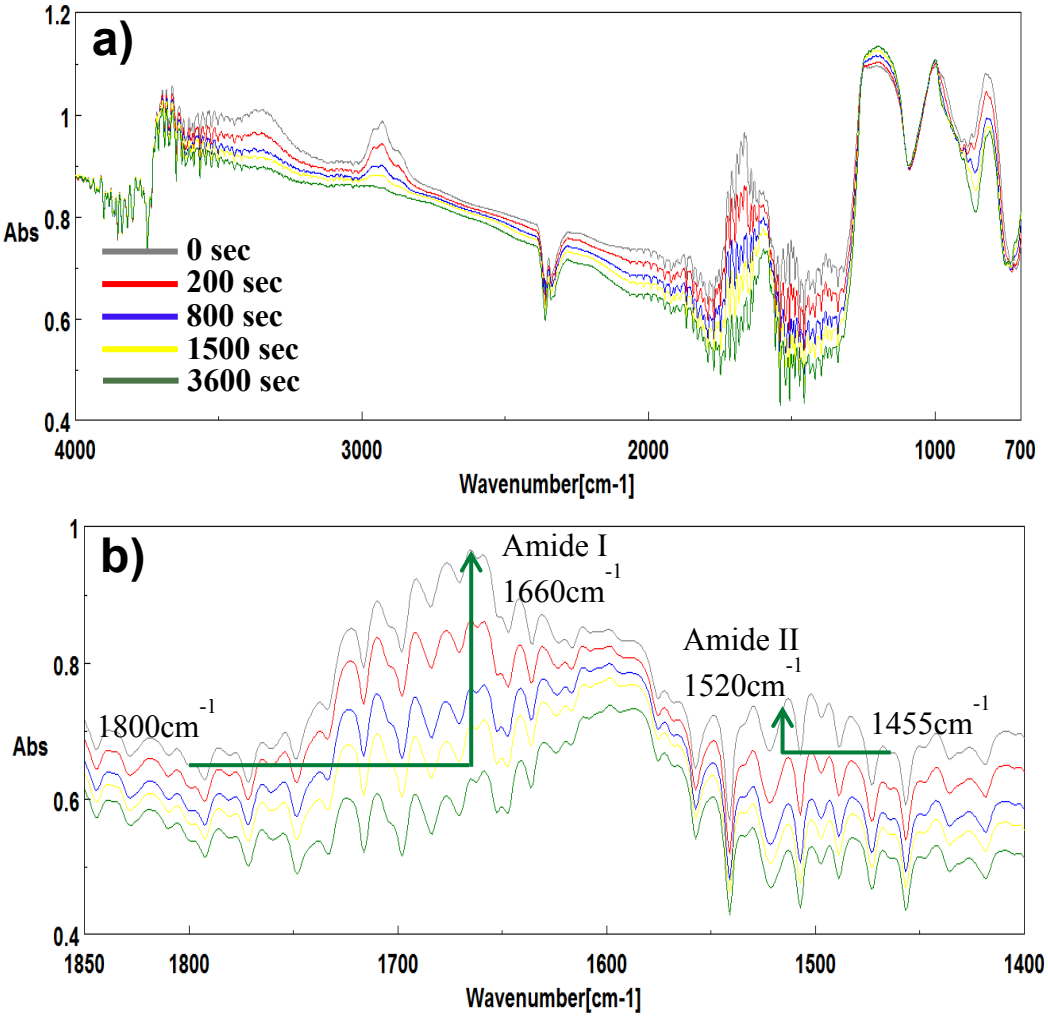

Fig.4.3. (a) IR spectral changes of diatom at 0, 200, 800, 1500 and 3600 seconds during heating experiments of an unwashed diatom on Al foil under ambient atmosphere at 280ºC.
(b) Details of the amide I and amide II region with one point baselines for amide I ($1660cm^{-1}$) and for amide II ($1520cm^{-1}$) shown on the 0 sec spectra.

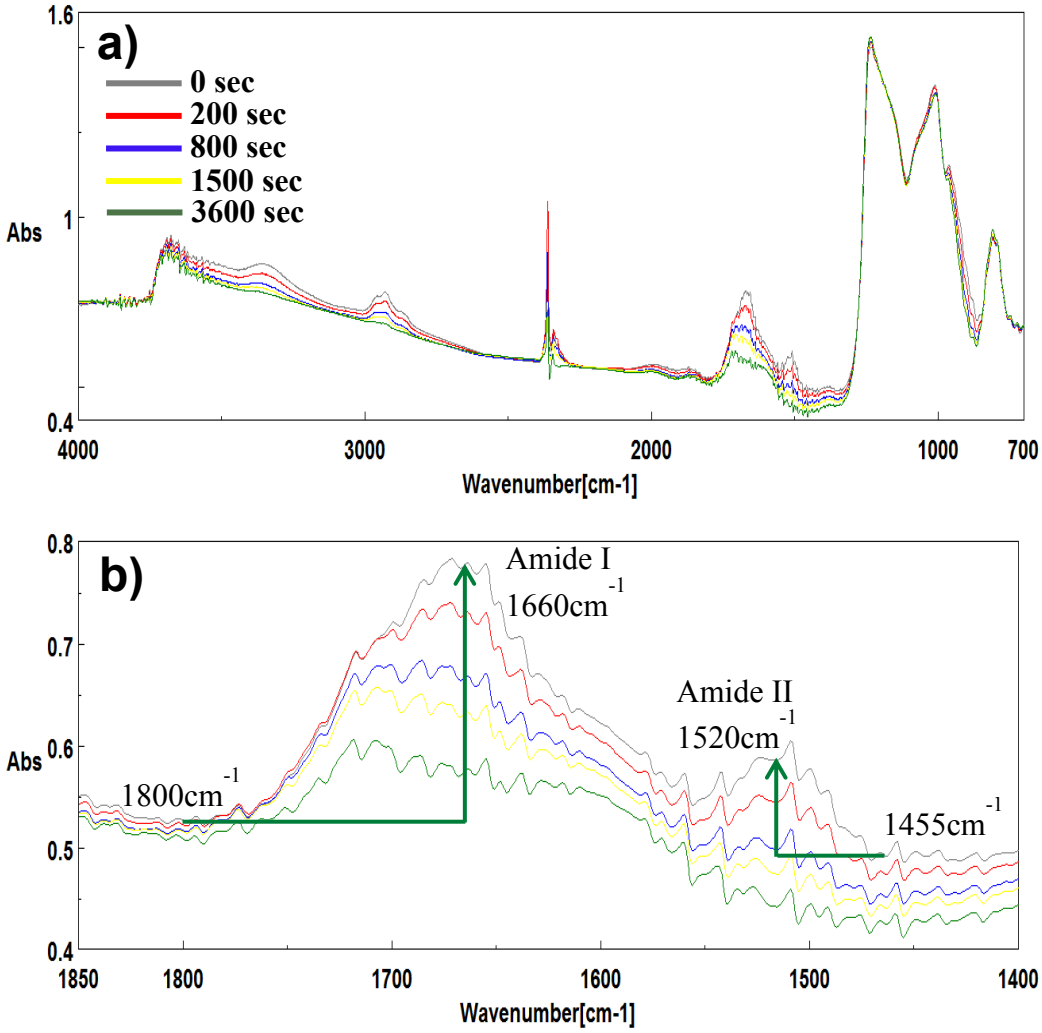

Fig.4.4. (a) IR spectral changes of diatom at 0, 200, 800, 1500 and 3600 seconds during heating experiments of an unwashed diatom on Al foil under ambient atmosphere at 270ºC.
(b) Details of the amide I and amide II region with one point baselines for amide I ($1660cm^{-1}$) and for amide II ($1520cm^{-1}$) shown on the 0 sec spectra.

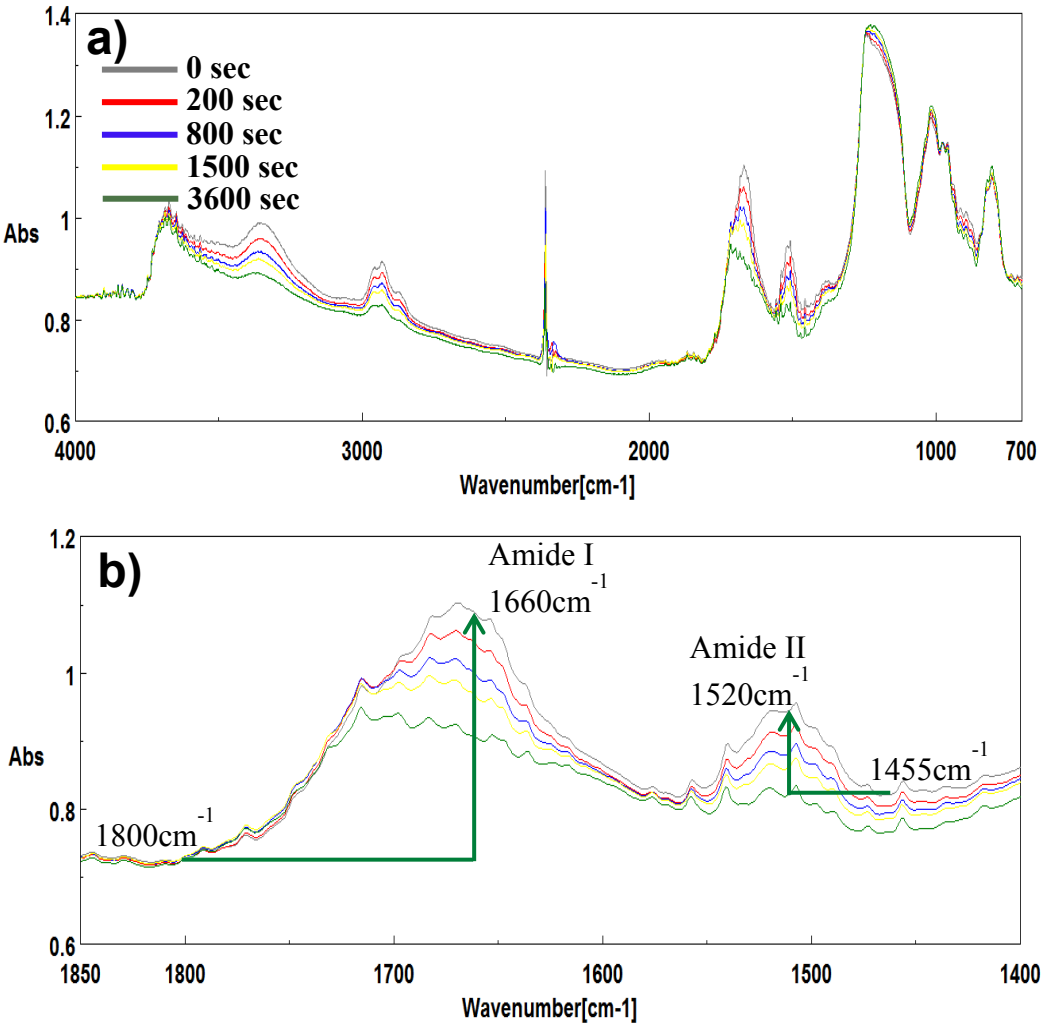

Fig.4.5. (a) IR spectral changes of diatom at 0, 200, 800, 1500 and 3600 seconds during heating experiments of an unwashed diatom on Al foil under ambient atmosphere at 260ºC.
(b) Details of the amide I and amide II region with one point baselines for amide I ($1660cm^{-1}$) and for amide II ($1520cm^{-1}$) shown on the 0 sec spectra.

In order to quantitatively examine decrease trends of amide I (1660cm^{-1}) and amide II (1520cm^{-1}) bands, two different one point baselines at 1850cm^{-1} for amide I (1660cm^{-1}) and 1455cm^{-1} for amide II (1520cm^{-1}) peaks were applied to determine their peak heights, because it was difficult to use the same linear baseline regions. Changes with time in the peak heights of amide I (1660cm^{-1}) and amide II (1520cm^{-1}) at 260 to 300ºC are shown in Fig. 4.6. The peak heights are divided by those at time zero (starting of the isothermal heating). The decrease trends of amide I and amide II are similar for all the temperatures. The decrease rates appear to be faster at higher temperatures.

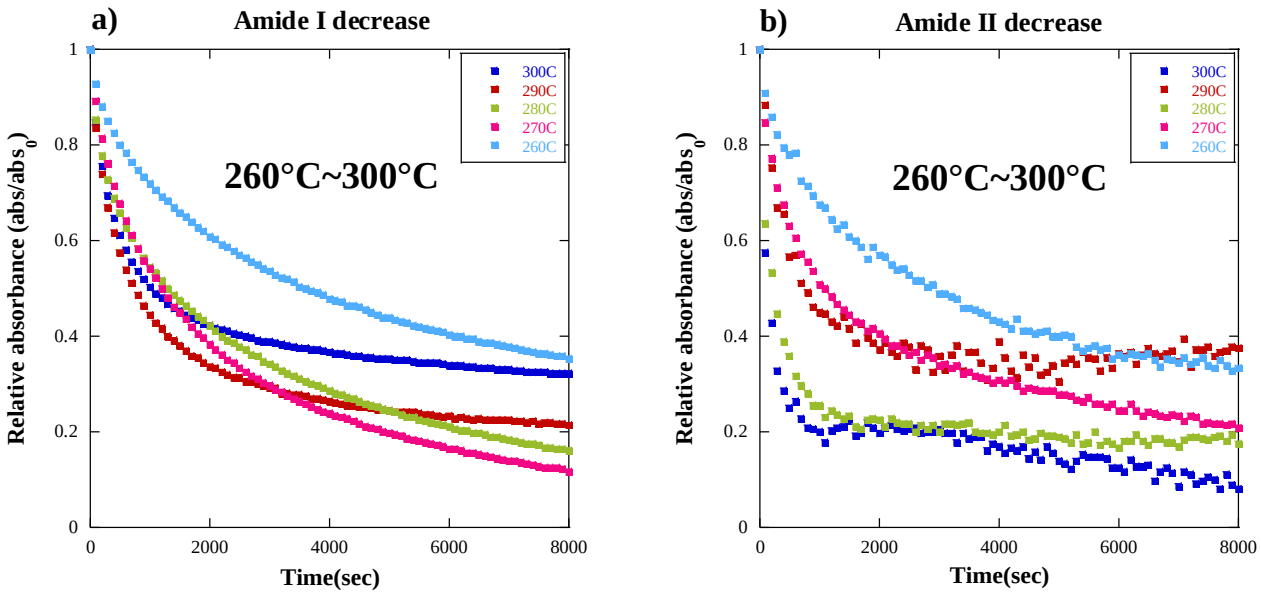

Fig.4.6. Changes with time in the peak heights of amide I and amide II.
(a) amide I at 1660cm^{-1} and (b) amide II at 1520cm^{-1} at 260, 270, 280, 290 and 300ºC.

4.4. Discussion

4.4.1. Kinetic analyses of decreases of amide I and amide II

These experimental results were analyzed by chemical reaction kinetics to determine reaction rates of amide I and amide II decreases in diatoms.

The degradation of organic functional groups is supposed to be a mixture of diverse complex multiple reactions, and separations of those reactions are often difficult. In the analyses of burial and diagenesis of organic materials in sediments and sedimentary rocks, the first order kinetics is often used for determining essentially oxidation rates of organic materials originated from dead organisms (Berner, 1980).

First, only one first order reaction model was applied to fit the experimental data by a single exponential curve. However, the fitting was very poor indicating presence of more than one first order reactions. In fact, by plotting the experimental data in Fig.4.6 in semi-logarithmic diagrams, roughly two linear regions can be recognized at initial and later stages of experiments at any temperature, especially at higher temperatures (Fig. 4.7). These two linear trends can correspond to two independent first order reactions (exponential decays): one is faster while the other one is slower.

By assuming the two first order reaction model, which was used in chapter 3, the decrease trends for amide I and amide II have been fitted by the same two exponential fitting equation for each temperature, to obtain reaction rate constants k_1 and k_2:

$$Abs = C_1 \exp(-k_1 t) + C_2 \exp(-k_2 t) + C_3$$

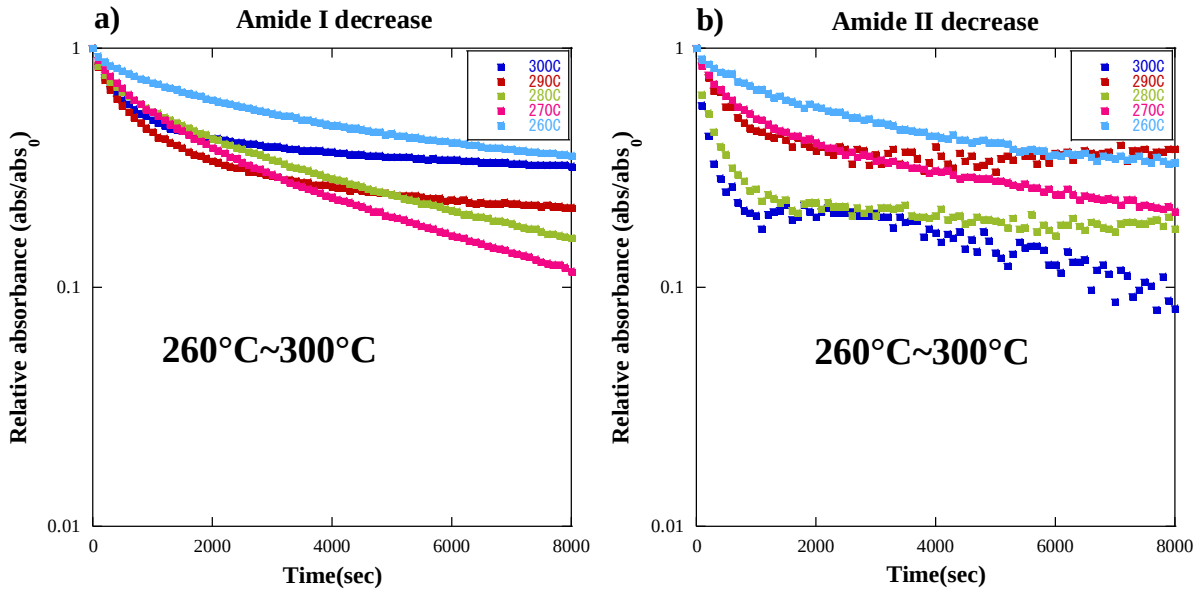

Fig.4.7. Semi-logarithmic plots for changes with time in the peak heights of (a) amide I at 1660cm^{-1} and (b) amide II at 1520cm^{-1} at 260, 270, 280, 290 and 300ºC.

4.4.2. Decrease rates of amide I and amide II

The fittings by the above two first order reaction equation of the experimental data for amide I and amide II decreases at 300°C are shown in Fig.4.8. The fittings are very well with correlation coefficient R of 0.9997 and 0.9912, suggesting the validity of the reaction model. Obtained first order rate constants for amide I at 300ºC are $k_1 = 1.1 \times 10^{-2}$ s^{-1} for the initial stage (fast) and $k_2 = 1.5 \times 10^{-3}$ s^{-1} for the later stage (slow) (Fig.4.8a). The first order rate constants for amide II at 300ºC are obtained to be $k_1 = 4.9 \times 10^{-3}$ s^{-1} for the initial stage (fast) and $k_2 = 2.8 \times 10^{-4}$ s^{-1} for the later stage (slow) (Fig.4.8b). These two rate constants are different for the faster and slower reactions of amide I and amide II (Table 4.1).

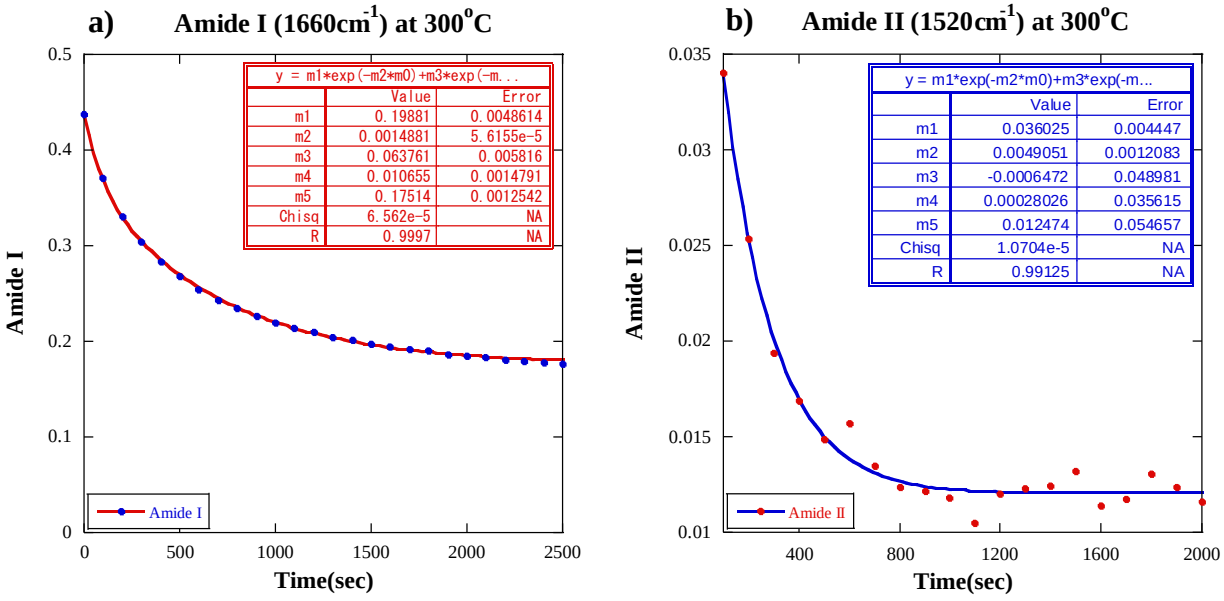

Fig.4.8. Results of curve fitting by two first order reactions ($Abs = C_1 exp(-k_1 t) + C_2 exp(-k_2 t) + C_3$), for changes with time in the peak heights of (a) amide I at 1660cm^{-1} and (b) amide II at 1520cm^{-1} at 300ºC.

	amide I ($1660cm^{-1}$) Initial fast: k_1	amide I ($1660cm^{-1}$) Later slow: k_2	amide II ($1520cm^{-1}$) Initial fast: k_1	amide II ($1520cm^{-1}$) Later slow: k_2
300ºC	$1.1 \times 10^{-2}\ s^{-1}$	$1.5 \times 10^{-3}\ s^{-1}$	$4.9 \times 10^{-3}\ s^{-1}$	$2.8 \times 10^{-4}\ s^{-1}$
290ºC	$4.8 \times 10^{-3}\ s^{-1}$	$8.1 \times 10^{-4}\ s^{-1}$	$3.0 \times 10^{-3}\ s^{-1}$	$5.9 \times 10^{-4}\ s^{-1}$
280ºC	$4.1 \times 10^{-3}\ s^{-1}$	$3.1 \times 10^{-4}\ s^{-1}$	$2.9 \times 10^{-3}\ s^{-1}$	$1.6 \times 10^{-3}\ s^{-1}$
270ºC	$3.3 \times 10^{-3}\ s^{-1}$	$4.3 \times 10^{-4}\ s^{-1}$	$1.7 \times 10^{-3}\ s^{-1}$	$9.1 \times 10^{-5}\ s^{-1}$
260ºC	$1.2 \times 10^{-3}\ s^{-1}$	$1.7 \times 10^{-4}\ s^{-1}$	$5.5 \times 10^{-4}\ s^{-1}$	$2.0 \times 10^{-4}\ s^{-1}$

Table 4.1. Summary of the first order rate constants for amide I and amide II (initial fast: k_1, later slow: k_2) at temperatures of 300-260ºC.

The fittings by the above two first order reaction equation of the experimental data for amide I and amide II decreases at 290ºC are shown in Fig.4.9. The fittings are very well with correlation coefficient R of 0.9998 and 0.9914, suggesting the validity of the reaction model. Obtained first order rate constants for amide I at 290ºC are $k_1 = 4.8 \times 10^{-3}\ s^{-1}$ for the initial stage (fast) and $k_2 = 8.1 \times 10^{-4}\ s^{-1}$ for the later stage (slow) (Fig.4.9a). The first order rate constants for amide II at 290ºC are obtained to be $k_1 = 3.0 \times 10^{-3}\ s^{-1}$ for the initial stage (fast) and $k_2 = 5.9 \times 10^{-4}\ s^{-1}$ for the later stage (slow) (Fig.4.9b). These two rate constants are different for the faster and slower reactions of amide I and amide II (Table 4.1).

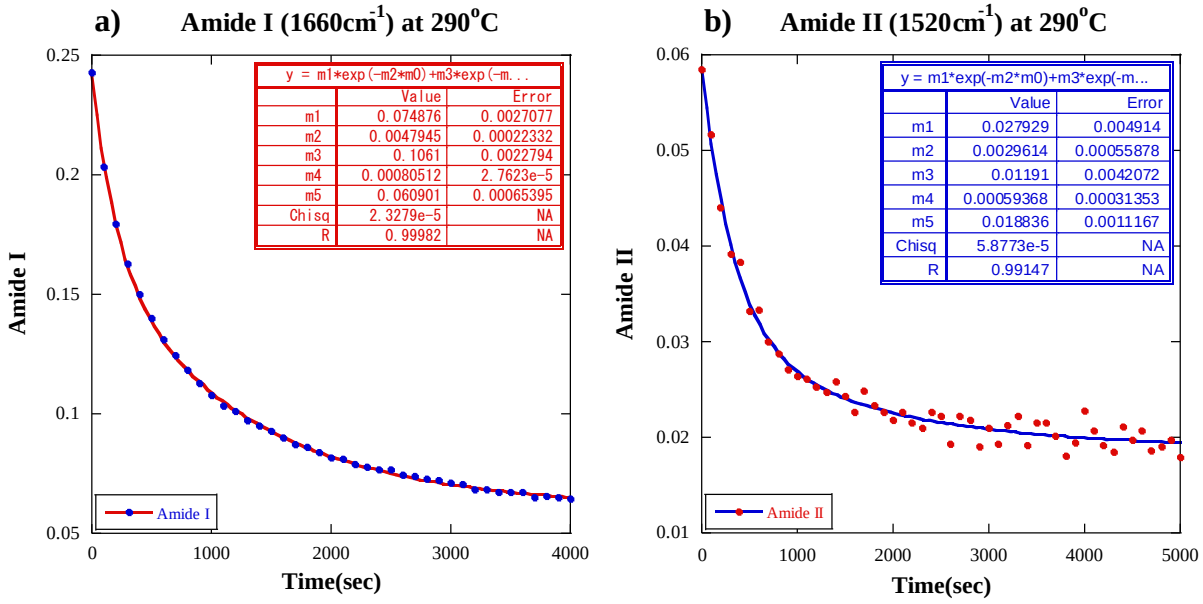

Fig.4.9. Results of curve fitting by two first order reactions (Abs = $C_1\exp(-k_1t) + C_2\exp(-k_2t) + C_3$), for changes with time in the peak heights of (a) amide I at 1660cm^{-1} and (b) amide II at 1520cm^{-1} at 290ºC.

The fittings by the above two first order reaction equation of the experimental data for amide I and amide II decreases at 280°C are shown in Fig.4.10. The fittings are very well with correlation coefficient R of 0.9996 and 0.9957, suggesting the validity of the reaction model. Obtained first order rate constants for amide I at 280ºC are $k_1 = 4.1 \times 10^{-3}$ s^{-1}, for the initial stage (fast) and $k_2 = 3.1 \times 10^{-4}$ s^{-1} for the later stage (slow) (Fig.4.10a). The first order rate constants for amide II at 280ºC are obtained to be $k_1 = 2.9 \times 10^{-3}$ s^{-1} for the initial stage (fast) and $k_2 = 1.6 \times 10^{-3}$ s^{-1} for the later stage (slow) (Fig.4.10b). These two rate constants are different for the faster and slower reactions of amide I and amide II (Table 4.1).

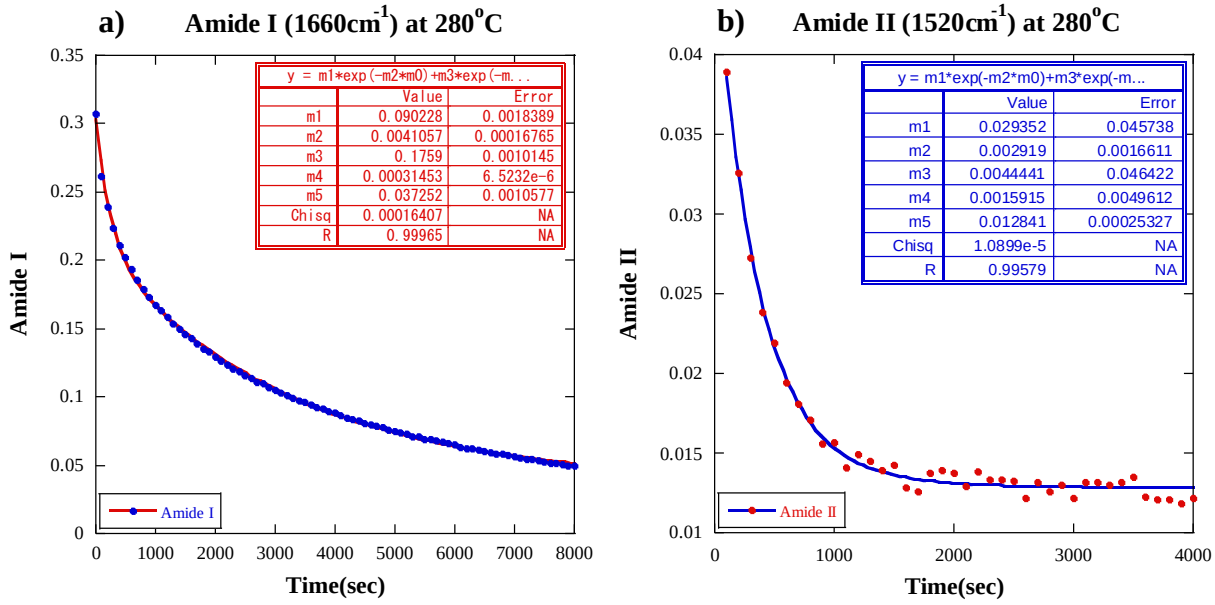

Fig.4.10. Results of curve fitting by two first order reactions (Abs = $C_1 exp(-k_1 t) + C_2 exp(-k_2 t) + C_3$), for changes with time in the peak heights of (a) amide I at 1660cm^{-1} and (b) amide II at 1520cm^{-1} at 280ºC.

The fittings by the above two first order reaction equation of the experimental data for amide I and amide II decreases at 270°C are shown in Fig.4.11. The fittings are very well with correlation coefficient R of 0.9998 and 0.9990, suggesting the validity of the reaction model. Obtained first order rate constants for amide I at 270ºC are $k_1 = 3.3 \times 10^{-3}$ s^{-1}, for the initial stage (fast) and $k_2 = 4.3 \times 10^{-4}$ s^{-1} for the later stage (slow) (Fig.4.11a). The first order rate constants for amide II at 270ºC are obtained to be $k_1 = 1.7 \times 10^{-3}$ s^{-1} for the initial stage (fast) and $k_2 = 9.1 \times 10^{-5}$ s^{-1} for the later stage (slow) (Fig.4.11b). These two rate constants are different for the faster and slower reactions of amide I and amide II (Table 4.1).

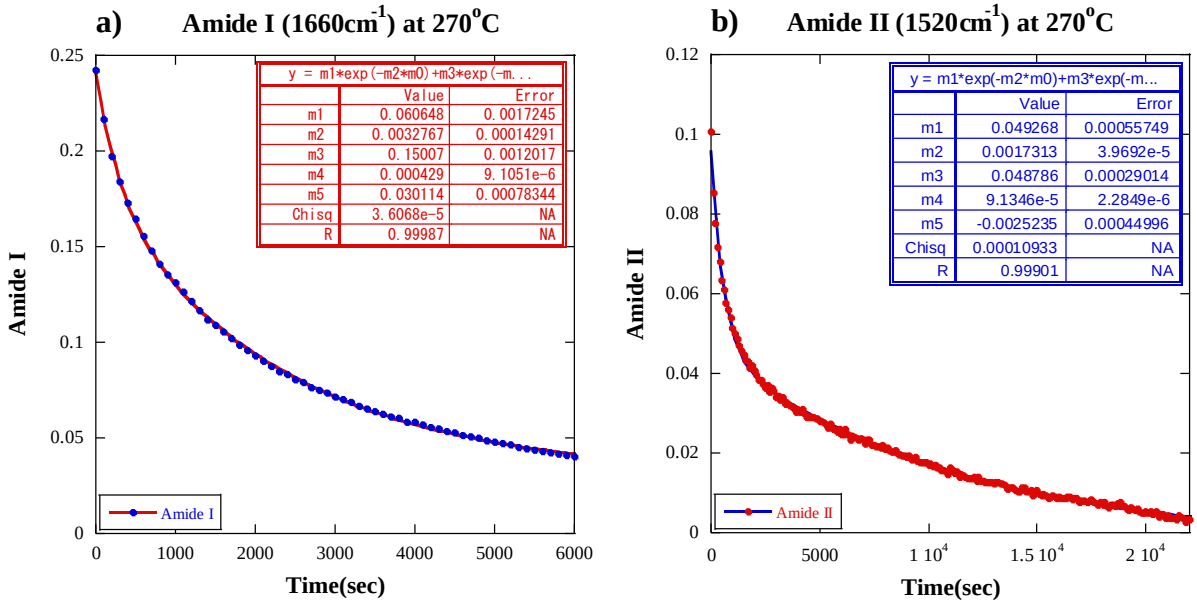

Fig.4.11. Results of curve fitting by two first order reactions (Abs = $C_1\exp(-k_1t) + C_2\exp(-k_2t) + C_3$), for changes with time in the peak heights of (a) amide I at 1660cm^{-1} and (b) amide II at 1520cm^{-1} at 270ºC.

The fittings by the above two first order reaction equation of the experimental data for amide I and amide II decreases at 260^{o}C are shown in Fig.4.12. The fittings are very well with correlation coefficient R of 0.9995 and 0.9959, suggesting the validity of the reaction model. Obtained first order rate constants for amide I at 260ºC are k_1 = 1.2 x10^{-3} s^{-1}, for the initial stage (fast) and k_2 = 1.7 x10^{-4} s^{-1} for the later stage (slow) (Fig.4.12a). The first order rate constants for amide II at 260ºC are obtained to be k_1 = 5.5 x10^{-4} s^{-1} for the initial stage (fast) and k_2 = 2.0 x10^{-4} s^{-1} for the later stage (slow) (Fig.4.12b). These two rate constants are different for the faster and slower reactions of amide I and amide II (Table 4.1).

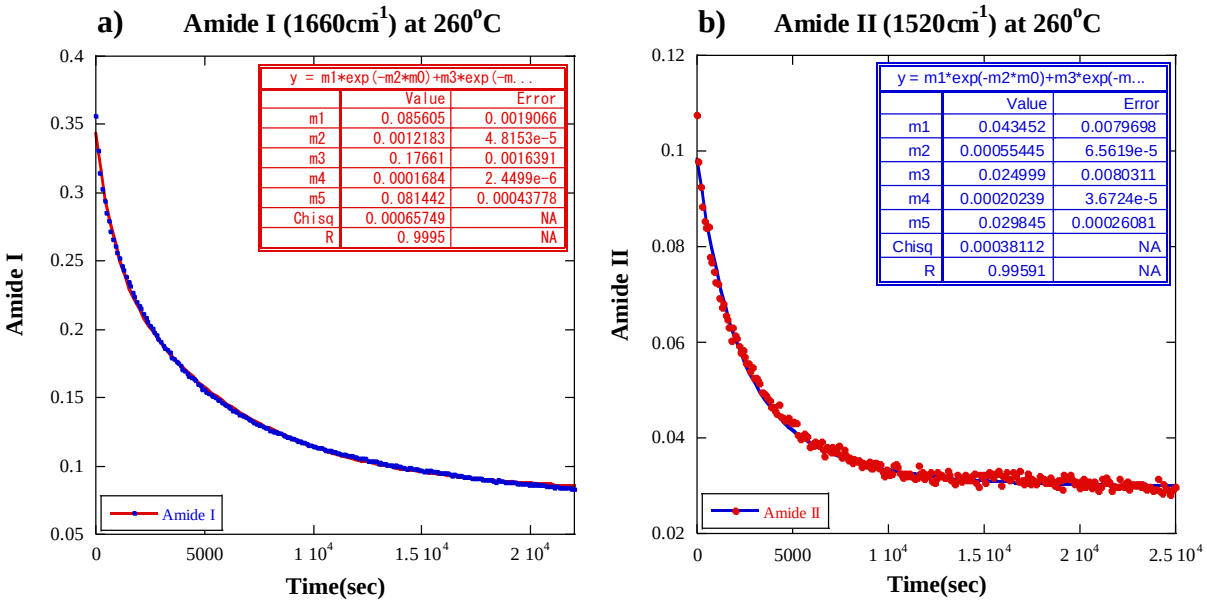

Fig.4.12. Results of curve fitting by two first order reactions (Abs = $C_1\exp(-k_1t) + C_2\exp(-k_2t) + C_3$), for changes with time in the peak heights of (a) amide I at 1660cm^{-1} and (b) amide II at 1520cm^{-1} at 260ºC.

4.4.3. Temperature dependence of decrease rates of amide bands

Temperature dependence of reaction rates can be described by the Arrhenius equation:

$$\ln(k)=\ln(A)-E_a/RT$$

where k is the rate constant, A is the pre-exponential "frequency" factor, E_a is the activation energy, R is the gas constant (R= 8.314 J/mol.K) and T is the absolute temperature (K).

Obtained first order rate constants at different temperatures for amide I and amide II, k_1 for the initial stage (fast) and k_2 for the later stage (slow), were plotted in Arrhenius diagrams in Fig.4.13a and Fig.4.13b, respectively.

The rate constants of k_1 for amide I are larger than that for amide II at all temperatures ranging from 300 to 260°C. Gradients of fitted lines of these data in Fig.4.13a give activation energies of E_a~120 kJ/mol for k_1 of amide I and E_a~123 kJ/mol for k_1 of amide II at the temperature range from 300 to 260°C.

The rate constants of k_2 for amide I are larger than those for amide II at 300, 290 and 270°C, but they are smaller than those of amide II at 280 and 260°C. Gradients of fitted lines of these data in Fig.4.13b give activation energies of E_a~126 kJ/mol for k_2 of amide I and E_a~ 62 kJ/mol for k_2 of amide II at the temperature range from 300 to 260°C.

These reaction rate constants and activation energies for amide I and II bands of proteins will be discussed in the summary and general discussion (chapter 6).

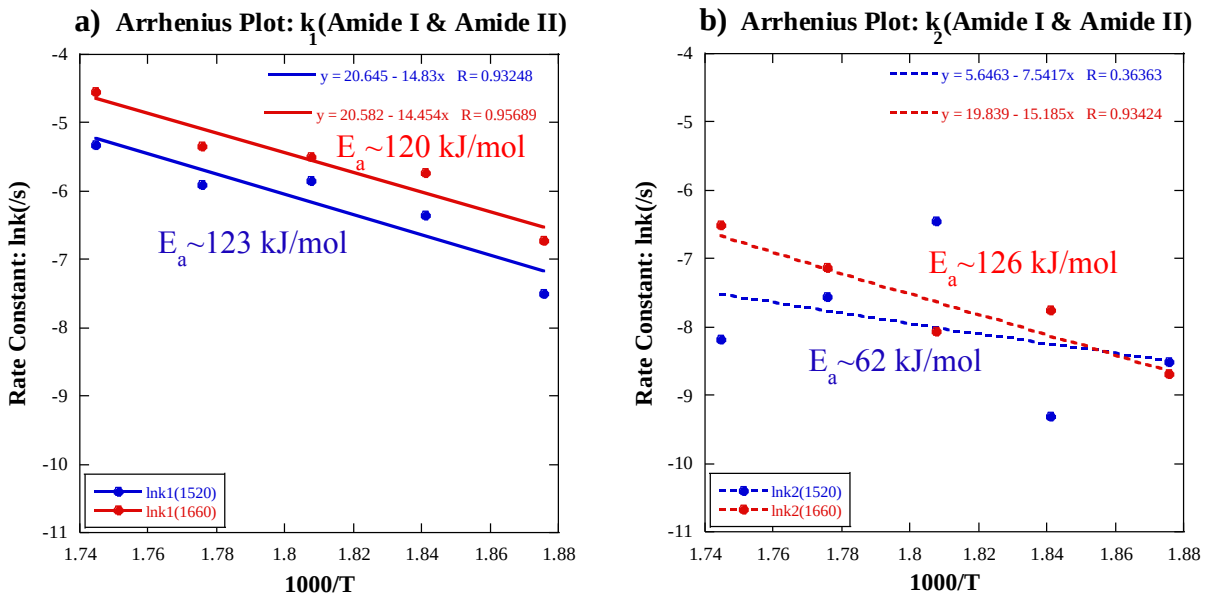

Fig.4.13. Arrhenius diagrams for the rate constants k as a function of temperature T (K) determined by two first order reactions for diatom heating experiments in Figs. 4.8 to 4.12.
(a) k_1 for amide I at 1660cm^{-1} and amide II at 1520cm^{-1} at the temperature range of 300-260ºC.
(b) k_2 for amide I at 1660cm^{-1} and amide II at 1520cm^{-1} at the temperature range of 300-260ºC.

Chapter 5. Changes in silica during in-situ heating IR microspectroscopy of unwashed diatoms

5.1. Introduction

As it stated in the introduction of chapter 3, dead bodies of marine diatoms are sedimented on the ocean floor and buried in marine sediments with time. During their burial, temperature and pressure increase and organic components in diatom bodies are transformed. Silica is also transformed from amorphous hydrous silica (Opal-A) via cristobalite (Opal-C) to quartz (Qz) (Pollastro, 1993). Although generation of hydrocarbons from diatoms is considered to be related to transformation of organic components during the burial-diagenesis (Tissot and Welt, 1984), detailed relations of aliphatic hydrocarbon release and silica transformation are not known. In this chapter, silica transformation processes are studied during the same in situ heating IR transflection microspectroscopy on diatom frustules as chapters 3 and 4 and kinetic parameters (reaction rate constants and activation energies) for silica (the 3650cm^{-1} band due to stretching of O-H bound to Si and the 805cm^{-1} band due to symmetric Si-O stretching vibration) have been evaluated.

5.2. Methods

5.2.1. In situ isothermal heating experiments by micro-FTIR spectroscopy

The same unwashed centric diatoms (*Arachnoidiscus ornatus*, diameters: 100-350 μm) were mounted on Al plates without using any adhesive for measuring IR spectral changes at high temperatures in the heating stage (Linkam TS-1500) under the IR microspectrometer (FTIR-620+IRT30, JASCO Co., Ltd). The temperature of the sample was monitored just below the Al plate and increased at a rate of 50^{o}C/minute up to the desired temperature (260, 270, 280, 290 or 300°C). Since no window materials were set in the heating stage, the diatom sample was heated in an ambient air atmosphere.

A background reflection spectrum on a 100×100μm^2 aperture area was first measured on a diatom free Al plate at room temperature by accumulating 100 scans with 4cm^{-1} resolution in the 4000-700cm^{-1} wavenumber range. The sample transflection spectrum was measured on a diatom sample mounted on an Al plate at room temperature. Then the diatom sample on the Al plate in the heating stage was heated at a rate of 50^{o}C/minute up to the desired temperature (260, 270, 280, 290 or 300°C), which was kept constant during the following IR spectral measurements. A series of IR transflection (transmission-reflection) spectra was measured on the same position of the diatom sample on the Al plate at every 100 seconds. These transflection signals were divided by the above background spectrum on the diatom-free Al plate at room temperature.

5.3. Results

5.3.1. Changes in silica of diatoms during isothermal heating experiments

Isothermal heating in situ IR-microspectroscopy has been applied to diatom silica frustules to collect a time series data sets at different temperatures (260, 270, 280, 290 and 300°C). Representative IR spectral changes with time during heating experiments of diatom frustuls on Al foils under ambient atmospheric condition at 300, 290, 280, 270 and 260ºC are shown in Figs. 5.1-5.5.

Although the trends of peak changes are similar at all temperatures but on different time scales, peak heights of SiOH (3650cm^{-1}) decreased with time. On the other hand, the bands around 1000 to 750cm^{-1} including Si-OH (960cm^{-1}) and SiOSi (805cm^{-1}) bands (chapter 2) changed greatly with heating possibly due to silica transformation.

The SiO-H band was around 3650cm^{-1} at room temperature but shifted to higher wavenumber region around 3680cm^{-1} at higher temperatures (300-260^{o}C). This shift with temperature was already reported and considered to be due to decrease of hydrogen bonding leading to more isolated surface Si-OH species (Yamagishi et al., 1997). Since it is difficult to take the same baseline region, one point base at 3750cm^{-1} (the stable minima)

was selected for determining peak heights around 3680-3650cm^{-1} (Figs. 5.1-5.5). The peak heights at 3680cm^{-1} showed increasing trends in some data due possibly to formation of isolated Si-OH upon dehydration. Therefore, the peak height at 3650cm^{-1} was selected here for further quantitative analyses.

The Si-O-Si stretching band at room temperature was at around 805cm^{-1} and showed an increase at higher temperatures, but another band around 880cm^{-1} also increased except for 290^{o}C (Figs. 5.1-5.5). The 880cm^{-1} band was reported in dehydroxylation of silica particles (Grabbe et al., 1995; Ceresoli et al., 2000) and assigned to unhydrate ordered Si-O-Si structures (Liu and Shen, 2008). Since it is difficult to take the same baseline region or one point base points near to the 805cm^{-1} band, one point base at 1350cm^{-1} (the most stable point) was selected for determining peak heights at 805cm^{-1} (Figs. 5.1-5.5). The peak heights at 880cm^{-1} were also analyzed but they did not show systematic changes. Therefore, only the peak height changes of 805cm^{-1} band was analyzed below.

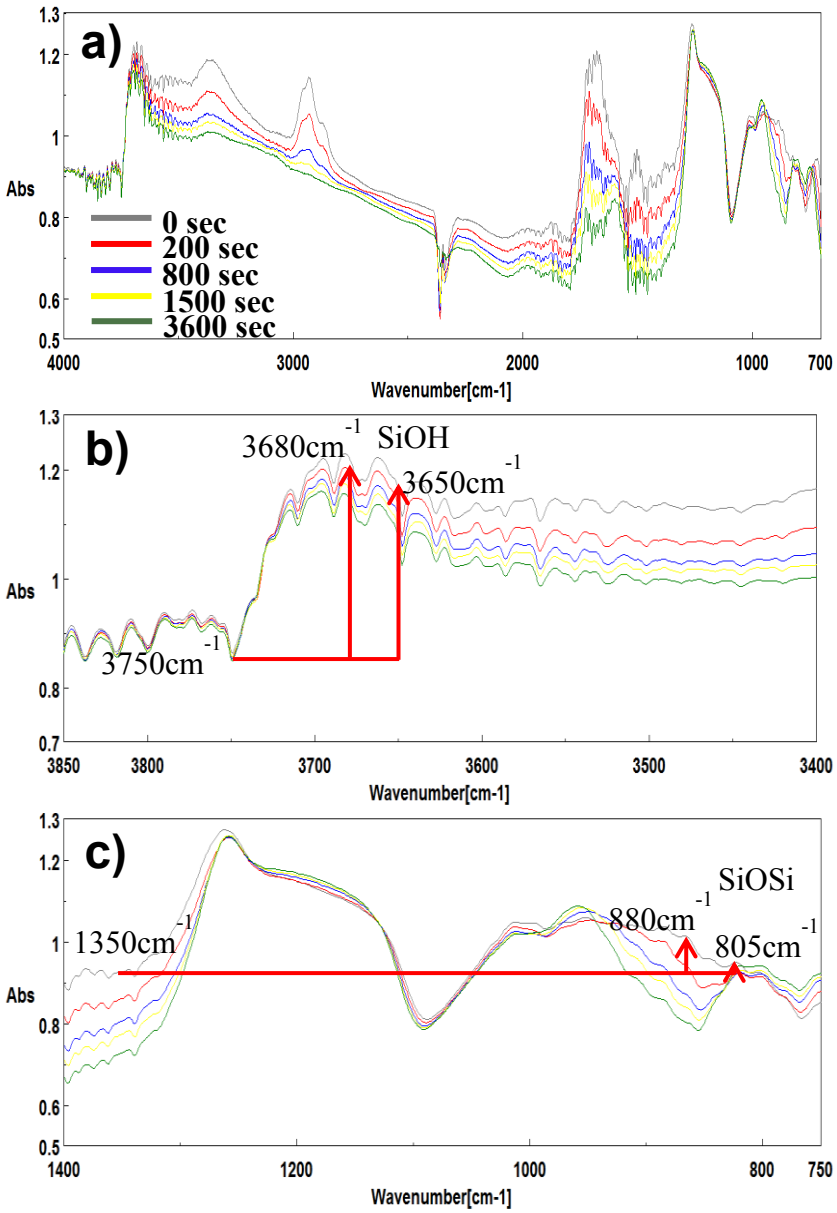

Fig.5.1. (a) IR spectral changes of diatom at 0, 200, 800, 1500 and 3600 seconds during heating experiments of an unwashed diatom on Al foil under ambient atmosphere at 300ºC. (b) Details of the silica regions with one point baselines for SiOH at 3650cm^{-1} & 3680cm^{-1} and for SiOSi at 805cm^{-1} & 880cm^{-1} shown on the 0 sec spectra.

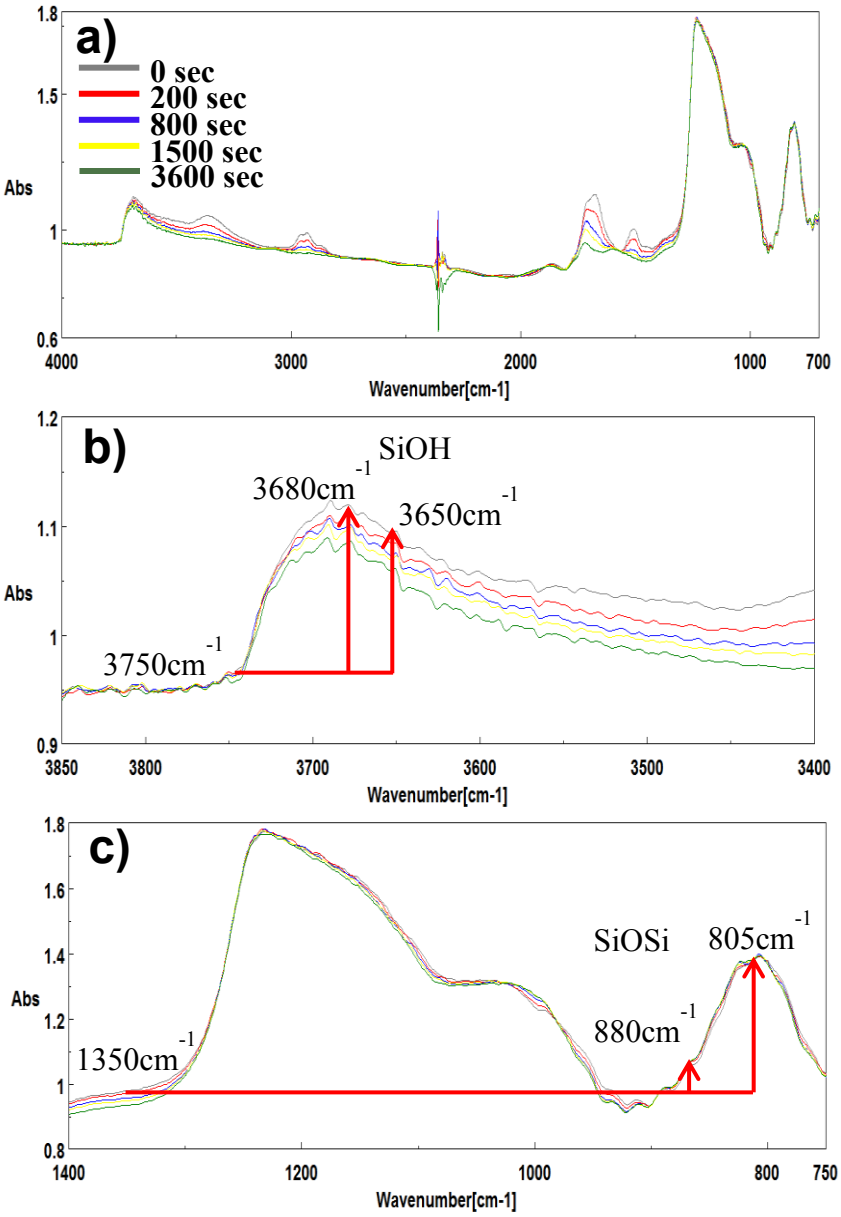

Fig.5.2. (a) IR spectral changes of diatom at 0, 200, 800, 1500 and 3600 seconds during heating experiments of an unwashed diatom on Al foil under ambient atmosphere at 290ºC. (b) Details of the silica regions with one point baselines for SiOH at 3650cm^{-1} & 3680cm^{-1} and for SiOSi at 805cm^{-1} & 880cm^{-1} shown on the 0 sec spectra.

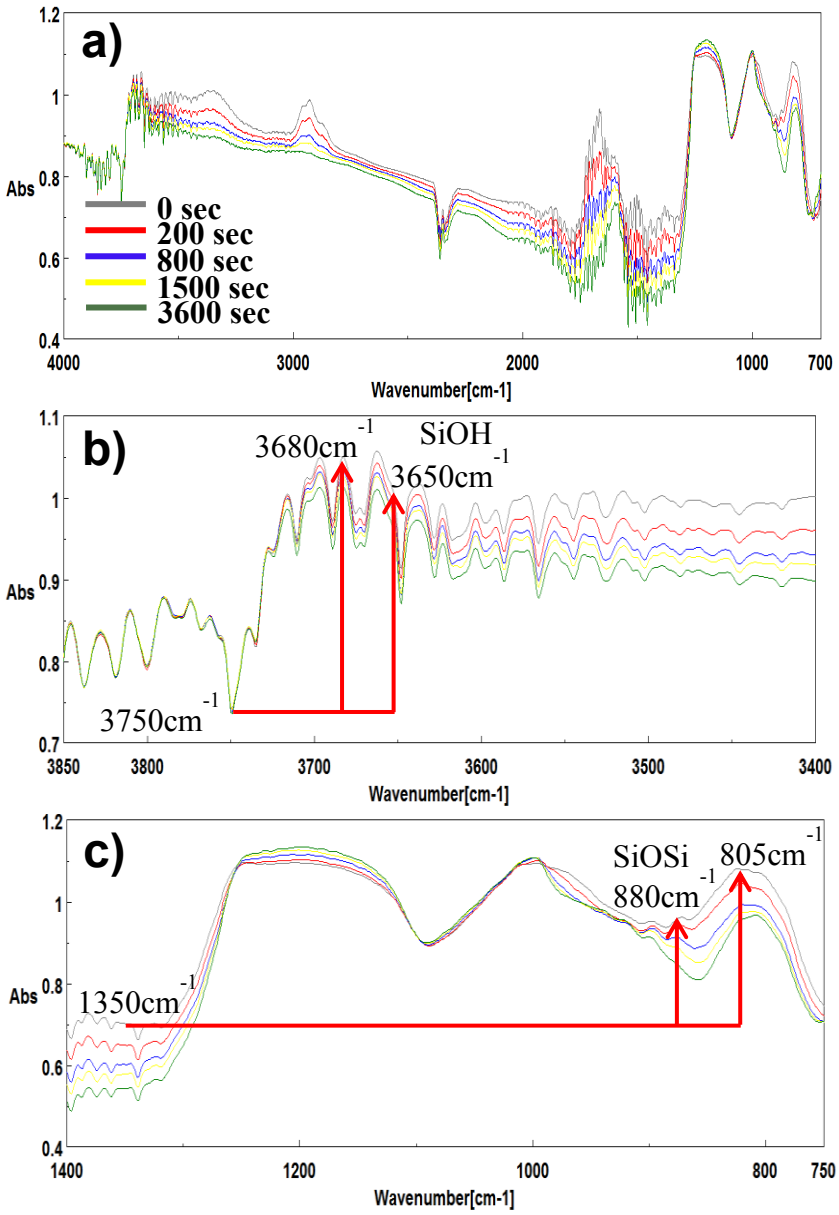

Fig.5.3. (a) IR spectral changes of diatom at 0, 200, 800, 1500 and 3600 seconds during heating experiments of an unwashed diatom on Al foil under ambient atmosphere at 280ºC. (b) Details of the silica regions with one point baselines for SiOH at 3650cm^{-1} & 3680cm^{-1} and for SiOSi at 805cm^{-1} & 880cm^{-1} shown on the 0 sec spectra.

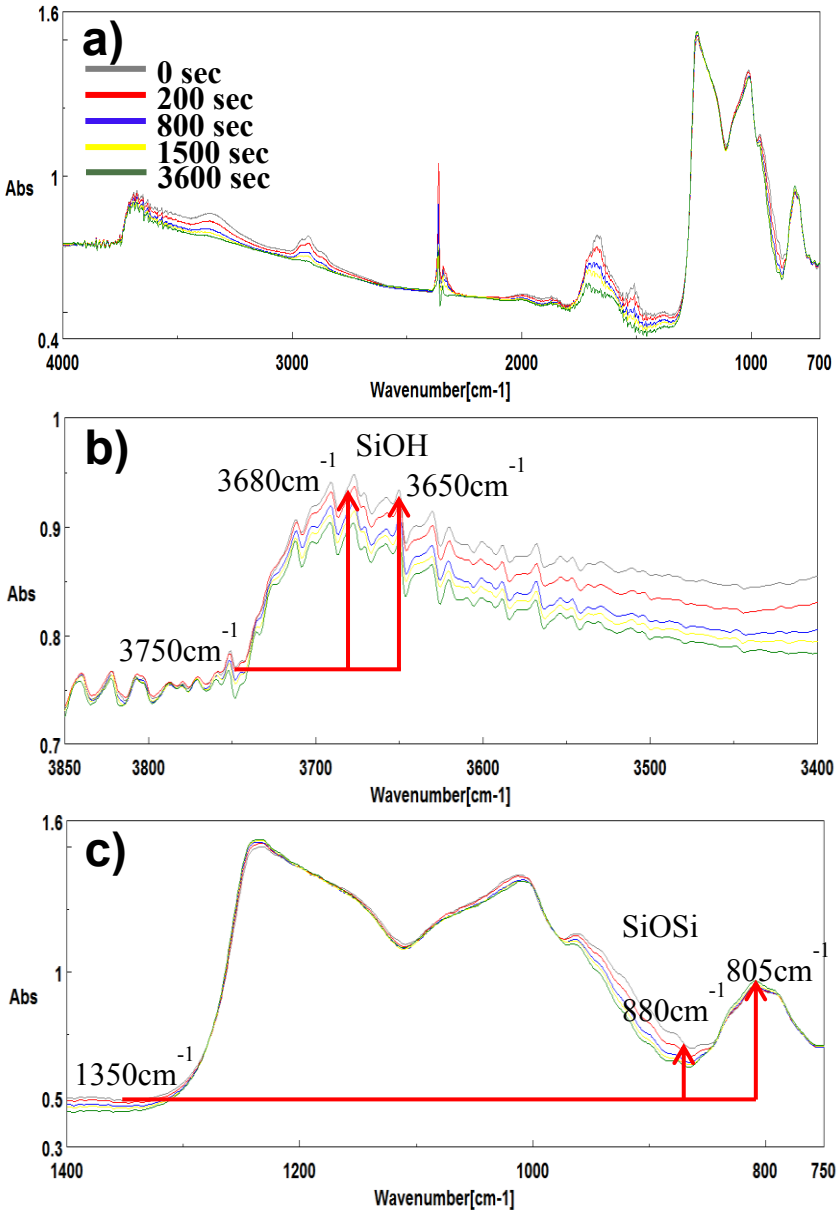

Fig.5.4. (a) IR spectral changes of diatom at 0, 200, 800, 1500 and 3600 seconds during heating experiments of an unwashed diatom on Al foil under ambient atmosphere at 270ºC. (b) Details of the silica regions with one point baselines for SiOH at 3650cm^{-1} & 3680cm^{-1} and for SiOSi at 805cm^{-1} & 880cm^{-1} shown on the 0 sec spectra.

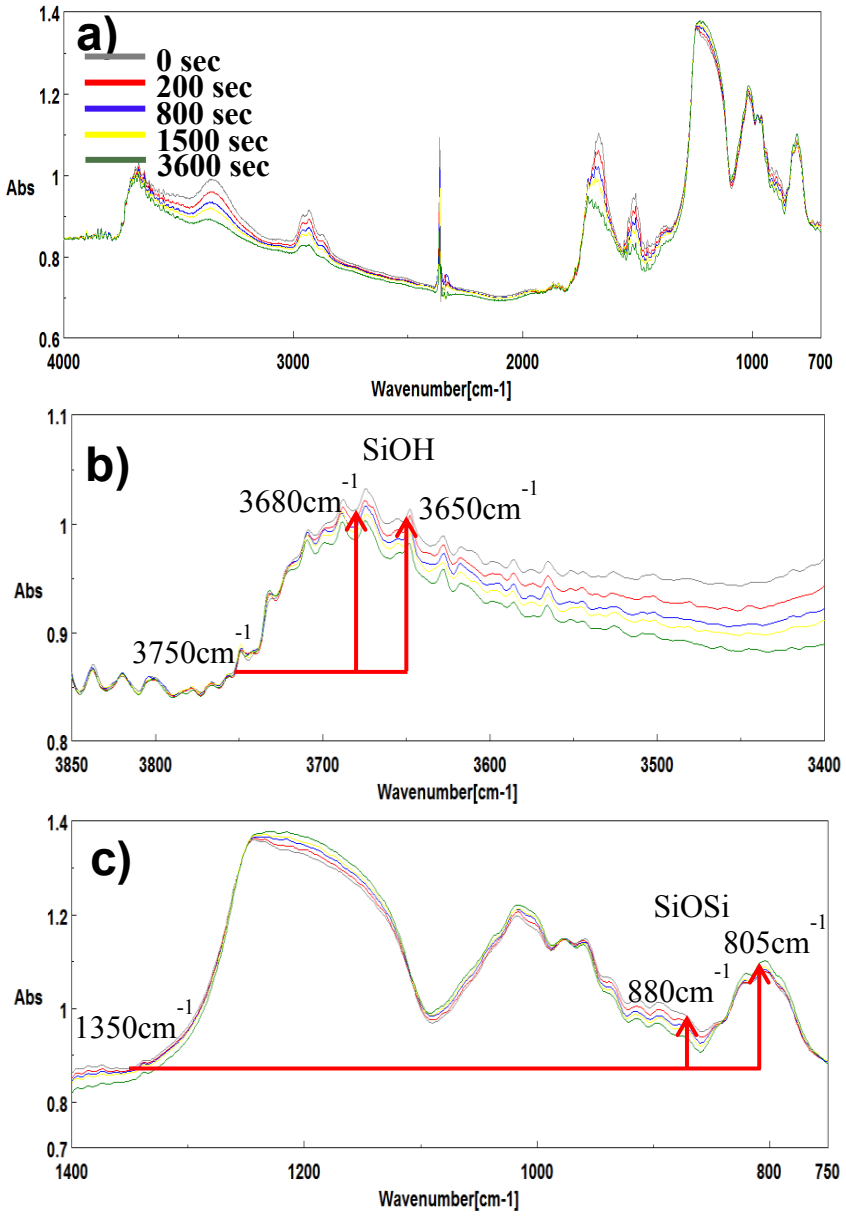

Fig.5.5. (a) IR spectral changes of diatom at 0, 200, 800, 1500 and 3600 seconds during heating experiments of an unwashed diatom on Al foil under ambient atmosphere at 260ºC. (b) Details of the silica regions with one point baselines for SiOH at 3650cm^{-1} & 3680cm^{-1} and for SiOSi at 805cm^{-1} & 880cm^{-1} shown on the 0 sec spectra.

5.3.2. Changes in peak heights of 3650cm^{-1} and 805cm^{-1} bands of diatom frustules during isothermal heating experiments

In order to quantitatively examine changes of SiOH (3650cm^{-1}) and SiO (805cm^{-1}) bands, two different one point baselines at 3750cm^{-1} for SiOH at 3650cm^{-1} and 1350cm^{-1} for SiO at 805cm^{-1} were applied to determine their peak heights. Changes with time in the peak heights of SiOH (3650cm^{-1}) and SiO (805cm^{-1}) at 260 to 300ºC are shown in Fig. 5.6. The peak heights are divided by those at time zero (starting of the isothermal heating). The decrease trends of SiOH and increase trends of SiO are similar for all the temperatures. The decrease rates appear to be faster at higher temperatures.

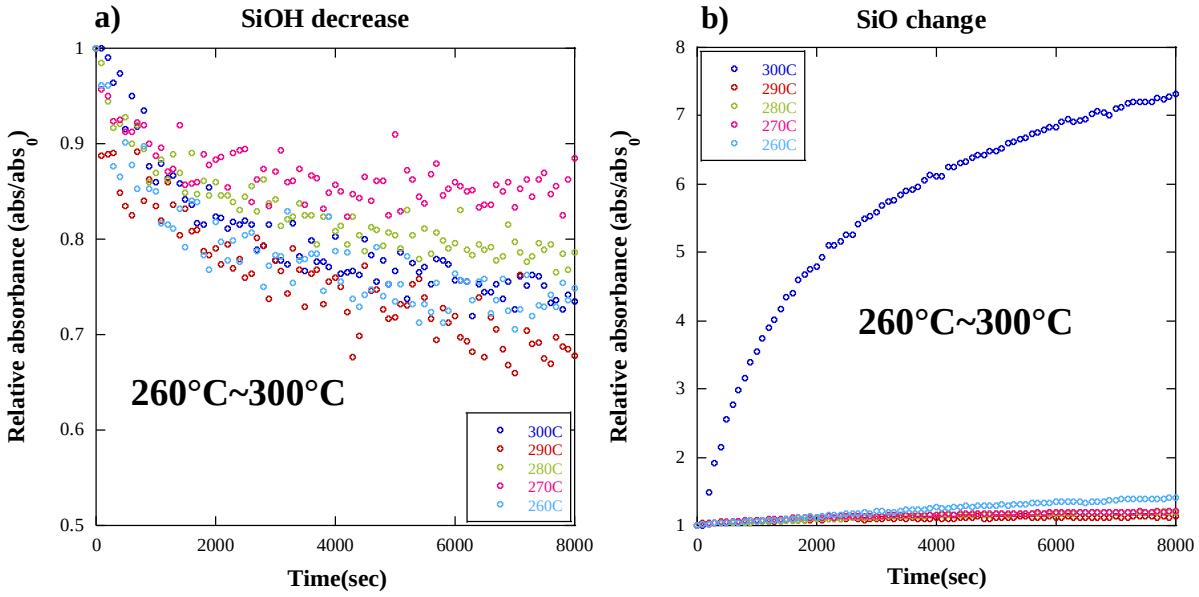

Fig.5.6. Changes with time in the peak heights of silica. (a) SiOH at 3650cm^{-1} and (b) SiO at 805cm^{-1} at 260, 270, 280, 290 and 300ºC.

5.4. Discussion

5.4.1. Kinetic analyses of Changes of SiOH and SiO

The above experimental results were analyzed by chemical reaction kinetics to determine reaction rates of SiOH decrease and SiO increase in diatoms. Since the first order reaction model was employed to analyze decrease rates of aliphatic CH_2, CH_3 and amide I and II bands, the same method was applied to SiOH and SiO bands.

First, only one first order reaction model was applied to fit the experimental data by a single exponential curve. However, the fitting was very poor indicating presence of more than one first order reactions. In fact, by plotting the experimental data in Fig.5.6 in semi-logarithmic diagrams, roughly two linear regions can be recognized at initial and later stages of experiments at any temperature, especially at higher temperatures (Fig.5.7). These two linear trends can correspond to two independent first order reactions: one is faster while the other one is slower.

By assuming the two first order reaction model, which was used in chapters 3 and 4, the decrease of SiOH and the increase of SiO have been fitted by the same two exponential fitting equations to obtain reaction rate constants k_1 and k_2 for each temperature:

$$Abs = C_1 \exp(-k_1 t) + C_2 \exp(-k_2 t) + C_3$$

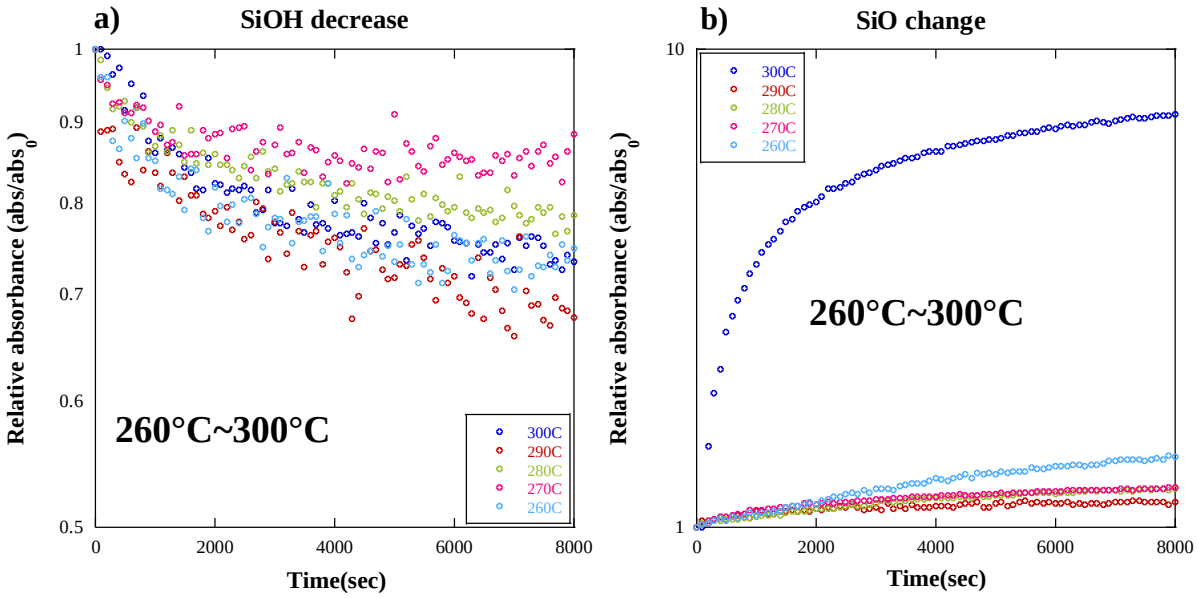

Fig.5.7. Semi-logarithmic plots for changes with time in the peak heights of silica. (a) SiOH at 3650 cm^{-1} and (b) SiO at 805 cm^{-1} at 260, 270, 280, 290 and 300ºC.

5.4.2. Decrease rates of SiOH and increase rates of SiO

The fittings by the above two first order reaction equation of the experimental data for silica changes at 300°C are shown in Fig.5.8. The fittings for SiOH are rather well with correlation coefficient R of 0.9731 and very well for SiO with correlation coefficient R of 0.9995, suggesting the validity of the reaction model. Obtained first order rate constants for SiOH at 300ºC are k_1 = 1.0 x10^{-3} s^{-1} for the initial stage (fast) and k_2 = 1.4 x10^{-4} s^{-1} for the later stage (slow) (Fig.5.8a). The first order rate constants for SiO at 300ºC are obtained to be k_1 = 1.9 x10^{-3} s^{-1} for the initial stage (fast) and k_2 = 2.6 x10^{-4} s^{-1} for the later stage (slow) (Fig.5.8b). These two rate constants are roughly in the same orders for the faster and slower reactions of silica (Table 5.1).

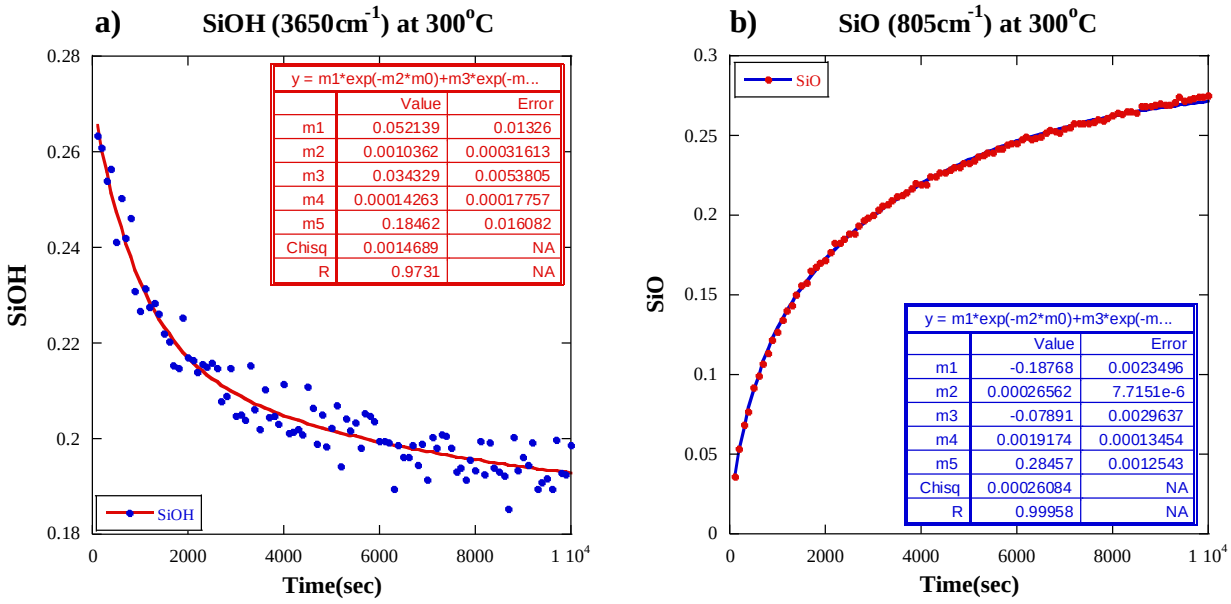

Fig.5.8. Results of curve fitting by two first order reactions (Abs = $C_1exp(-k_1t) + C_2exp(-k_2t) + C_3$), for changes with time in the peak heights of silica for (a) SiOH at 3650cm^{-1} and (b) SiO at 805cm^{-1} at 300ºC.

	SiOH ($3650\ cm^{-1}$) Initial fast: k_1	SiOH ($3650\ cm^{-1}$) Later slow: k_2	SiO ($805\ cm^{-1}$) Initial fast: k_1	SiO ($805\ cm^{-1}$) Later slow: k_2
300ºC	$1.0 \times 10^{-3}\ s^{-1}$	$1.4 \times 10^{-4}\ s^{-1}$	$1.9 \times 10^{-3}\ s^{-1}$	$2.6 \times 10^{-4}\ s^{-1}$
290ºC	$1.2 \times 10^{-3}\ s^{-1}$	$1.5 \times 10^{-4}\ s^{-1}$	$5.0 \times 10^{-4}\ s^{-1}$	$2.0 \times 10^{-4}\ s^{-1}$
280ºC	$1.6 \times 10^{-3}\ s^{-1}$	$2.1 \times 10^{-4}\ s^{-1}$	$2.5 \times 10^{-4}\ s^{-1}$	$1.7 \times 10^{-4}\ s^{-1}$
270ºC	$7.3 \times 10^{-4}\ s^{-1}$	$2.7 \times 10^{-4}\ s^{-1}$	$9.7 \times 10^{-4}\ s^{-1}$	$1.2 \times 10^{-4}\ s^{-1}$
260ºC	$4.0 \times 10^{-4}\ s^{-1}$	$7.9 \times 10^{-5}\ s^{-1}$	$1.6 \times 10^{-4}\ s^{-1}$	$3.5 \times 10^{-5}\ s^{-1}$

Table 5.1. Summary of the first order rate constants for SiOH and SiO (initial fast: k_1, later slow: k_2) at temperatures of 300-260ºC.

The fittings by the above two first order reaction equation of the experimental data for silica changes at 290°C are shown in Fig.5.9. The fittings are rather well with correlation coefficient R of 0.9429 and 0.9227, suggesting the validity of the reaction model. Obtained first order rate constants for SiOH at 290ºC are $k_1 = 1.2 \times 10^{-3}\ s^{-1}$ for the initial stage (fast) and $k_2 = 1.5 \times 10^{-4}\ s^{-1}$ for the later stage (slow) (Fig.5.9a). The first order rate constants for SiO at 290ºC are obtained to be $k_1 = 5.0 \times 10^{-4}\ s^{-1}$ for the initial stage (fast) and $k_2 = 2.0 \times 10^{-4}\ s^{-1}$ for the later stage (slow) (Fig.5.9b). These two rate constants are different for the faster and slower reactions of silica (Table 5.1).

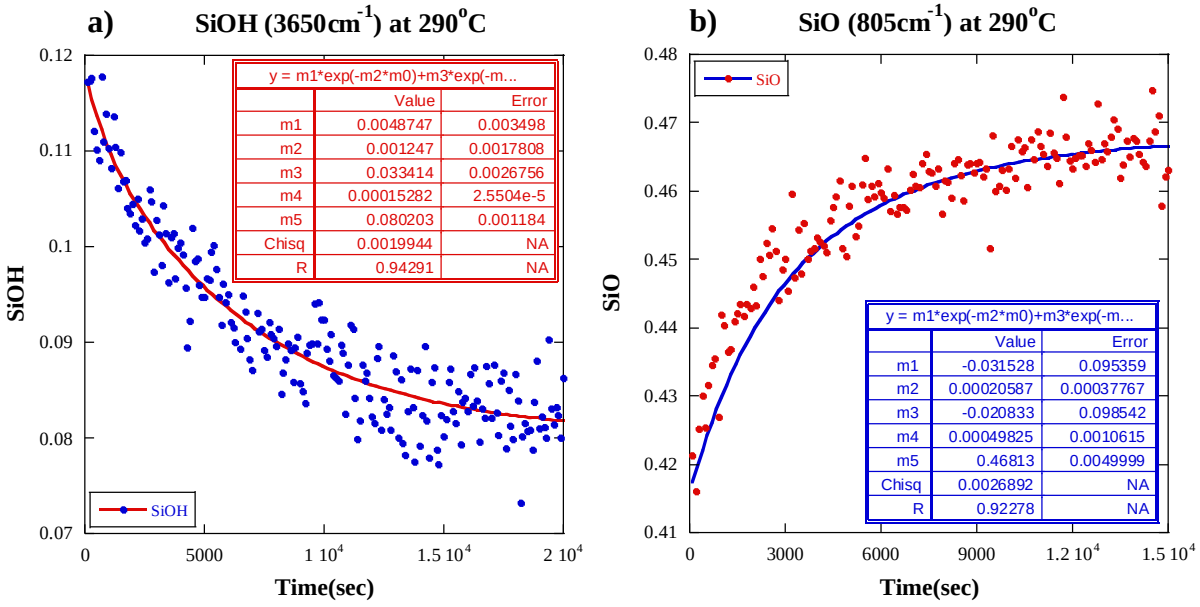

Fig.5.9. Results of curve fitting by two first order reactions (Abs = $C_1 exp(-k_1 t) + C_2 exp(-k_2 t) + C_3$), for changes with time in the peak heights of silica for (a) SiOH at 3650cm^{-1} and (b) SiO at 805cm^{-1} at 290ºC.

The fittings by the above two first order reaction equation of the experimental data for silica changes at 280^{o}C are shown in Fig.5.10. The fittings are rather well with correlation coefficient R of 0.9492 and 0.9953, suggesting the validity of the reaction model. Obtained first order rate constants for SiOH at 280ºC are k_1 = 1.6x 10^{-3} s^{-1} for the initial stage (fast) and k_2 = 2.1 x10^{-4} s^{-1} for the later stage (slow) (Fig.5.10a). The first order rate constants for SiO at 280ºC are obtained to be k_1 = 2.5 x10^{-4} s^{-1} for the initial stage (fast) and k_2 = 1.7 x10^{-4} s^{-1} for the later stage (slow) (Fig.5.10b). These two rate constants are different for the faster and slower reactions of silica (Table 5.1).

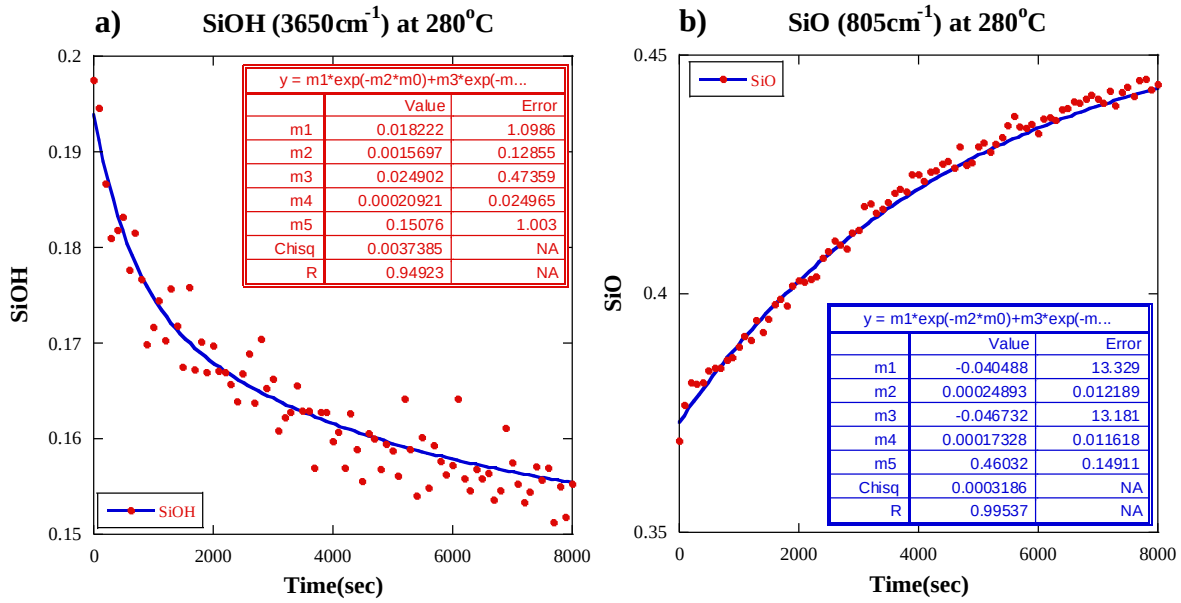

Fig.5.10. Results of curve fitting by two first order reactions (Abs = $C_1exp(-k_1t) + C_2exp(-k_2t) + C_3$), for changes with time in the peak heights of silica for (a) SiOH at 3650cm^{-1} and (b) SiO at 805cm^{-1} at 280ºC.

The fittings by the above two first order reaction equation of the experimental data for silica changes at 270^{o}C are shown in Fig.5.11. The fitting for SiOH is poor with correlation coefficient R of 0.7722 and very well for SiO with correlation coefficient R of 0.9986, suggesting the validity of the reaction model. Obtained first order rate constants for SiOH at 270ºC are k_1 = 7.3 x 10^{-4} s^{-1} for the initial stage (fast) and k_2 = 2.7 x10^{-4} s^{-1} for the later stage (slow) (Fig.5.11a). The first order rate constants for SiO at 270ºC are obtained to be k_1 = 9.7 x10^{-4} s^{-1} for the initial stage (fast) and k_2 = 1.2 x10^{-4} s^{-1} for the later stage (slow) (Fig.5.11b). These two rate constants are roughly in the same orders for the faster and slower reactions of silica (Table 5.1).

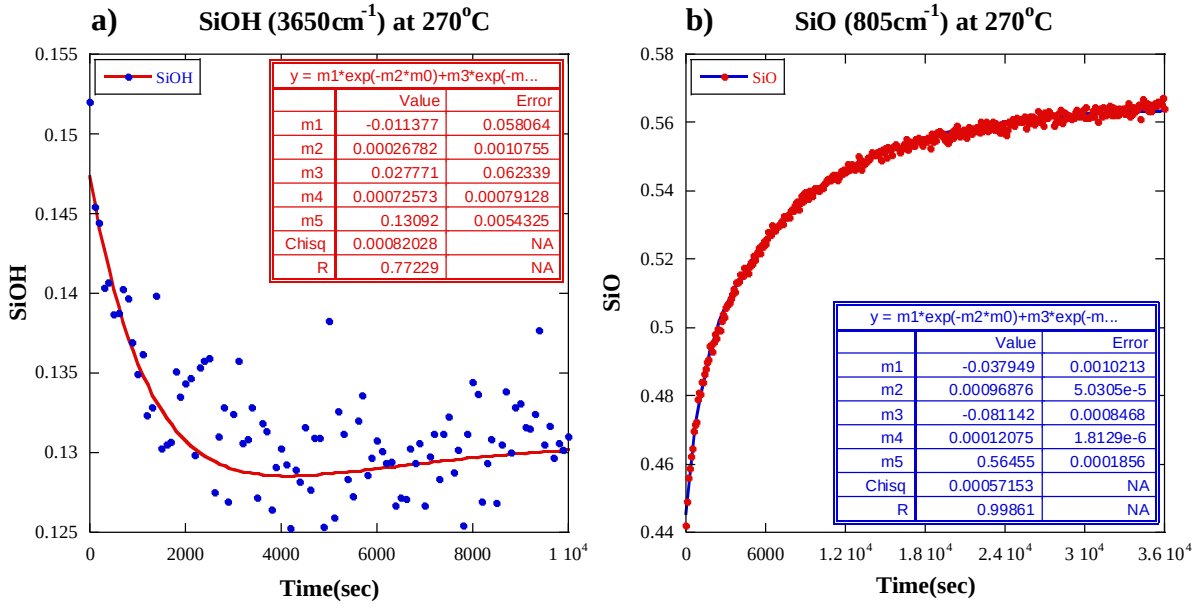

Fig.5.11. Results of curve fitting by two first order reactions (Abs = $C_1exp(-k_1t) + C_2exp(-k_2t) + C_3$), for changes with time in the peak heights of silica for (a) SiOH at 3650cm^{-1} and (b) SiO at 805cm^{-1} at 270ºC.

The fittings by the above two first order reaction equation of the experimental data for silica changes at 260^{o}C are shown in Fig.5.12. The fittings for SiOH are rather well with correlation coefficient R of 0.9112 and very well for SiO with correlation coefficient R of 0.9989, suggesting the validity of the reaction model. Obtained first order rate constants for SiOH at 260ºC are k_1 = 4.0 x10^{-4} s^{-1} for the initial stage (fast) and k_2 = 7.9 x10^{-5} s^{-1} for the later stage (slow) (Fig.5.11a). The first order rate constants for SiO at 260ºC are obtained to be k_1 = 1.6 x10^{-4} s^{-1} for the initial stage (fast) and k_2 = 3.5 x10^{-5} s^{-1} for the later stage (slow) (Fig.5.11b). These two rate constants are roughly in the same orders for the faster and slower reactions of silica (Table 5.1).

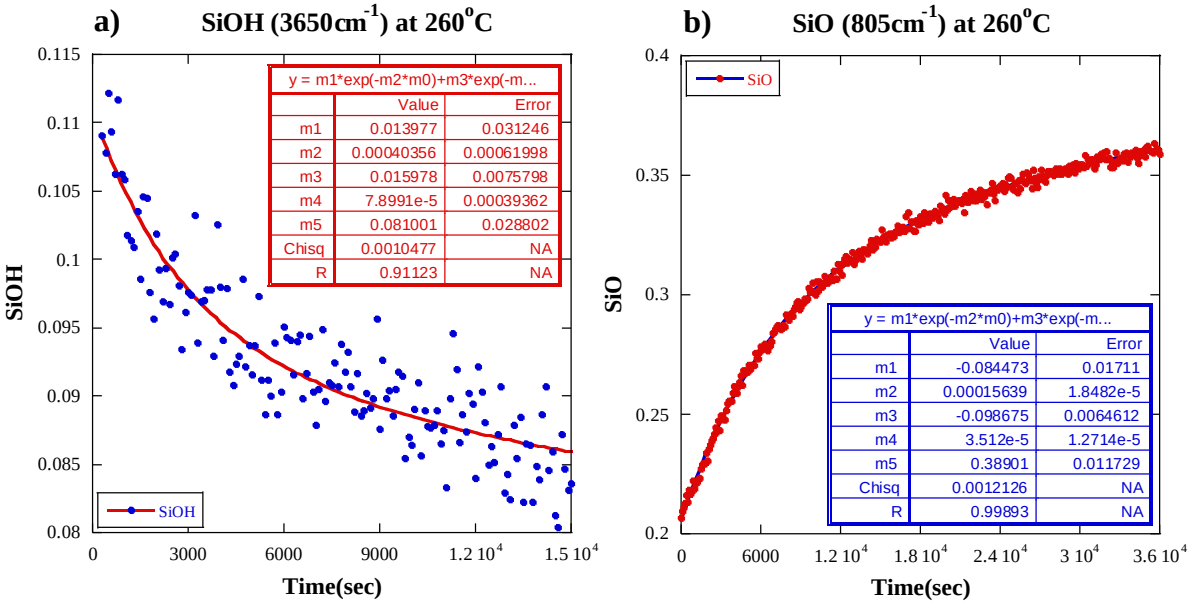

Fig.5.12. Results of curve fitting by two first order reactions (Abs = $C_1\exp(-k_1t) + C_2\exp(-k_2t) + C_3$), for changes with time in the peak heights of silica for (a) SiOH at 3650cm^{-1} and (b) SiO at 805cm^{-1} at 260ºC.

5.4.3. Temperature dependence of decrease rates of SiOH and Increase of SiO

Temperature dependence of reaction rates can be described by the Arrhenius equation:

$\ln(k)=\ln(A)-E_a/RT$

where k is the rate constant, A is the pre-exponential "frequency" factor, E_a is the activation energy, R is the gas constant (R= 8.314 J/mol.K) and T is the absolute temperature (K).

Obtained first order rate constants at different temperatures for SiOH and SiO, k_1 for the initial stage (fast) and k_2 for the later stage (slow) were plotted in Arrhenius diagrams in Fig.5.13a and Fig.5.13b, respectively.

The rate constants of k_1 for SiOH are larger than that for SiO at 290, 280 and 260°C (Fig.5.13a). Gradients of fitted lines of these data in Fig.5.13a give activation energies of

E_a~62 kJ/mol for k_1 of SiOH, and E_a~109 kJ/mol for k_1 of SiO in the temperature range from 300 to 260°C.

The rate constants of k_2 for SiOH are larger than those for SiO at 280, 270 and 260°C, but they are smaller than those of SiO at 300 and 290°C. Gradients of fitted lines of these data in Fig.5.13b give activation energies of E_a~16 kJ/mol for k_2 of SiOH, and E_a~ 117 kJ/mol for k_2 of SiO in the temperature range from 300 to 260°C.

These reaction rate constants and activation energies for SiOH and SiO bands of diatoms will be discussed in the summary and general discussion (chapter 6).

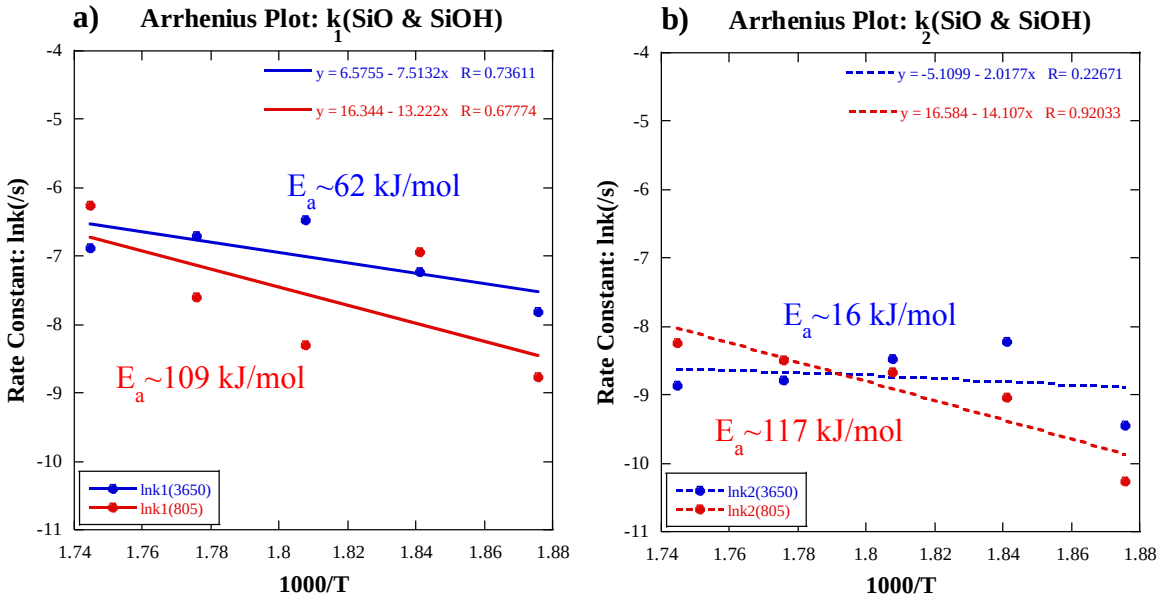

Fig.5.13. Arrhenius diagrams for the rate constants k as a function of temperature T (K) determined by two first order reactions for diatom heating experiments in Figs. 5.8 to 5.12. (a) k_1 for SiOH at 3650cm^{-1} and SiO at 805cm^{-1} in the temperature range of 300-260ºC. (b) k_2 for SiOH at 3650cm^{-1} and SiO at 805cm^{-1} in the temperature range of 300-260ºC.

Chapter 6. Summary and general discussion

6.1. Introduction

Diatoms are a large and ecologically important group of eukaryotic unicellular photosynthetic phytoplankton controlling the carbon cycle of the earth (Smetacek, 1985; Falkowski et al 1998; Wilkerson & Dugdale, 1998), which is an important origin of petroleum and natural gas as well (Aoyagi & Omokawa 1992; Aoyagi & Omokawa 1993, Theriot, 2012; Levitan et al 2014). The diatom cell wall is composed of mainly hydrous amorphous silica ($SiO_2.nH_2O$) with a small portion of organic macromolecules (proteins and polysaccharides) (Hecky et al, 1973; Kröger & Poulsen, 2008; Sumper & Brunner, 2008)(Fig.6.1).

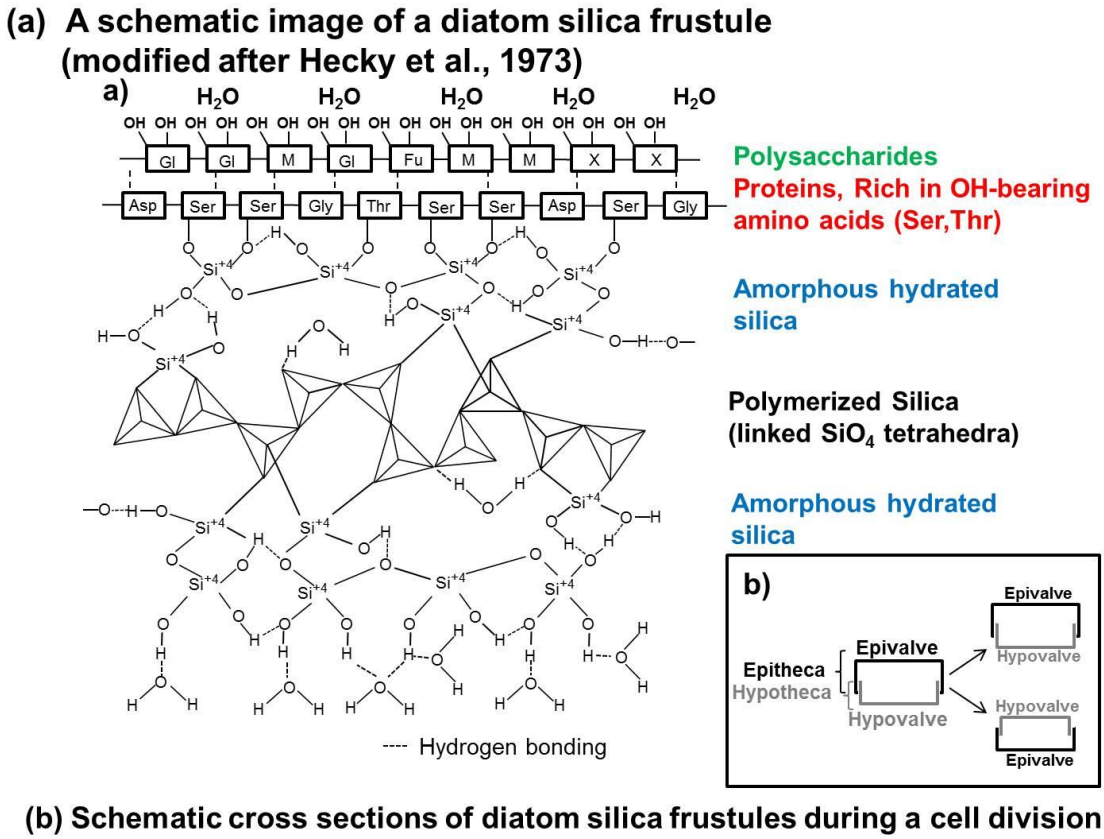

Fig.6.1. A schematic images of (a) chemical structure of diatom silica frustule and (b) cell division process.

Despite extensive studies of bulk chemical compositions, structures and properties of biominerals including diatoms, their formation processes (called biomineralization) are still poorly understood (Mann, 2001; Sumper, 2002; Kröger & Sumper, 2004; Mount et al 2004, Hildebrand, 2008, Tesson & Hildebrand, 2013). One of the main reasons is the lack of microscopic characterization of biominerals. In this research, first Infrared (IR) micro-spectroscopy and Scanning Electron Microscopy (SEM) has been applied to describe chemical and physical structures of present day centric diatoms (*Arachnoidiscus ornatus*) (Diameter: 100-350 µm) in micro-scales (chapter 2).

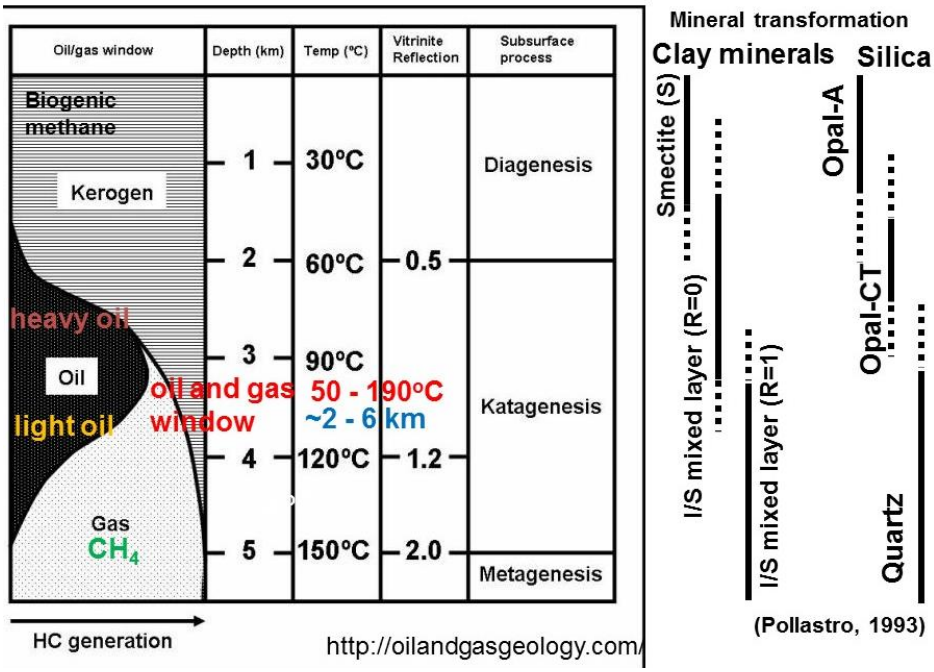

Fig.6.2. A schematic images of oil and gas generation during burial, diagenesis, catagenesis and metagenesis of sediments including biological debris such as diatoms. Transformations of clay minerals and silica are also indicated.

Dead bodies of marine diatoms are sedimented on the ocean floor and buried in marine sediments with time. During their burial, temperature and pressure increase and organic components in diatom bodies are transformed. Silica is also transformed from amorphous

hydrous silica (Opal-A) via cristobalite (Opal-C) to quartz (Qz) (Pollastro, 1993). These burial processes are subdivided into three phases: diagenesis, catagenesis and metagenesis (Berner, 1980; Tissot and Welt, 1984) (Fig.6.2).

Generation of hydrocarbons is considered to be related to transformation of organic components in aquatic organisms such as diatoms during the burial-diagenesis (Tissot and Welt, 1984). The depth of oil and gas generation is considered to be around 2 to 6 km corresponding to 50 to 190^{o}C, which is called as "oil and gas window" (Fig.6.2). This depth of oil and gas generation roughly corresponds to the reported depth of transformation of silica from opal CT (cristobalite) to quartz. However, the relation between silica transformation and hydrocarbon generation is not known. Evaluation of hydrocarbon generation potentials has been conducted often by using reaction kinetics of kerogen (complex sedimentary organic matter) to understand quality and quantity of petroleum and natural gas (Behar et al., 1997; Burnham et al., 1989; Dieckmann et al., 2000). Most of experimental simulations of hydrocarbon generation reactions have been conducted at high temperatures (500^{o}C -350^{o}C) resulting in wide ranges of rates and activation energies (Behar et al., 1997; Burnham et al., 1989; Dieckmann et al., 2000; Tonoue, PhD thesis 2015). These varying values give a very large range of time scales for hydrocarbon generation by their extrapolation to lower temperatures of 70^{o}C to 150^{o}C (natural hydrocarbon reservoir conditions).

Although some catalytic effects of minerals on rapid hydrocarbon generation have been suggested (Johns, 1979; Wei et al., 2006), few quantitative evaluations were reported. In particular, detailed kinetic studies of organic transformation processes during burial and diagenesis of diatomaceous sediments have not been simulated experimentally by using diatoms themselves as the source rock.

This research aims to clarify thermal transformation and kinetic parameters (reaction rate constants and activation energies) of diatom frustules as measured by in situ heating under a Fourier transform infrared (FTIR) spectrometer, based on the chemical and physical structures of the present day centric diatom frustules (*Arachnoidiscus ornatus*, Diameter:

100-350μm) that were studied mainly by Infrared (IR) micro-spectroscopy in Chapter 2. Transflection-mode FTIR spectroscopy was employed for measuring IR spectra of diatom frustules on Al plate in the heating stage. The objectives of this thesis are:

1) Since diatom silica frustules have abundant micro- and nano-pores, effects of voids on IR micro-spectroscopy have been evaluated. Also, the void area percentages of diatom frustules have been determined from SEM imaging. After careful evaluation of the void effects on diatom frustules, IR absorption peaks and their ratios have been determined for 43 diatom samples. IR microscopic imaging has been conducted by mapping the microscopic distribution of IR peak heights and ratios for 4 representative diatom samples. (Chapter 2)

2) Changes in aliphatic CH species during in-situ heating IR microspectroscopy of unwashed diatom frustules are analyzed to evaluate their decrease rates upon heating. (Chapter 3)

3) Changes in amide I and amide II during in-situ heating IR microspectroscopy of unwashed diatom frustules are analyzed to evaluate degradation rates of proteins upon heating. (Chapter 4)

4) Changes in silica during in-situ heating IR microspectroscopy of unwashed diatom frustules are analyzed to evaluate their transformation rates upon heating. (Chapter 5)

5) These thermal changes of aliphatic CH, amide and silica species in diatom frustules are compared and organic-silica interactions are discussed in relation to hydrocarbon generation. (Chapter 6)

6.2. Materials and methods

Centric diatoms (*Arachnoidiscus ornatus*) (Diameters: 100-350μm) were taken from red algae at Kurosakinohana, near Misakiguchi station, Miura Peninsula, Kanagawa Prefecture, Japan (May, 2009). For the microscopic characterization of diatom frustules

(chapter 2), they were washed first by H_2O_2 (about 30 wt%) to remove organics, then by HCl (about 4 mol/l) to dissolve carbonates and finally by deionized water. They are then mounted on a BaF_2 crystal, which is transparent in the 4000-700cm^{-1} region. 4 representative diatom samples were selected in this study among 43 samples: Samples A (Diameter: 177µm), B (300µm), C (310µm) and D (176µm). Infrared transmission micro-spectroscopy of washed diatom frustules was conducted by a Fourier transform IR (FT-IR) spectrometer (Jasco FTIR-620+IRT30) under the experimental conditions of 100 scans, 4cm^{-1} resolution, 4000-700cm^{-1} range and 50×50µm^2 aperture (Fig.6.3). High resolution IR mapping with a 6.25×6.25µm^2 pixel size has been performed by IR imaging microscope (Thermo Nicolet iN10MX) under the experimental conditions of 64 scans, 8cm^{-1} resolution and 4000-700cm^{-1} range. SEM images were obtained on the same samples on the BaF_2 crystal without carbon/metal coating under a low vacuum condition (about 50Pa, 5kV acceleration) by SU3500 Scanning Electron Microscope (Hitachi High-Technologies).

To conduct in situ isothermal heating experiments, diatom samples were not washed, but just dried in ambient air. To examine IR spectral changes, a single dried unwashed diatom particle was mounted on an Al plate without using any adhesive. The Al plate with mounted diatom was placed in a heating stage (Linkam TS-1500) and set under an IR microscope connected to a Fourier trans form IR spectrometer (FT-IR) (FTIR-620+IRT30, JASCO Co., Ltd) (Fig.6.3). The temperature of the sample was monitored just below the Al plate and increased at a rate of 50^{o}C/minute up to the desired temperature (260, 270, 280, 290 or 300°C). Since no window materials are set in the heating stage, the diatom sample was heated in an ambient air atmosphere. A background reflection spectrum on a 100×100µm^2 aperture area (avoiding the diatom free area) was first measured on a diatom free Al plate at room temperature by accumulating 100 scans with 4cm^{-1} resolution in the 4000-700cm^{-1} wavenumber range. First the sample transflection spectrum was measured on a diatom sample mounted on an Al plate at room temperature then at the desired temperature (260, 270, 280, 290 or 300°C), which was kept constant during the following IR spectral measurements. A series of IR transflection (transmission-reflection) spectra was measured on the same position of the diatom sample on the Al plate at every 100 seconds.

These transflection signals were divided by the above background spectrum on the diatom-free Al plate at room temperature.

6.3. IR spectra of diatom silica frustules and void effects associated with IR micro-spectroscopy.

A representative infrared (IR) spectrum of a washed diatom frustule and its band assignments is shown in Fig.6.3.

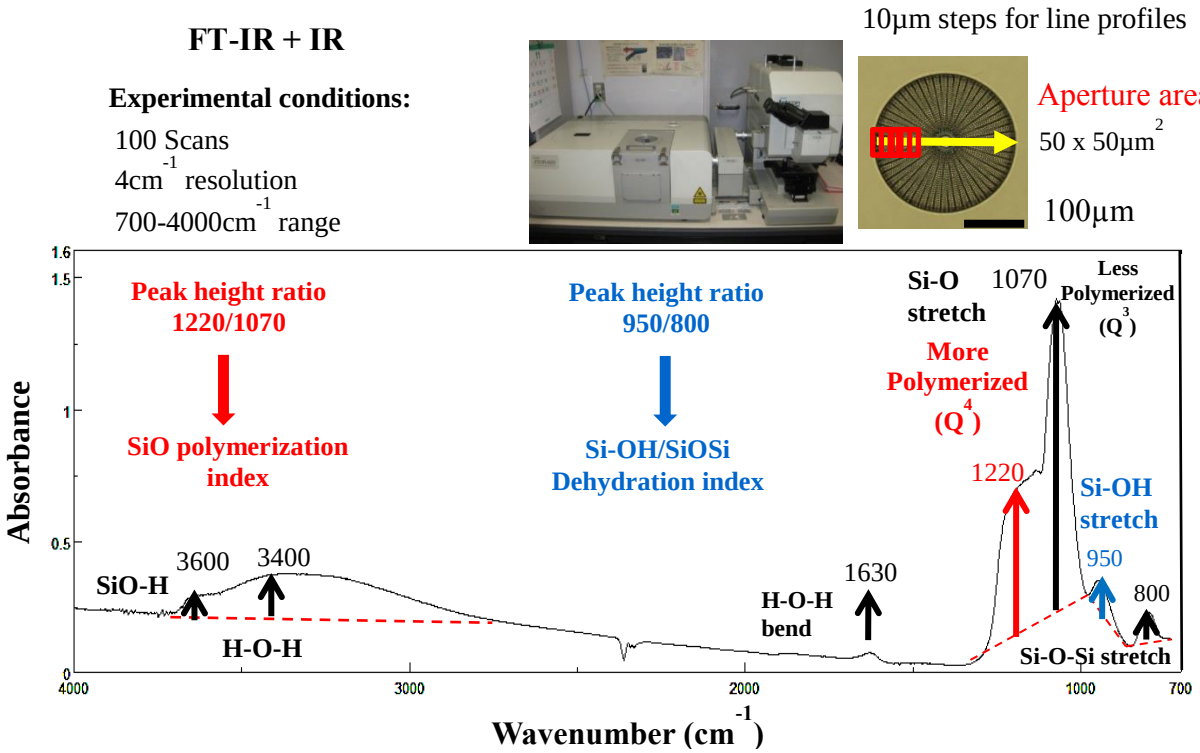

Fig.6.3. A typical IR spectrum of washed diatom silica frustule.

Diatom silica frustules have generally complex microscopic morphology including many void areas such as micro- or nano-pores. Therefore, effects of voids on the spectral band shapes were first evaluated (Fig.6.4). With increasing void area %, 1220cm^{-1}/1070cm^{-1} peak height ratio (Si-O polymerization index) increases and 950cm^{-1}/800cm^{-1} peak height ratio

(Si-OH/Si-O-Si) decreases, both approaching 1. Based on the void area% of representative diatom samples determined by SEM image analyses (51.5% to 20.5%) and spectral simulation, the 1220cm^{-1}/1070cm^{-1} ratios of diatom samples are sometimes affected by the void effect, but the 950cm^{-1}/800cm^{-1} ratios can indicate real structural information of silica. This void effect should be carefully evaluated for IR micro-spectroscopy of micro-nano-porous materials.

Maturity of diatom specimens may be evaluated from:

1) void area percentages determined by SEM,

2) average thicknesses determined by optical microscope and

3) average values of 1220cm^{-1}/1070cm^{-1} peak height ratios (opposite trend to the void effect) determined by IR micro-spectroscopy.

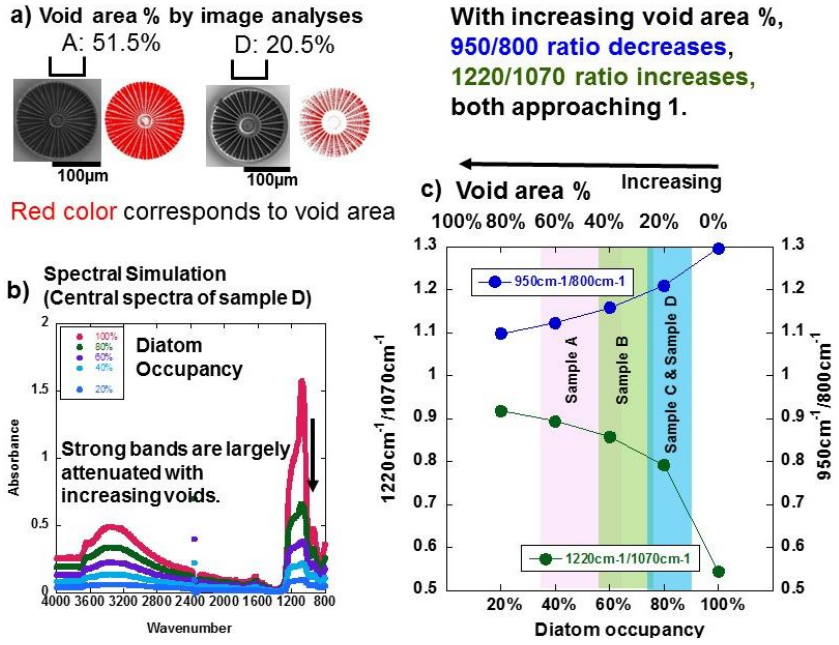

Fig.6.4. Void effects on IR spectra and peak height ratios of diatom silica frustules.

Microscopic heterogeneities of chemical structures of silica were obtained by IR micro-spectroscopic mapping of 4 representative diatoms. Regions with large 950cm^{-1}/800cm^{-1} ratios were found on some diatoms indicating hydrated amorphous immature silica. IR

micro-spectroscopic data with careful void effect evaluation can be applied to physicochemical structures of bionanomaterials such as diatoms.

6.4. In situ isothermal heating experiments by micro-FTIR spectroscopy

IR spectral changes with heating of unwashed diatoms on Al plates were studied by in-situ isothermal heating IR transflection micro-spectroscopy.

In the IR transflection micro-spectroscopy on diatom silica frustules, 1200-1000cm^{-1} bands (Si-O stretching) are severely distorted because of reflection at the very absorbing wavenumber (Fig.6.5). However, the higher wavenumber regions such as aliphatic CHs and amides are less affected by strong reflections. Moreover, in order to avoid the void effect (Fig.6.4), 100×100μm^2 aperture area was set within the diatom sample.

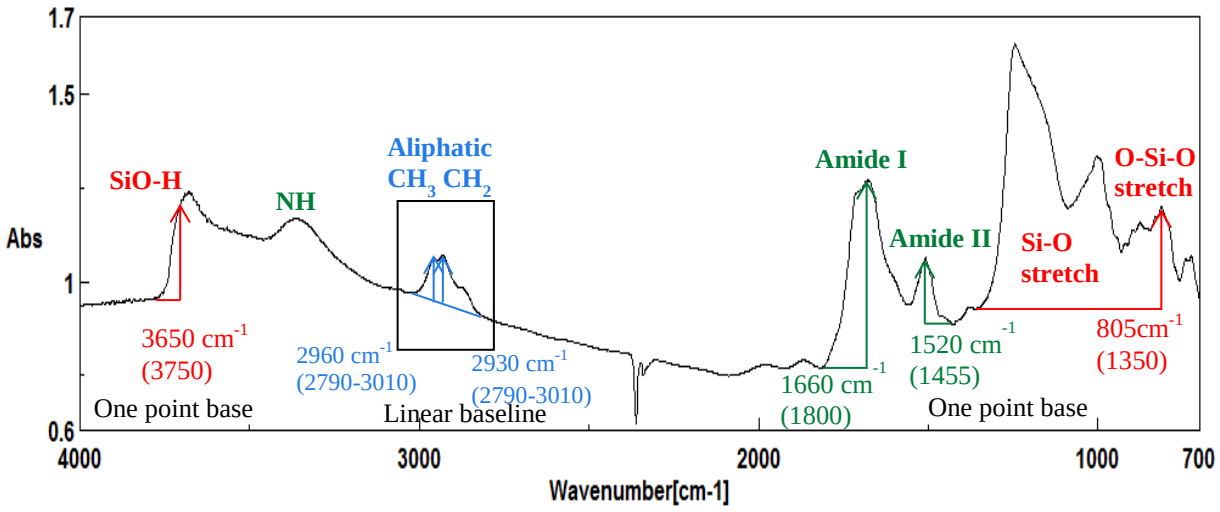

Fig. 6.5. A representative IR Spectrum of an unwashed diatom silica frustule at room temperature (26°C).

Diatom IR spectra were collected as absorbance (Abs), which can be written by the Lambert-Beer law as:

$$\mathrm{Abs} = -\log_{10}\left[\frac{I_1}{I_0}\right]$$

where I_0 is the intensity of the incident beam (background spectrum), and I_1 is the infrared signal intensity of the sample. In the transflection signal of a diatom sample, IR light transmitted through the diatom is reflected at the Al plate and transmitted again through the diatom, so the IR lights are travelling about twice the thickness of the diatom sample.
A representative Infrared (IR) transflection spectrum of an unwashed diatom at room temperature (26°C) is shown in Fig.6.5. All the absorption bands in transflection mode in the 4000-700cm^{-1} wavenumber region are similar to those of transmission mode (Fig.6.3) with the exception of Si-O stretching bands (1240 and 1030cm^{-1} bands due to stretching of SiO-H and Si-OH bonds, respectively) which are distorted at around 1300-1000cm^{-1} wavenumber region.

IR spectral changes with time during heating experiments of diatoms on Al plates under ambient atmospheric condition at 300, 290, 280, 270 and 260ºC are similar at all temperatures but on different time scales, indicating decreases of organic functional groups (peak heights of aliphatic CHs (2960 and 2930cm^{-1}), amide I (1660cm^{-1}) and amide II (1520cm^{-1})). However, while SiOH band (3650cm^{-1}) decreased upon heating, SiOSi band around 805cm^{-1} increases with heating due possibly to silica transformation.

The in-situ heating IR micro-spectroscopic results were analyzed by chemical reaction kinetics to determine reaction rates of decrease of main chemical components in diatoms. By assuming the two first order reaction model, the decrease trends for aliphatic CH_2, CH_3, amide I, amide II, SiOH and the increase trend of SiOSi have been fitted by the following two exponential fitting equation for each temperature, to obtain reaction rate constants k_1 and k_2:

$$Abs = C_1 \exp(-k_1 t) + C_2 \exp(-k_2 t) + C_3$$

6.4.1. Changes in aliphatic CHs of diatoms during isothermal heating experiments

In order to quantitatively examine decrease trends of aliphatic CH_2 (2930cm^{-1}) and CH_3 (2960cm^{-1}) bands, a linear baseline between 2790 and 3010cm^{-1} was applied to determine their peak heights (Fig.6.5). Changes with time in the peak heights of aliphatic CH_2 at 2930cm^{-1} and CH_3 at 2960cm^{-1} at 260 to 300ºC are shown in Fig. 6.6. The peak heights are divided by those at time zero (starting of the isothermal heating). The decrease trends of aliphatic CHs are similar for all the temperatures, and appear to be faster at higher temperatures.

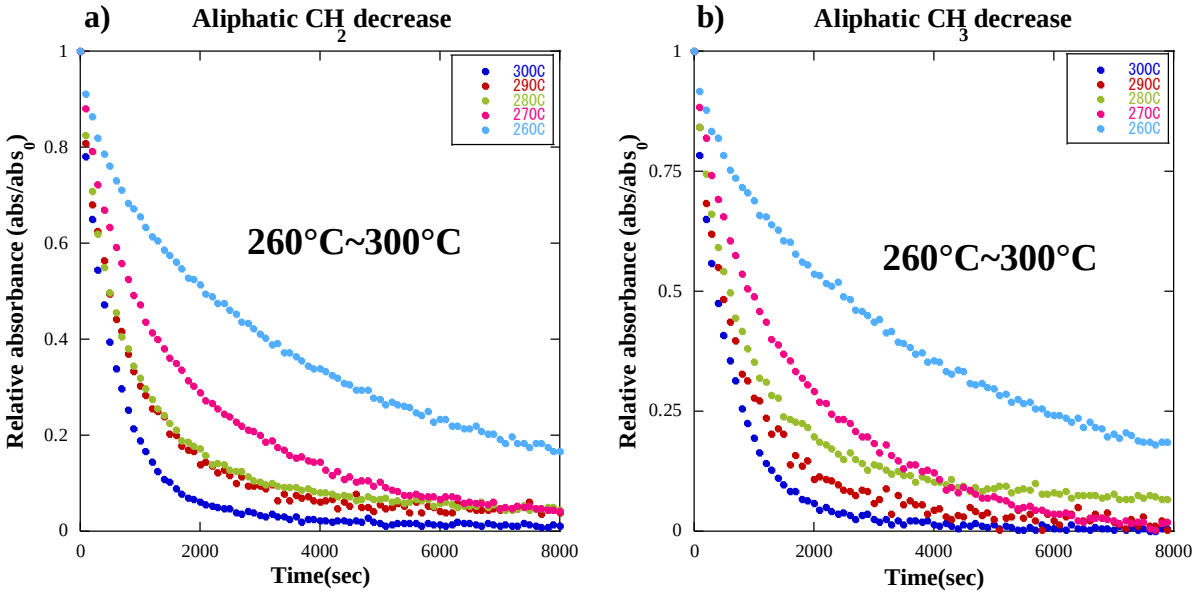

Fig.6.6. Changes with time in the peak heights of aliphatic CHs for (a) CH_2 at 2930cm^{-1} and (b) CH_3 at 2960cm^{-1} at 260, 270, 280, 290 and 300ºC.

The fittings by the above two first order reaction equation of the experimental data at 300, 290, 280, 270 and 260ºC for aliphatic CH decreases gave two first order rate constants: 1) the initial fast decrease and 2) the later slow decrease.

The CH_3/CH_2 ratio can be used to evaluate reaction mechanisms of aliphatic CH decreases (Fig.6.7). The CH_3/CH_2 ratios show an increasing trend at 280ºC and at the initial

stage of 260°C. On the other hand, they show decreasing trends for 300, 290 and 270°C. The increase in the CH_3/CH_2 ratio can indicate breaking of longer aliphatic CH_2 chains and forming more end-methyls (– CH_3). The CH_3/CH_2 decreases at higher temperatures might be due to secondary recombination reactions of broken short chains to produce longer chains of aliphatic CHs.

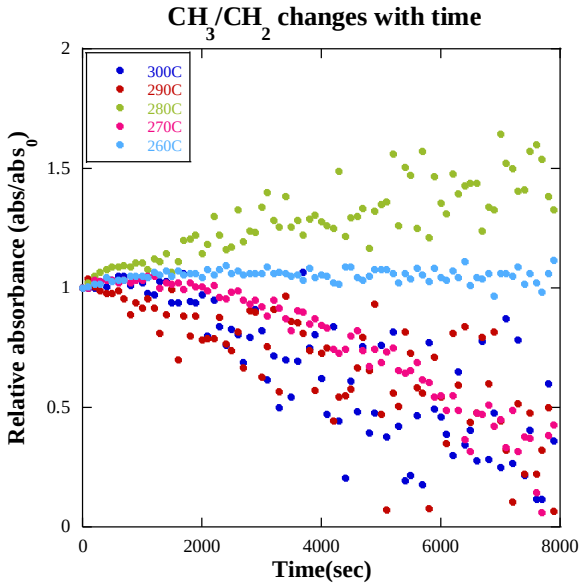

Fig.6.7. Changes with time in peak height ratios of CH_3/CH_2 at 300, 290, 280, 270 and 260°C.

Obtained first order rate constants at different temperatures for aliphatic CH_2 and CH_3, k_1 for the initial stage (fast) and k_2 for the later stage (slow), were plotted in Arrhenius diagrams to show the temperature dependence of reaction rates (Fig.6.8). Activation energies of these two reactions are 123 and 128 kJ/mol for k_1 and k_2 of CH_2 and 158 and 135 kJ/mol for k_1 and k_2 of CH_3, respectively, at the temperature range from 300 to 260°C.

The rate constants of the faster process k_1 of aliphatic CH_2 and CH_3 showed larger gradients for higher temperatures (300-280°C) and smaller gradients for lower temperatures (280-260°C). The rate constants fitted by two different lines for different temperature regions give activation energies of E_a~170 kJ/mol, for CH_2 and E_a~257 kJ/mol

for CH_3 (k_1: 300-280°C) and E_a~77 kJ/mol for CH_2 and E_a~62kJ/mol for CH_3 (k_1: 280-260°C) (Fig.6.8a). The activation energies are larger at higher temperatures and smaller at lower temperatures.

The activation energies for k_2 are E_a~97 kJ/mol for CH_2 and E_a~124 kJ/mol for CH_3 (k_2: 300-280°C) and E_a~167 kJ/mol for CH_2 and E_a~134 kJ/mol for CH_3 (k_2: 280-260°C) (Fig.6.8b). They are roughly around 130 kJ/mol at 300-260°C.

These activation energies for aliphatic CH decrease from diatom frustules (62–257 kJ/mol) are generally much smaller than the reported values for hydrocarbon generation from kerogens of 200-270 kJ/mol, (Behar et al., 1997; Burnham et al., 1989; Dieckmann et al., 2000) which seems to be controlled by cracking of alkyl-alkyl C-C bonds and aryl-alkyl C-C bonds at high temperatures (350-450°C). The E_a value around 257 kJ/mol for k_1 of CH_3 decrease at 300-280°C might be close to these literature values.

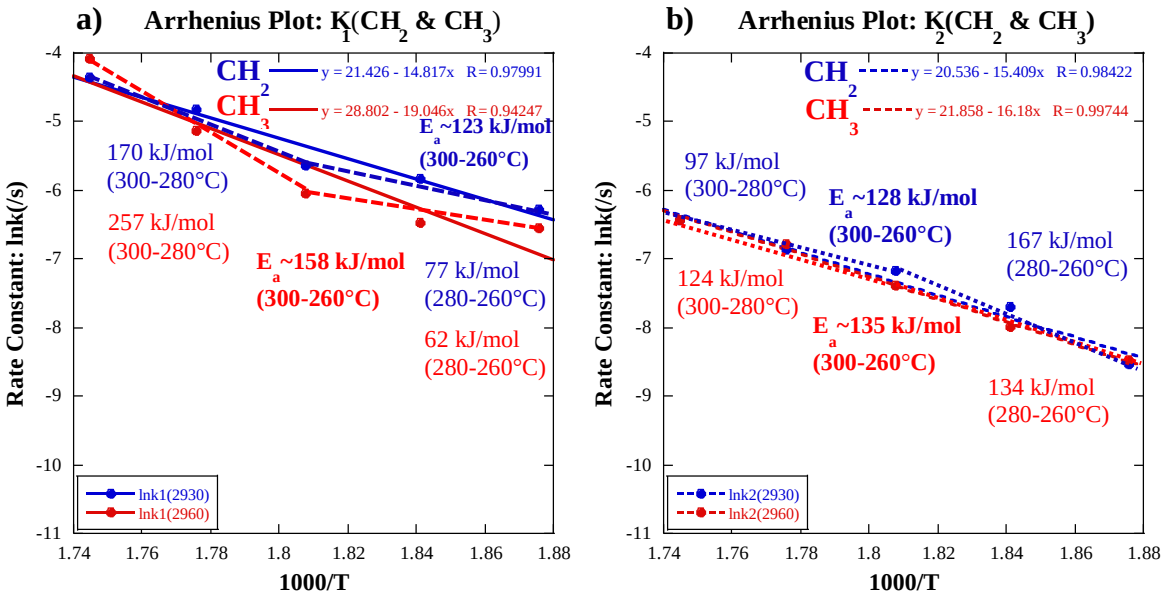

Fig.6.8. Arrhenius diagrams for the rate constants k as a function of temperature T (K) determined by two first order reactions for diatom heating experiments. a) k_1 of CH_2 at 2930cm^{-1} and CH_3 at 2960cm^{-1} in the temperature range of 300-260ºC, 300-280ºC and 280-260ºC. b) k_2 of CH_2 at 2930cm^{-1} and CH_3 at 2960cm^{-1} in the temperature range of 300-260ºC, 300-280ºC and 280-260ºC.

6.4.2. Changes in amide I and amide II of diatom frustules during isothermal heating experiments

Changes with time in amide I and II peak heights of proteins in diatom frustules during the heating experiments of unwashed diatom frustules under ambient atmospheric condition at 300, 290, 280, 270 and 260ºC were analyzed by taking two different one point baselines at 1850cm^{-1} for amide I (1660cm^{-1}) and 1455cm^{-1} for amide II (1520cm^{-1}) (Fig. 6.9). The peak heights are divided by those at time zero. The decrease trends of amide I and amide II are similar for all the temperatures but appear to be faster at higher temperatures.

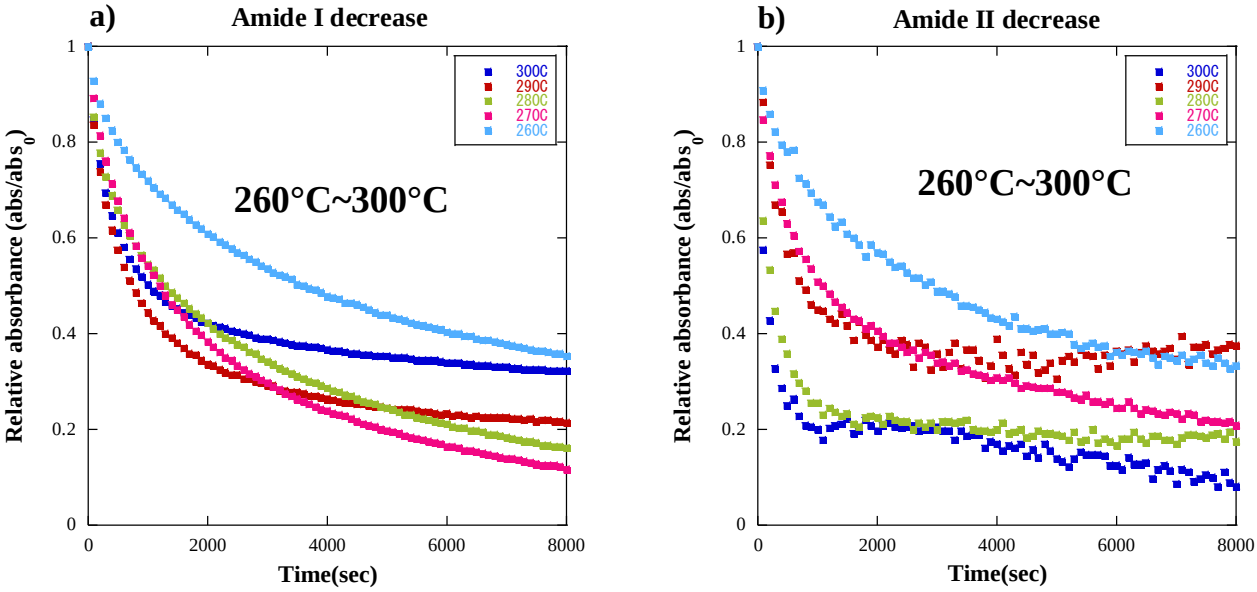

Fig.6.9. Changes with time in the peak heights of amide I and amide II.
(a) amide I at 1660cm^{-1} and (b) amide II at 1520cm^{-1} at 260, 270, 280, 290 and 300ºC.

The fittings of these data for amide I and amide II decreases by the two first order reaction equation give two first order rate constants: 1) the initial fast decrease and 2) the later slow decrease. They are plotted in Arrhenius diagrams (Fig. 6.10). Activation energies at 300-260^{o}C for k_1 of amide I and amide II are 120 and 123 kJ/mol, respectively, and 126 and 62 kJ/mol for k_2 of amide I and amide II, respectively. These activation energies around 120

kJ/mol are generally comparable to those for decomposition of amino acids (147 kJ/mol: Shiota and Nakashima, 2005; ~120 kJ/mol: Tomiak et al., 2013).

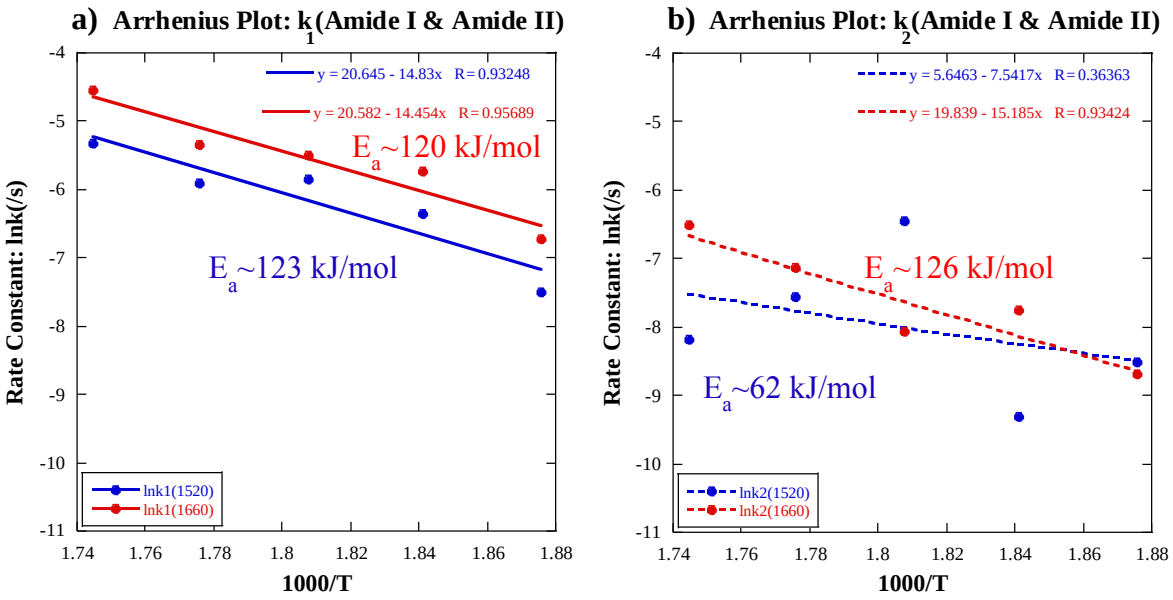

Fig.6.10. Arrhenius diagrams for the rate constants k as a function of temperature T (K) determined by two first order reactions for diatom heating experiments at 300-260ºC.
(a) k_1 for amide I at 1660cm^{-1} and amide II at 1520cm^{-1}.
(b) k_2 for amide I at 1660cm^{-1} and amide II at 1520cm^{-1}.

6.4.3. Changes in silica during in-situ heating IR microspectroscopy of unwashed diatoms

Representative IR spectral changes with time during heating experiments of unwashed diatom frustules on Al plates under ambient atmospheric condition at 300, 290, 280, 270 and 260ºC for silica bands are shown in Fig. 6.11.

The SiO-H band was around 3650cm^{-1} at room temperature but shifted to higher wavenumber region around 3680cm^{-1} at higher temperatures (300-260^{o}C). This shift with temperature was already reported and considered to be due to decrease of hydrogen bonding leading to more isolated surface Si-OH species (Yamagishi et al., 1997). The peak

heights at 3650cm^{-1} with one point base at 3750cm^{-1} (the stable minima) decreased gradually during heating is suggesting dehydration.

The bands around 1000 to 750cm^{-1} including Si-OH (960cm^{-1}) and SiOSi (805cm^{-1}) bands changed greatly with heating possibly due to silica transformation (Fig. 6.11).

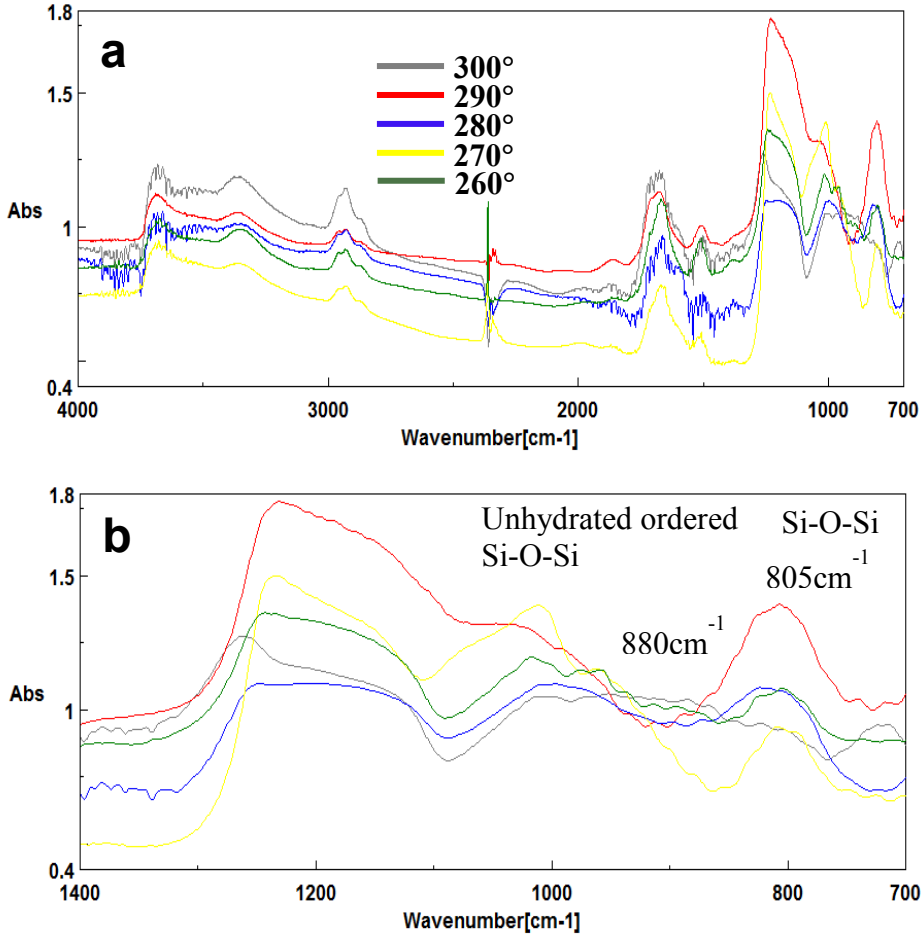

Fig. 6.11. Changes of IR spectra on unwashed diatom frustules with temperature. (a) Starting spectrum (time zero) at each temperature, (b) Details of silica bands (1400-700cm^{-1}) with distortion of SiO bands around 1300-1000cm^{-1}, bands around 880 cm^{-1} (Unhydrated ordered Si-O-Si) and 805 cm^{-1} (Si-O-Si streching).

The Si-OH (960cm^{-1}) bands are not clear already at the starting of the isothermal heating experiments, so their decrease behavior was not analyzed. The Si-O-Si stretching band at

room temperature was at around 805cm^{-1} and showed an increase at higher temperatures, but another band around 880cm^{-1} also increased except for 290^{o}C (Fig. 6.11). The 880cm^{-1} band was reported in dehydroxylation of silica particles (Grabbe et al., 1995; Ceresoli et al., 2000) and assigned to unhydrated ordered Si-O-Si structures (Liu and Shen, 2008). The peak heights at 805cm^{-1} with one point base at 1350cm^{-1} (the most stable point) increased gradually at 300-260ºC.

The decrease trends of SiO-H at 3650cm^{-1} and the increase trends of SiOSi at 805cm^{-1} are shown in Fig. 6.12. The SiO-H decreased and SiOSi increased gradually at 300-260ºC.

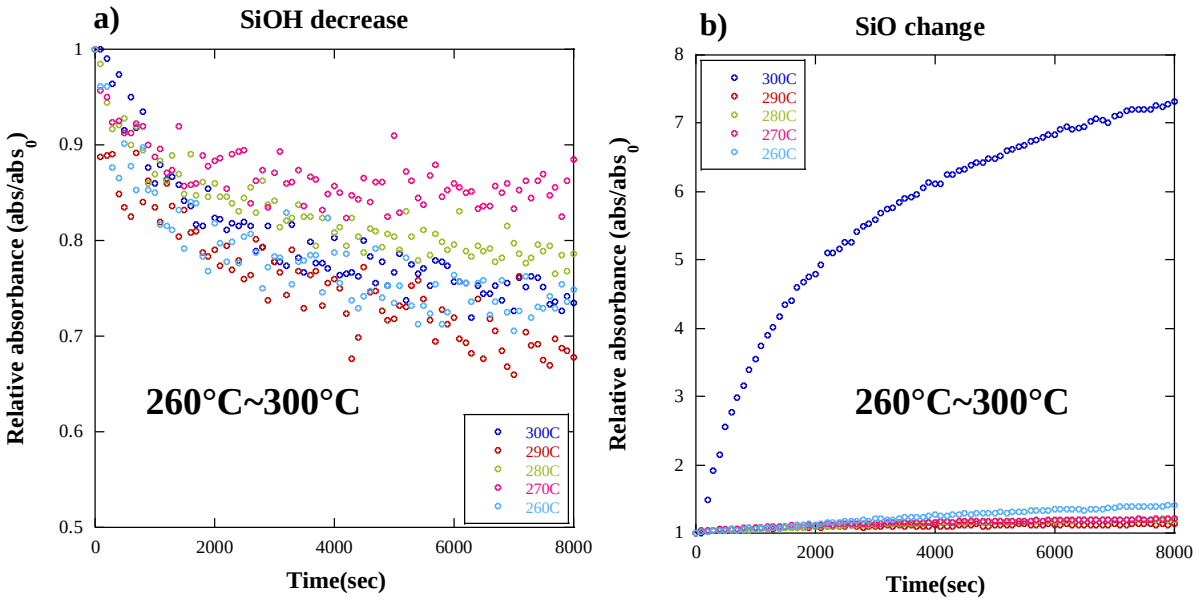

Fig.6.12. Changes with time in the peak heights of silica.
(a) SiOH at 3650cm^{-1} and (b) SiOSi at 805cm^{-1} at 260, 270, 280, 290 and 300ºC.

These changes with time of SiOH (3650cm^{-1}) and SiOSi (805cm^{-1}) peaks were fitted by the two first order rate equation to obtain rate constants. They are plotted in Arrhenius diagrams in the temperature range from 300 to 260^{o}C to give activation energies for k_1 of SiOH and SiOSi of 62 and 109 kJ/mol, respectively and those for k_2 of SiOH and SiOSi of

16 and 117 kJ/mol, respectively (Fig. 6.13). Since the rate constants do not show good linear trends, these activation energy values include large errors.

The k_1 of SiOH decrease showed a relatively linear trend with E_a value of 62 kJ/mol (Fig. 6.13). This might be comparable to the reported values of the transformation of amorphous silica (70 kJ/mol; Mizutani, 1977). Although details are not reported in literature, the increase of SiOSi (805cm^{-1}) peak can be related to crystallization of quartz-like phases (Saikia et al., 2008). The k_1 and k_2 of SiOSi increase have E_a values around 110 kJ/mol (Fig. 6.13). These might be comparable to the reported value for the transformation of cristobalite to quartz (95 kJ/mol; Ernst and Calvert, 1969).

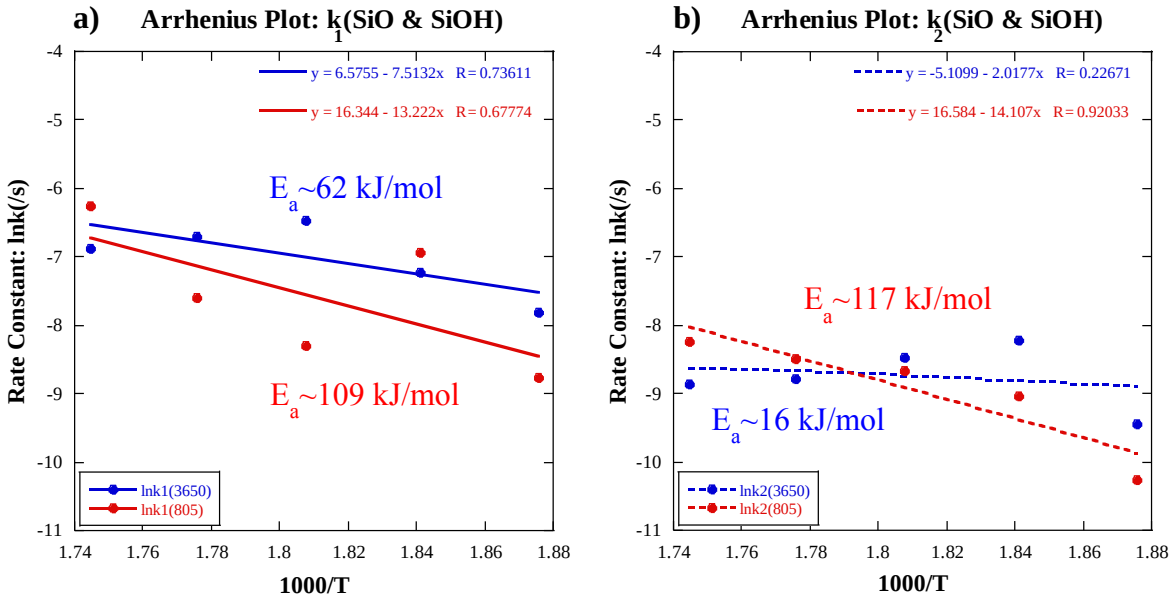

Fig.6.13. Arrhenius diagrams for the rate constants k as a function of temperature T (K) determined by the two first order reaction equation for diatom heating experiments at 300-260ºC.
(a) k_1 for SiOH at 3650cm^{-1} and SiOSi at 805cm^{-1}.
(b) k_2 for SiOH at 3650cm^{-1} and SiOSi at 805cm^{-1}.

6.5. Comparison of changes in aliphatic CHs, amides and silica during in-situ heating IR microspectroscopy of unwashed diatom frustules

The reaction rate constants determined above for aliphatic CHs, amides and silica during the in-situ heating IR micro-spectroscopy of unwashed diatom frustules are summarized in Fig. 6.14. Their activation energy values are also summarized in Table 6.1.

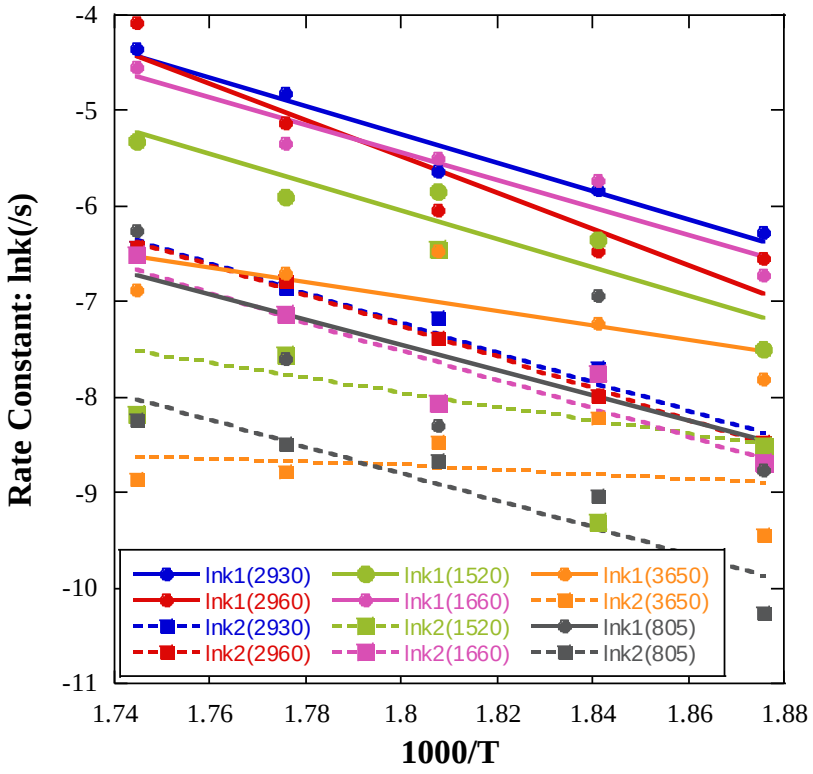

Fig. 6.14. Arrhenius diagram for the rate constants k as a function of temperature T (K) at 300-260°C determined by two first order reaction equations for heating experiments of unwashed diatom frustules for aliphatic CHs, amides and silica.

The decrease rates of the initial fast decrease (k_1) for aliphatic CHs are similar to those for amide I but larger than those of amide II (Fig.6.14). The decrease rates of the later slow decrease (k_2) for aliphatic CHs are similar to those for amide I but larger than those of amide II. The activation energy values for the decreases of aliphatic CHs and amides are

around 120 kJ/mol (Table 6.1). Therefore, these two processes might be related, in particular decreases of aliphatic CH_2 and amide I because of their similar rates.

The dehydration rates k_1 and k_2 for SiO-H are much smaller than the above decrease rates of aliphatic CHs and amides with smaller activation energies (Fig. 6.14, Table 6.1). Therefore, the dehydration of SiO-H might be independent from the degradation of aliphatic CHs and proteins.

The SiOSi increase rates k_1 and k_2 are also smaller than the above decrease rates of aliphatic CHs and amides but the faster rates k_1 are similar to the slower decrease rates of aliphatic CHs and amide I with smaller activation energies (Fig. 6.14, Table 6.1). The silica transformation can then be related to slower degradation processes of aliphatic CHs and proteins.

	300-280°C Initial fast: k_1	280-260°C Initial fast: k_1	300-260°C Initial fast: k_1	300-280°C Later slow: k_2	280-260°C Later slow: k_2	300-260°C Later slow: k_2
CH_2	170	77	123	96	167	128
CH_3	257	62	158	124	134	135
Amide I			120			126
Amide II			123			62
SiOH			62			16
SiOSi			109			117

Table 6.1. Summary of the activation energy values for aliphatic CH_2 , CH_3 , amide I , amide II, SiO-H and SiOSi (initial fast: k_1, later slow: k_2) at temperatures ranges of 300-280ºC, 280-260ºC and 300-260ºC.

These results suggest possible interactions of the followings during the heating of diatom frustules:

1) decreases of aliphatic CH_2 and amide I

2) silica transformation (SiOSi increase) and slower decrease rates of aliphatic CHs and amide I.

The same in-situ heating IR micro-spectroscopy was also conducted on degradation of cyanobacteria without and with silica-embedding (Igisu et al, submitted) (Fig. 6.15). The obtained CH decrease rates are much smaller than those for diatom frustules with slightly smaller activation energies (102 and 78 kJ/mol for CH_2 decrease of cynobacteria without and with silica-embedding).

Decrease rates for labile and refractory CH of coal at 350-420^{o}C with the same in-situ heating IR micro-spectroscopy but with N_2 gas flow (Tonoue, 2015: PhD Thesis), are much smaller than the present data for diatom frustules with larger activation energies (170 and 154 kJ/mol) (Fig. 6.15).

Although aliphatic CH decreases in diatom frustules are much faster than those of cyanobacteria and coal, they are substantially slower than hydrothermal decomposition of amino acids (Shiota and Nakashima, 2005) (Fig. 6.15). Therefore, although detailed reaction mechanisms are not known, these results again suggest the possible interactions between aliphatic CHs and proteins during the heating of diatom frustules.

Since diatoms are considered to be one of major sources of aliphatic hydrocarbons, it is necessary to compare the present results on aliphatic CH decrease rates from diatom frustules with those of kerogens. Activation energies for hydrocarbon generation are reported to be 170-370 kJ/mol (Behar et al., 1997; Burnham et al., 1989; Dieckmann et al., 2000) (Fig.6.16), and they are considered to be related to cracking of alkyl-alkyl C-C bonds and aryl-alkyl C-C bonds. Decrease rates for labile and refractory CH of coal at 350- 420^{o}C by in-situ heating IR micro-spectroscopy with N_2 gas flow (Tonoue, 2015: PhD Thesis) have similar rate constants with the lowest activation energy values (170 and 154 kJ/mol) (Fig. 6.16). Despite the possible large errors, these smaller activation energies are considered to be related to the presence of polar components such as N, S and O in the degradation of alkyl aromatics (Tonoue, 2015: PhD Thesis).

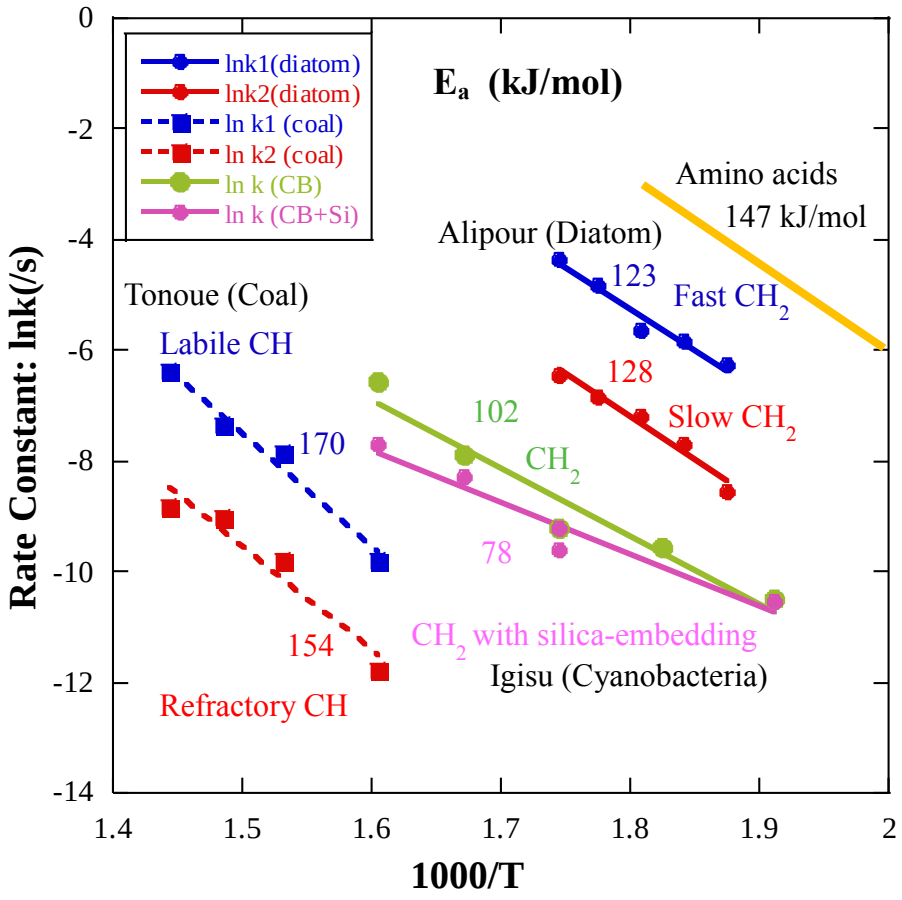

Fig.6.15. Comparison of activation energies and rate constants of first order reactions (k_1) of aliphatic CHs obtained from diatoms (this study), coal (Tonoue, 2015) and cyanobacteria (Igisu et al., 2015: submitted) together with hydrothermal decomposition rates of amino acids (Shiota and Nakashima, 2005).

Although the present in-situ heating IR micro-spectroscopy of diatom frustules was under air, the decrease rates for aliphatic CHs of diatom frustules are much larger than the above hydrocarbon generation reactions. I also tried to conduct the same experiments under N_2 flow but they were not possible with the frequent sample moving. However, some successful results suggested that the decrease rates of aliphatic CHs under N_2 flow are about only one order of magnitude smaller than those under air. Therefore, the present decrease reactions of aliphatic CHs from diatom frustules might be quite different from hydrocarbon generation reactions from kerogens, which are generally considered to be very slow in the natural oil and gas reservoir conditions (Fig .6.15).

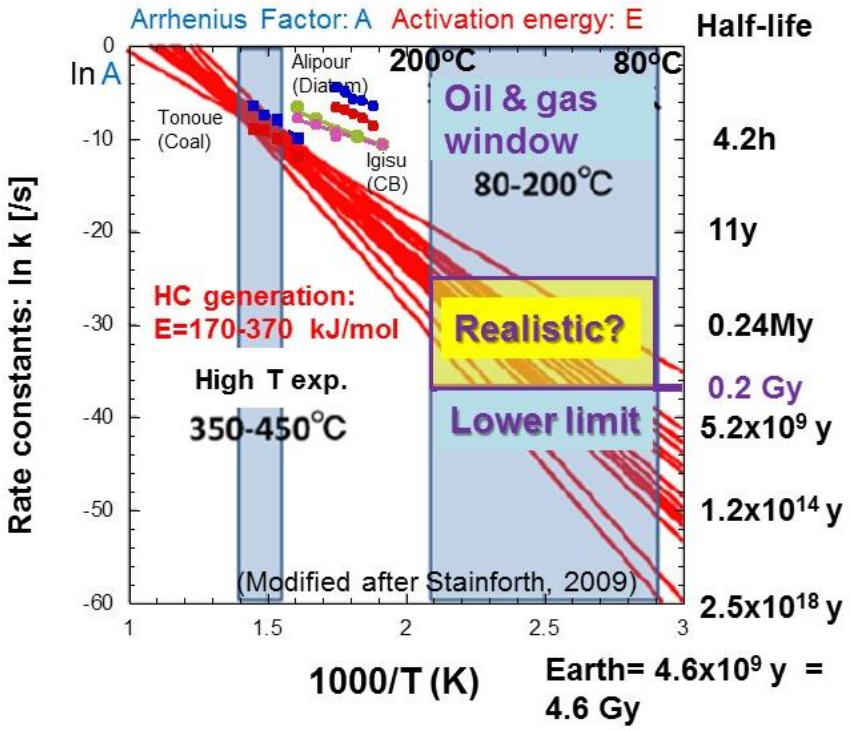

Fig.6.16. Arrhenius diagram comparing first order rate constants and activation energies of aliphatic CHs obtained from diatoms (this study), coal (Tonoue, 2015) and cyanobacteria (Igisu et al., submitted) together with literature data on hydrocarbon generation modified after Stainforth (2009).

Obtained results suggest that organic transformation reactions including protein degradation and generation of aliphatic hydrocarbons inside the diatom silica frustules might be different from those of proteins and/or kerogens separated from the biological structures. Although further studies are needed, importance of organic-inorganic interactions should be noted during the burial-diagenesis of diatom frustules.

6.6. Problems and future perspectives

The present study on diatom frustules shows that IR micro-spectroscopy is a useful method for characterizing small bio-nanomaterials and complex organic-inorganic interactions during their burial-diagenesis. However, the following problems remain to be solved:

1) The bonding natures among hydrous amorphous silica ($SiO_2.nH_2O$), lipids, proteins and polysaccharides in diatom cell walls (Fig. 6.1).
2) Relations among the dehydration of SiOH, the linkage of Si-O-Si and crystallization of cristobalite to quartz during the silica transformation during burial-diagenesis (Fig.6.2).
3) Origins of aliphatic CHs in diatom frustules and their relations to hydrocarbon generation.
4) Differences of decreases of amide I and amide II bands.

In order to solve some of these problems, the following studies can be conducted in the future:
1) Developments of high resolution IR/Raman micro-spectroscopy for characterizing bonding natures among hydrous amorphous silica ($SiO_2.nH_2O$), lipids, proteins and polysaccharides in diatom cell walls.
2) Improvements of in-situ heating IR micro-spectroscopy, especially under N_2 gas flow, for avoiding sample movement and increasing signal to noise ratio to obtain more accurate kinetic data sets.
3) In-situ heating IR micro-spectroscopy on amorphous silica gel for simulating the silica transformation without organic matrix.
4) In-situ heating IR micro-spectroscopy on proteins for simulating their degradation without silica matrix.
5) In-situ heating IR micro-spectroscopy on lipids for simulating their degradation without silica matrix.
6) In-situ heating IR micro-spectroscopy on polysaccharides for simulating their degradation without silica matrix.

7) Hydrothermal reactions of diatom frustules simulating their burial-diagenesis in the presence of water.

References

Aoyagi, K., and Omokawa, M., 1992. “Neogene Diatoms as the Important Source of Petroleum in Japan”. Journal of Petroleum Science and Engineering. 7(3):247-262

Aoyagi, K., and Omokawa, M., 1993. “Diagenesis of Neogene Diatoms and their Importance as a Source of Petroleum in Japan”. The Island Arc. 2(4): 273-279.

Asada, R., Okuno, M., and Tazaki, K., 2002. “Structural anisotropy of biogenic silica in pennate diatoms under Fourier transform polarized infrared microspectroscopy”. Journal of Mineralogical and Petrological Sciences. 97: 219-226.

Bassan, P., Sachdeva, A., Kohler, A., Hughes, C., Henderson, A., Boyle, J., Shanks, J.H., Brown, M., Clarke, N.W., and Gardner, P., 2012. “FTIR microscopy of biological cells and tissue: data analysis using resonant Mie scattering (RMieS) EMSC algorithm” . The Analyst. 137(6): 1370-1377.

Behar, F., Vandenbroucke, M., Tang, Y., Marquis, F., and Espitalie, J., 1997. “Thermal cracking of kerogen in open and closed systems: determination of kinetic parameters and stoichiometric coefficients for oil and gas generation”. Org. Geochem. 26: 321-339. doi: 10.1016/S0146-6380(97)00014-4.

Belton, D.J., Patwardhan, S.V., Annenkov, V.V., Danilovtseva, and E.N., Perry. C.C., 2008. “From Biosilicification to Tailored Materials: Optimizing Hydrophobic Domains and Resistance to Protonation of Polyamines” Proc. Natl. Acad. Sci. USA. 105(16): 5963-5968.

Benning, L. G., Phoenix, V. R., Yee, N., and Tobin, M. J., 2004. “Molecular characterization of cyanobacterial silicification using synchrotron infrared micro-spectroscopy”. Geochimica et Cosmochimica Acta. 68(4): 729–741.

Berner, R.A., 1980. “Early Diagenesis: A Theoretical Approach”. ISBN: 9780691082608 256 pp.

Boskey, A.L., 2003. “Biomineralization: An Overview”. Connect Tissue Res. 44(1): 5-9.

Burnham, A.K. and Braun, R.L., 1990. “Development of a detailed model of petroleum formation, destruction, and expulsion from lacustrine and marine source rocks”. Org. Geochem. Proceedings of the 14th International Meeting on Organic Geochemistry. 16: 27-39. doi:10.1016/0146-6380(90)90023-S..

Burnham, A.K., Oh, M.S., Crawford, R.W., Samoun, A.M., 1989. “Pyrolysis of Argonne premium coals: activation energy distributions and related chemistry”. Energy Fuels. 3: 42-55. 10.1021/ef00013a008.

Ceresoli, D., Bernasconi, M., Iarlori, S., Parrinello, M., and Tosatti, E., 2000. “Two-Membered Silicon Rings on the Dehydroxylated Surface of Silica”. Physical Review Letters. 84:3887-3890.

Coates, J., 2000. “Interpretation of Infrared Spectra, A Practical Approach”. Encyclopedia of Analytical Chemistry. R.A. Meyers (Ed.) John Wiley & Sons Ltd.

Dieckmann , V., Horsfield, B., Schenk, H.J., 2000. “heating rate dependency of petroleum-forming reactions: implications for compositional kinetic predictions. Org. Geochem. 31: 1333-1348. doi: 10.1016/S0146-6380(00)00105-4.

Ernst, W.G., and Calvert, S.E., 1969. “An Experimental Study on the Recrystalization of Porcelanite and its Bearing on the Origin of some Bedded Cherts”. The American Journal of Science. 267-A: 114-133.

Falkowski, P.G., Barber, R.T., and Smetacek, V., 1998. “Biogeochemical Controls and Feedbacks on Ocean Primary Production”. Science. 281(5374): 200-206.

García-Lodeiro, I., Macphee, D.E., Palomo, A., and Fernández-Jiménez, A., 2009. “Effect of alkalis on fresh C–S–H gels”. FTIR analysis, Cement and Concrete Research. **39**: 147–153.

Gelabert, A., Pokrovsky, O.S., Schott, J., Boudou, A., Feurtet-Mazel, A., Mielczarski, J., Mielczarski, E., Mesmer-Dudons, N., and Spalla, O., 2004. "Study of diatoms/aqueous solution interface. I. Acid-base equilibria and spectroscopic observation of freshwater and marine species". Geochimica et Cosmochimica Acta. 68(20): 4039–4058.

Gilbert, P.U.P.A., Abrecht, M., and Frazer, B.H., 2005. "The Organic-Mineral Interface in Biominerals", Reviews in Mineralogy & Geochemistry. 59(1): 157-185.

Grabbe, A., Michalske, T.A., and Smith, W.L., 1995. "Strained Siloxane Rings on the Surface on Silica: Their Reaction with Organosiloxanes, Organosilanes, and Water". J. Phys. Chem. 99 (13): 4648–4654.

Griffin, G.M., 1971, Interpretation of X-ray diffraction data, in Carver, R.E., ed., procedures in Sedimentary Petrology: New York, Wiley, p. 541–569.

Grim, R. E., 1947, Relation of clay mineralogy to origin and recovery of petroleum: Am.Assoc. Petroleum Geologists Bull., v. 31, no. 8, p. 1491-1499.

Hantschel, T., and Kauerauf, A.I., 2009. "Fundamentals of Basin and Petroleum Systems Modeling". Springer-Verlag. Pp. 476. doi: 10.1007/978-3-540-72318-9.

Hasle, G. R., and Syvertsen, E. E., 1996. "Marine Diatoms". In: C.R. Tomas, editor. Identifying Marine Diatoms and Dinoflagellates. San Diego, US: Academic Press, P.5–385.

Hecky, R.E., Mopper, K., Kilham, P., and Degens, E.T., 1973. "The Amino Acid and Sugar Composition of Diatom Cell-Walls". Mar Biol. 19(4): 323-331.

Hildebrand, M., 2008. "Diatoms, Biomineralization Processes, and Genomics". Chemical Review. 108(11): 4855–4874.

Ito, Y., and Nakashima, S., 2002. "Water Distribution in Low Grade Siliceous Metamorphic Rocks by Micro-FTIR and its Relation to Grain Size: A Case from the Kanto Mountain Region, Japan". Chem Geol. 189(1):1-18.

Igisu, M., Komiya, T., Kawashima, M., Nakashima, S., Ueno, Y., Han, J., Shu, D., Li, Y., Guo, J., Maruyama, S., and Takai, K., 2014. "FTIR Microspectroscopy of Ediacaran Phosphatized Microfossils from the Doushantuo Formation,Weng'an, South China". Gondwana Research. 25(3):1120-1138

Igisu, M., Yokoyama, T., Ueno, Y., Nakashima, S., Shimojima, M., Ohta, H., and Maruyama, S., 2015. "Influences of silica and embedding on the thermal alteration of aliphatic hydrocarbons in cyanobacteria during diagenesis, as evaluated by FTIR microspectroscopy" submitted to Palaios.

Johns, W. D., 1979. "Clay Mineral Catalysis and Petroleum Generation". Annual Review of Earth and Planetary Sciences. 7:183.

Jungandreas A., Wagner, H., Wilhelm, C., 2012. "Simultaneous measurement of the silicon content and physiological parameters by FTIR spectroscopy in diatoms with siliceous cell walls". Published by Oxford University Press on behalf of Japanese Society of Plant Physiologists.

Knoll, A. H., 2003. "Biomineralization and Evolutionary History". In: Dove, P.M., DeYoreo, J. and Weiner, S.,editors. Biomineralization. Reviews in Mineralogy and Geochemistry. 54(1):329-56.

Kobayashi, A., Tanaka, J., and Nagumo, T., 1998. "Morphological and taxonomical study of *Arachnoidiscus ornatus* Ehreb. (Bacillariophyceae) in Japan". Diatom. 14: 25-33. (In Japanese with English abstract)

Kebukawa, Y., Nakashima, S., Otsuka, T., Nakamura-Messenger, K., Zolensky, M.E., 2009. "Rapid contamination during storage of carbonaceous chondrites prepared for micro FTIR measurements". Meteorit. Planet. Sci. 44: 545-557.

Kebukawa, Y., Nakashima, S., Zolensky, M.E., 2010. "Kinetics of organic matter degradation in the Murchison meteorite for the evaluation of parent-body temperature

history". Meteoritics & Planetary Science 45, Nr 1, 99–113.doi:10.1111/j.1945-5100.2009.01008.x.

Kröger, N., 2007. "Prescribing Diatom Morphology: toward Genetic Engineering of Biological Nanomaterials". Curr. Opin. Chem. Biol. 11(6): 662-669.

Kröger, N., and Poulsen, N., 2008. "Diatoms-From Cell Wall Biogenesis to Nanotechnology". Annu Rev Genet. 42(1): 83-107.

Kröger, N., and Sandhage, K.H., 2010. "From Diatom Biomolecules to Bioinspired Syntheses ofSilica- and Titania-based Materials". MRS Bull. 35(2):122-126.

Kröger, N., and Sumper M., 2000. "The Biochemistry of Silica Formation in Diatoms". In: E. Bäuerlein. editor. Biomineralization. Weinheim, Germany: Wiley-VCH, Pp: 151–170.

Kröger, N., and Sumper, M., 2004. "The Molecular Basis of Diatom Biosilica Formation". In: E. Bäuerlein. editor. Biomineralization: From Biology to Biotechnology and Medical Application. Weinheim, Germany: Wiley-VCH Verlag GmbH & Co. KGaA, Pp.137-157. 2nd ed.

Levitan, O., Dinamarca, J., Hochman, G., and Falkowski, P.G., 2014. "Diatoms: A Fossil Fuel of the Future". Trends Biotechnol. 32(3):117-124.

Lin, Q., Xu, Z., Lan, X., Ni, Y., and Lu, C., 2011. "The reactivity of nano silica with calcium hydroxide". J Biomed Mater Res Part B. 99(B): 239–246.

Liu, W. and Shen Y.R., 2008. "Surface Vibrational Modes of α-Quartz(0001) Probed by Sum-Frequency Spectroscopy". PRL 101, 016101. doi: 10.1103/PhysRevLett.101.016101

Losic, D., Mitchell, J.G., and Voelcker, N.H., 2005. "Complex Gold Nanostructures Derived by Templating from Diatom Frustule", *Chemical Communications* (Cambridge, England). 39: 4905-4907.

Losic, D., Rosengarten, G., Mitchell, J.G., and Voelcker, N.H., 2006. “Pore Architecture of Diatom Frustules: Potential Nanostructured Membranes for Molecular and Particle Separations”. J Nanosci. Nanotechnol. 6(4): 1-8.

Losic, D., Short, K., Mitchell, J.G., Lal, R., and Voelcker, N.H., 2007. “AFM Nanoindentations of Diatom Biosilica Surfaces”. Langmuir: the ACS journal of surfaces and colloids. 23(9): 5014-5021.

Lowenstam, H.A., and Weiner, S., 1989. “On Biomineralization”. New York, Oxford (Oxfordshire): Oxford University Press.

Mann, S., 2001. “Biomineralization: Principles and concepts in Bioinorganic Materials Chemistry”. New York: Oxford University Press.

Mann. S., and Ozin, G.A., 1996. “Synthesis of Inorganic Materials with Complex form”. Nature. 382(6589): 313-318.

Mayama, S., and Kuriyama. A., 2002. “Diversity of Mineral Cell Coverings and their Formation Processes: a Review Focused on the Siliceous Cell Coverings”. J. Plant Res. 115(4): 289-295.

Mizutani, S., 1977. “Progressive Ordering of Cristobalitic Silica in the Early Stage of Diagenesis”. Contributions to Mineralogy and Petrology. 61: 129-140.

Mount, A.S., Wheeler, A.P., Paradkar, R.P., and Snider, D., 2004. “Hemocyte-mediated Shell Mineralization in the Eastern Oyster”. Science. 304(5668): 297-300.

Nagumo, T., and Suzuki, H., 2001. “Diatoms-micro arts designed by nature-”. The Hitachi Scientific Instrument News. 44(1): 7-11.

Nakajima, T., and Volcani, B.E., 1969. “3,4-Dihydroxyproline: a new Amino Acid in Diatom Cell Walls”. Science. 164(3886):1400-1401.

Nakashima, S., Ito, Y., and Shiota, D., 2002. “Silica-Water-Organics Interactions”. Japanese Magazine of Mineralogical and Petrological Sciences. 31: 58-61.

Nakashima, S., Matayoshi, H., Yuko, T., Michibayasgi, K., Masuda, T., Kuroki, N., Yamagishi, H., Ito, Y., and Nakamura, A., 1995. “Infrared Microspectroscopy Analysis of Water Distribution in Deformed and Metamorphosed Rocks”, Tectonophysics, 245(3): 263-276.

Okumura, S. and Nakashima S., 2004. “Water diffusivity in rhyolitic glasses as determined by in-situ IR Spectroscopy”. *Physics and Chemistry of Minerals.* **31:** 183-189.

Okumura, S. and Nakashima, S., 2005. “Molar absorptivities of OH and H2O in rhyolitic glass at room temperature and at 400 – 600 °C”. *American Mineralogist.* **90:** 441-447.

Okumura, S. and Nakashima, S., 2006. “Water diffusion in basaltic to dacitic glasses”. Chemical Geology. 227: 70–82.

Painter P.C., Snyder, R.W., Starsinic, M., Coleman, M.M., Kuehn, D.W., Davis, A., 1981. “Concerning the Application of FT-IR to the Study of Coal: A Critical Assessment of Band Assignments and the Application of Spectral Analysis Programs. Appl. Spectrosc. 35: 475-485.

Parkinson, J., and Gordon, R., 1999. “Beyond Micromachining: the Potential of Diatoms”. Trends Biotechnol. 17(5): 190-196.

Patwardhan, S.V., Maheshwari, R., Mukherjee, N., Kiick, K. L., and Clarson, S.J. 2006. “Conformation and Assembly of Polypeptide Scaffolds in Templating the Synthesis of Silica: An Example of a Polylysine Macromolecular “Switch””. Biomacromolecules. 7: 491-49.

Pickett-Heaps, J.D., Schmid, A.M., and Edgar, L.A., 1990. “The Cell Biology of Diatom Valve Formation.” In: F.E. Round, D.J. Chapman, editors. Progress in Phycological Research. Bristol, UK: Biopress, 7: Pp. 1-168.

Pollastro, R., 1993. “Considerations and applications of the illite/smectite geothermometer in hydrocarbon-bearing rocks of Miocene to Mississippian age”. Clays And Clay Minerals, 41(2): 119-133.

Round, F. E., Crawford, R. M., and Mann, D. G., 1990. “The Diatoms, Biology & Morphology of the Genera”. Cambridge, UK: Cambridge University Press.

Saikia, B.J., Parthasarathy, G., and Sarmah, N. C., 2008. “Fourier transform infrared spectroscopic estimation of crystallinity in SiO2 based rocks”. Bull. Mater. Sci. 31(5): 775-779.

Scheffel, A., Poulsena, N., Shian, S., and Kröger, N., 2011. “Nanopatterned Protein Microrings from a Diatom that Direct Silica Morphogenesis”. PNAS. 108(8): 3175-3180.

Schäffer, T.E., Ionescu-Zanetti, C., Proksch, R., Fritz, M., Walters, D.A., Almqvist, N., Zaremba, C.M., Belcher, A.M., Smith, B.L., Stucky, G.D., Morse, D.E., and Hansma, P.K., 1997. “Does Abalone Nacre form by Heteroepitaxial Nucleation or by Growth through Mineral Bridges?”. Chemistry of Materials. 9(8):1731-1740.

Schmidt, M., Botz, R., Rickert, D., Bohrmann, G., Hall, S.R., and Mann, S., 2001. “Oxygen Isotopes of Marine Diatoms and relations to Opal-A Maturation”. Geochimica et Cosmochimica Acta. 65(2): 201-211.

Shiota, D., and Nakashima, S., 2005. “Threonine Transformation under Hydrothermal Conditions”. Chemistry Letters. 34(2): 158-159.

Smetacek, V.S., 1985. “Role of Sinking in Diatom Life-History Cycles: Ecological, Evolutionary and Geological Significance”. Mar Biol. 84(3): 239–251.

Stainforth, J.G., 2009. “Practical kinetic modelling of petroleum generation and expulsion”. Mar. Pet. Geol. 26: 552-572. doi: 10.1016/j.marpetgeo.2009.01.006.

Sumper, M., 2002. “A Phase Separation Model for the Nanopatterning of Diatom

Biosilica". Science. 295(5564): 2430-2433.

Sumper, M., and Brunner, E., 2008. "Silica Biomineralisation in Diatoms: The Model Organism Thalassiosira pseudonana". ChemBioChem. 9(8): 1187-1194.

Sumper, M., and Kröger, N., 2004. "Silica Formation in Diatoms: the Function of Long-Chain Polyamines and Silaffins". J. Mater. Chem. 14(14):2059-2065.

Tang, Z., Kotov, N.A., Magonov, S., and Ozturk, B., 2003. "Nanostructured Artificial Nacre". Nature materials. 2(6):413-418.

Tesson, B., and Hildebrand, M., 2013. "Characterization and Localization of Insoluble Organic Matrices Associated with Diatom Cell Walls: Insight into their Roles during Cell Wall Formation". PLoS ONE. 8(4): e61675.

Theriot, E. C., 2012. "Diatoms". In: eLS. Chichester, UK. John Wiley & Sons. Ltd. http://www.els.net. doi: 10.1002/9780470015902.a0000330.pub2

Tissot, B.P., and Welt, D.H., 1984. "Petroleum Formation and Occurrence". Springer-Verlag. 699p.

Tomiak, P.J., Penkman, K.E.H., Hendy, E.J., Demarchi, B., Murrells, S., Davis S.A., McCullagh, P., Collins, M.J., 2013. "Testing the limitations of artificial protein degradation kinetics using known-age massive Porites coral skeletons". Quaternary Geochronology. 16: 87-109.

Tonoue, R., Katsura, M., Hamamoto, M., Bessho, H., and Nakashima, S., 2014. "A Method to Obtain the Absorption Coefficient Spectrum of Single Grain Coal in the Aliphatic C–H Stretching Region Using Infrared Transflection Microspectroscopy". Applied Spectroscopy. 68: 733-739.

Tonoue, R., 2015. “Infrared micro-spectroscopy of coals and developments of quantitative analysis methods”. PhD thesis. Department of Earth and Space Science, Graduate School of Science, Osaka University.

Tréguer, P., Nelson, D.M., Van Bennekom, A.J., DeMaster, D.J., Leynaert, A., and Quéguiner, B., 1995. “The Silica Balance in the World Ocean: A Reestimate”. Science. 268(5209): 375–379.

Vrieling, E.G., Beelen, T.P.M., van Santen, R.A., and Gieskes, W.W.C., 2000. “Nanoscale Uniformity of Pore Architecture in diatomaceous Silica: A Combined Small and Wide Angle Xray Scattering study”. J. Phycol. 36(1), 146-159.

Wei, Z., Moldowan, J.M, Dahl, J., Goldstein, T.P., and Jarvie, D.M., 2006. “The catalytic effects of minerals on the formation of diamondoids from kerogen macromolecules”. Organic Geochemistry. 37(11): 1421-1436. doi:10.1016/j.orggeochem.2006.07.006.

Wilkerson, F.P., and Dugdale, R.C., 1998. “Silicate Regulation of New Production in the Equatorial Pacific Upwelling”. Nature. 391(6664): 270–273.

Yamagishi, H., Nakashima, S., and Ito, Y., 1997. “High temperature infrared spectra of hydrous microcrystalline quartz”. Phys Chem Minerals. 24: 66–74

Yool, A., and Tyrrell, T., 2003. “Role of Diatoms in Regulating the Ocean's Silicon Cycle”. Global Biogeochem Cycles. 17(4): 1103–1124.

List of publications

Leila Alipour, Satoru Nakashima, Rika Harui, Thomas Dieing, Keiichi Nakamoto, Miriam Böhmler, Masanari Furiki and Osamu Oku, "Microscopic imaging of a natural bionanomaterial - silica frustules of centric diatoms -" Proceedings of the 5th International Conference on Nanostructures (ICNS5) 6-9 March 2014, Kish Island, Iran. 107-109.

Leila Alipour , Mai Hamamoto , Satoru Nakashima, Rika Harui, Masanari Furiki and Osamu Oku. "Infrared (IR) Micro-Spectroscopy of Bionanomaterials (Diatoms) with Careful Evaluation of Void Effects".accepted on July 13, 2015 for publication in *Applied Spectroscopy*.

List of presentations

Leila Alipour , Satoru Nakashima, Osamu Oku , Akio Murakami and Rika Harui. "Characterization of diatom silica frustules by IR micro-spectroscopy (1): polymerization degree of Si-O". The Annual Meeting of the Spectroscopical Society of Japan, Tokyo, Japan, (November 27-29, 2012), P11. Poster presentation.

Leila Alipour, Mai Hamamoto , Satoru Nakashima. "Infrared micro-spectroscopy of centric diatom silica frustules". 69th Annual Meeting of the Japanese Society of Microscopy, "Microscopy: Cutting-edge technology opening up new fields", Osaka, Japan, (May 20-21, 2013),P46. Poster presentation.

Leila Alipour, Satoru Nakashima, Rika Harui, Thomas Dieing, Keiichi Nakamoto, Masanari Furiki and Osamu Oku. "IR and Raman Imaging of Centric Diatom Silica frustules". The Annual Meeting of the Spectroscopical Society of Japan, Osaka, Japan, (November 19-21, 2013), P16. Poster presentation.

Leila Alipour, Mai Hamamoto, Satoru Nakashima. "Infrared Micro-spectroscopy of Silica Frustule of Centric Diatom *Arachnoidiscus ornatus*".7th International Conference on

Advanced Vibrational Spectroscopy, Kobe, Japan, (August 25-30, 2013), P052.
Poster presentation.

Leila Alipour, Satoru Nakashima, Rika Harui, Thomas Dieing, Keiichi Nakamoto, Miriam Böhmler[5], Masanari Furiki and Osamu Oku. "Microscopic imaging of a natural bionanomaterial - silica frustules of centric diatoms -". 5th International Conference on Nanostructures, Kish Island, Iran, (March 6-9, 2014), PBio036. Poster presentation.